Email : bilgumus@gmail.com
Visit our home page on www.dergipark.org.tr/mejs

Tamraz H. TAMRAZOV
Field: Biological Sciences
(Assoc.Prof.Dr., Department of Plant Physiology and Biotechnology, Research Institute of Crop Husbandry, Ministry of Agriculture of the Republic of Azerbaijan)
tamraz.tamrazov@mail.ru

Yusuf ZEREN

Field: Mathematics, Topology

(Assoc.Prof.Dr., Yıldız Technical University, Faculty of Science and Letters, Dep. of Mathematics, TURKEY)

yzeren@yildiz.edu.tr

Z. Gökay KAYNAK

Field: Nuclear Physics

(Retired Prof.Dr., Uludag University, Faculty of Science, Dep. of Physics, Turkey) kaynak@uludag.edu.tr

Middle East Journal of Science

https://dergipark.org.tr/mejs

e-ISSN:2618-6136

MEJS
Volume 11
Issue 1
June 2025

CONTENTS

Middle East Journal of Science

https://dergipark.org.tr/mejs **MEJS**

e-ISSN:2618-6136

Research Article

THE USE OF PARTIALLY LINEAR REGRESSION MODEL IN IMAGE PROCESSING

Merve Bingöl Sukutli [1] ***Seçil Yalaz****[2]

[1] Dicle University, Science Faculty, Statistics Department, Türkiye
[2] Dicle University, Science Faculty, Statistics Department, Türkiye
* Corresponding author; syalaz@dicle.edu.tr

Abstract: *Digital imaging systems are increasingly popular in various fields such as education, industry, engineering, and healthcare. The ease of use and low cost of these systems contribute to their widespread adoption. However, the main disadvantage of digital imaging is resolution issues. In practical applications that require high resolution, dense sensors are used to obtain robust images. This method, however, increases costs and produces more data and noise due to its density. Additionally, millions of low-resolution but valuable pieces of information are lost. Image processing techniques are used to enhance resolution and preserve high-frequency information. The primary aim of this study is to comprehensively investigate the importance and effectiveness of using partially linear models in image processing applications. Partially linear regression aims to offer a new model for image enhancement without losing high-frequency information. Because many problems encountered in the field of image processing stem from resolution issue, this study aims to understand the effects of resolution on image processing processes and to demonstrate how partially linear models can be used to address these effects. Various comparison methods have been used to evaluate the effectiveness of the proposed method. These methods have been employed to objectively assess the quality difference between images, highlighting the superiority of the proposed method over traditional methods. The study's findings show that partially linear models are a significant tool in image processing applications. Future studies may aim to examine in more detail how these models perform with different types of images and conditions.*

Keywords*: Digital Imaging Systems, Image Enhancement, Image Processing, Partially Linear Regression, Resolution*

Received: August 1, 2024 *Accepted: February 15, 2025*

1. Introduction

At the core of image processing lies the conversion of images captured by an optical sensor (camera) into another form in a computer environment [1]. The analysis and classification of these transformed forms rely on regression analysis methods.

Regression analysis is a statistical method that allows for the examination of the relationship between a dependent variable and one or more independent variables [2]. This method is used particularly to understand the relationship between variables and to examine the effects of independent variables on the dependent variable. Additionally, regression analysis expresses the effects of variables on each other as a mathematical function [1].

Depending on the characteristics of the dataset, the purpose of the analysis, and the assumptions, various regression approaches exist. At the center of these approaches is the parametric regression model, which works under the assumption that the form of the relationship between independent and

dependent variables is known. In a parametric model, if a linear relationship is observed between the dependent variable and a single independent variable, the model is called a simple regression model.

In image processing, the linear regression method used to understand and predict the relationship between 2D data pairs expresses each pixel in the image as an independent variable, and the features or measurements corresponding to the pixel values as the dependent variable.

In addition to linear regression, multiple linear regression analysis methods are used for models that include more independent variables. While this method is used in fields like statistics and machine learning to relate a dependent variable to multiple independent variables and to model this relationship, in image processing it is used to evaluate and model the collective effect of multiple independent variables on the dependent variable (image). Multiple linear regression analysis methods are utilized to segment images (define the boundaries of objects in the image and divide the image into sections), achieve image restoration (remove noise and repair noised areas in the image), and obtain high-resolution images from low-resolution images.

It is not correct to say that only parametric (linear) models are preferred for regression. In situations where the form of the relationship between variables is unknown, non-parametric and semi-parametric (partially linear) methods are preferred, which are used in various fields such as economics, finance, marketing, medicine, health sciences, machine learning, data mining, and image processing.

Recently, the increasing popularity of image processing has made it an intriguing topic for analysts, engineers, and statisticians. Ease of use and low cost have made method selection in image processing preferable. However, with the reduction in cost, issues such as resolution, decrease in image quality, and noticeable overlapping effects have emerged. These problems stem from the limited number of highly correlated sensors used in digital imaging devices. Increasing the number of pixels used not only raises the cost but also causes blur in the image, increasing noise [3].

The aim of this study is to comprehensively examine the importance and effectiveness of using partially linear models in image processing applications. The study aims to explore the effects of image processing on workflows and how partially linear models can mitigate these effects.

2. Materials and Methods

This study examines the impact of using regression analysis within partially linear models in image processing techniques. Literature reviews on the concept of partially linear regression have revealed general approaches for parameter estimation. It has been observed that problems related to image processing are solved using kernel and Gaussian blurring methods in the relevant regression.

The study explains the correction methods for noised images. By comparing the histogram values of the noised and corrected images, a homogeneous distribution has been obtained for the corrected image. Subsequently, it has become possible to estimate the noise level by modeling the relationship between the images.

After all processes were completed, the noised and corrected images were displayed on the screen. The study includes the steps used to process images from the specified file path and visualize the results, designed to meet the specified requirements.

2.1. Regression Models and Image Processing

Regression analysis is a statistical method used to make inferences about the regression function and is primarily used to examine the relationship between two variables. Parametric and non-parametric regression techniques approach regression analysis from two different perspectives. Parametric regression has strong assumptions, whereas non-parametric regression does not require these assumptions.

In parametric regression analysis, the parameters (β) of a pre-specified model are estimated, while in non-parametric regression analysis, the goal is to directly estimate the regression function (g) [3].

In image processing, digital filters are used to smooth images or enhance edges. Some of the filters used include the mean filter, median filter, Gaussian smoothing filter, Kalman filter for object recognition in images, frequency filters, and kernel regression.

The mean filter replaces each pixel value in an image with the average value of its neighbors, including itself. This process removes pixel values that are not meaningful for the image. The mean filter is a convolution filter based on a kernel template.

The median filter, like the mean filter, considers neighboring pixels to calculate the value of each pixel. However, instead of replacing the pixel value with the average of the neighboring pixel values (mean filter), it sorts the neighboring pixels and takes the median value. If the region being examined (within the template) has an even number of pixels, the average of the two middle pixels is used as the median value.

The Gaussian smoothing operator is a two-dimensional (2D) convolution operator used to blur images by removing details and noise. It is similar to the mean filter but uses a different kernel template. This template is represented by a bell-shaped curve known as the Gaussian function. The formula for the Gaussian function that gives the bell-shaped curve can be written in both the 2D plane and the 3D space.

$$G(x) = \frac{1}{\sqrt{2\pi}\,\sigma} e^{-\frac{x^2}{2\sigma}}$$

$$G(x) = \frac{1}{\sqrt{2\pi}\,\sigma^2} e^{-\frac{x^2+y^2}{2\sigma^2}}$$

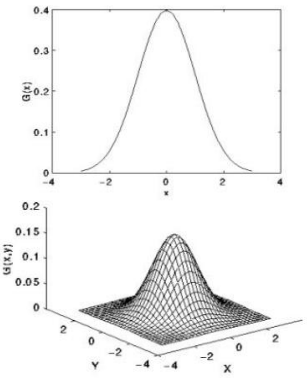

x	σ	$\frac{1}{\sqrt{2\pi}\,\sigma}$	$e^{-\frac{x^2}{2\sigma}}$	$z = \frac{1}{\sqrt{2\pi}\,\sigma} e^{-\frac{x^2}{2\sigma}}$
-2	1	0,398943084	0,135335283	0,053991075
-1,9	1	0,398943084	0,164474457	0,065615947
-1,8	1	0,398943084	0,197898699	0,078950317
-1,7	1	0,398943084	0,235746077	0,094049267
-1,6	1	0,398943084	0,2780373	0,110921058
-1,5	1	0,398943084	0,324652467	0,129517856
-1,4	1	0,398943084	0,375311099	0,149727767
-1,3	1	0,398943084	0,429557358	0,171368937
-1,2	1	0,398943084	0,486752256	0,194186446
-1,1	1	0,398943084	0,546074427	0,217852616
-1	1	0,398943084	0,60653066	0,241971212
-0,9	1	0,398943084	0,666976811	0,266085786
-0,8	1	0,398943084	0,726149037	0,289692136
-0,7	1	0,398943084	0,782704538	0,312254562
-0,6	1	0,398943084	0,835270211	0,333225274
-0,5	1	0,398943084	0,882496903	0,352066036
-0,4	1	0,398943084	0,923116346	0,368270882
-0,3	1	0,398943084	0,955997482	0,381388584
-0,2	1	0,398943084	0,980198673	0,391043481
-0,1	1	0,398943084	0,995012479	0,396953347
0	1	0,398943084	1	0,398943084
0,1	1	0,398943084	0,995012479	0,396953347
0,2	1	0,398943084	0,980198673	0,391043481
0,3	1	0,398943084	0,955997482	0,381388584

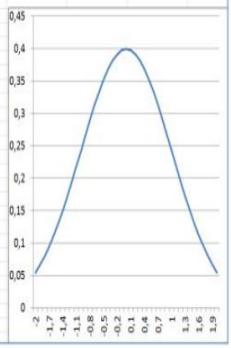

Figure 1. Gaussian filter for 2D plane and 3D spaces

In Figure 1, (σ) represents the standard deviation of the distribution. It is also assumed that the mean of the distribution is zero (i.e., centered on the line).

The purpose of the Kalman filter is to predict the multi-person pose tracking system developed and evaluate it in terms of processing time using various pose estimation algorithms. Pose estimation arises from determining the pixel positions of key points of the human skeleton viewed by the camera. The outputs of pose estimation methods associate the pixel values of all detected joint points in the image with the relevant person. Identifying individuals across successive frames in videos is particularly important for understanding their movements. This allows for determining what kind of movements individuals make and at what moments in the video [4].

Kernel regression is an image-processing method. In this method, scaling, rotation, and stretching parameters are calculated from the original data analyzed for local structures to provide directive matrices. These calculations are performed using singular value decomposition (SVD) with locally estimated gradients on local gradients. The algorithm is fed with raw pixels associated with each image. This method requires minimal preprocessing of images before classification, making it more useful than traditional training algorithms [1].

2.1.1 Partially Linear Regression

Partially linear models are a special model that includes both parametric and nonparametric methods. These models are used when part of the data can be explained with a parametric formula, but another part needs to be modeled more flexibly [1]. The formulation of the model is as follows:

$$Y = \boldsymbol{X}\beta + g(x^*) + \varepsilon, \tag{1}$$

where $\boldsymbol{X}\beta$ represents the parametric component, $\boldsymbol{X}$ is the $(n \times p)$ dimensional independent variable matrix, β is the $(p \times 1)$ dimensional coefficient vector, x^* is the nonparametric variable vector, $g(.)$ is the nonparametric function, and ε is the error term.

Because the partially linear regression model combines both parametric and nonparametric regression functions, it is also called semiparametric regression [5]. This model offers a more flexible and adaptable analysis method by using both parametric and nonparametric components together. If the effects of the parametric variables are ignored or if these variables are not included in the analysis, the semiparametric regression model becomes a purely nonparametric regression model. This feature makes the semiparametric regression model a powerful tool for examining both linear and nonlinear relationships simultaneously.

In the partially linear model, a kernel corrector $K_h(x^*)$ applied with bandwidth h is used. This corrector, used to calculate the effect from other points at point x^*, is shown as:

$$w(x^*) = \frac{K_h(x_i^* - x^*)}{\sum_{i=1}^{n} K_h(x_i^* - x^*)} \tag{2}$$

where $K_h(x^*) = \frac{1}{h_n} K\left(\frac{x^*}{h_n}\right)$, K is the kernel function and h_n is the bandwidth parameter. Using the kernel corrector, the effect at point x^* on variables x and y is estimated using the some regulations in Nadaraya-Watson estimator (NWE) separately:

$$\hat{g}_{x,h}(x_i^*) = \sum_{i=1}^{n} w(x^*)x_i$$

$$\hat{g}_{y,h}(x_i^*) = \sum_{i=1}^{n} w(x^*)y_i$$

Using these estimates, new variables cleared of the effect are obtained by removing the effect at point x^* from the variables x and y as:

$$\tilde{Y}_i = Y_i - \hat{g}_{y,h}(x_i^*),$$

$$\tilde{X}_i = X_i - \hat{g}_{x,h}(x_i^*).$$

The parametric component is estimated by:

$$\hat{\beta} = (\tilde{X}^T\tilde{X})^{-1}\tilde{X}^T\tilde{Y}, \tag{3}$$

for the estimated variance $\hat{\sigma}^2 = (\tilde{Y}^T\tilde{Y} - \hat{\beta}^T\tilde{X}^T\tilde{Y})/(n-2)$. And the nonparametric function is estimated as:

$$\hat{g}(x^*, \hat{\beta}) = \sum_{i=1}^{n} w(x^*)(y_i - x_i\hat{\beta}), \tag{4}$$

which calculates the nonparametric effect of the y variable at point x^*. This process ensures the accurate analysis of relationships between variables in image processing applications and controls the effect of nonparametric components.

3. Findings and Discussion

3.1. Use of Partially Linear Model in Image Processing

The main aim of using regression predictors in image processing is to reduce noise while preserving the edge structure when correcting the image.

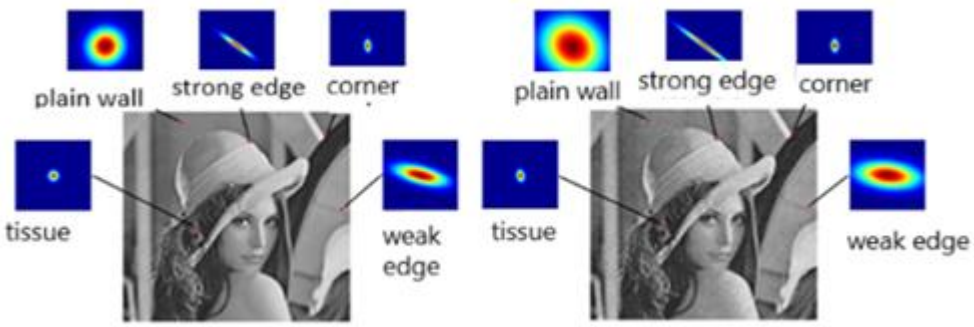

(a) (b)

Figure 2. (a) Noiseless and (b) Gaussian noisy image with SNR = 5.64dB

Figure 2 shows how local structures change in predictions for noiseless and noisy images [1]. In digital image processing, some filters are needed to smooth the image, highlight objects, or recognize them. In parametric models, different pixels are more easily identified, while it is quite difficult to distinguish this in similar scenes. Smoothing at the x^* point in any data set is obtained by fitting a weighted OLS line. In image processing, after determining the color weights of the image divided into pixels, a smoothed image is obtained by fitting the least squares line at any pixel.

When performing partially linear regression analysis in image processing, a second dimension (2-D) is added to classical prediction methods (see Equation (1)) [6]:

$$y_i = \boldsymbol{x}_i\beta + g(\boldsymbol{x}_i^*) + \varepsilon_i, \quad i = 1, \dots, n. \tag{5}$$

Here, the coordinates of measured data y_i is now the (2×1) vector $\boldsymbol{x}_i^*$, $g(.)$ is the (hitherto unspecified) regression function and ε_is are the i.i.d. zero mean noise values (with otherwise no particular statistical distribution assumed), $\boldsymbol{x}^*$ has dimensions $(n \times q)$. When expanding the nonparametric function $g(\boldsymbol{x}_i^*)$ becomes

$$g(\boldsymbol{x}_i^*) = g(\boldsymbol{x}^*) + \{\boldsymbol{\nabla} g(\boldsymbol{x}^*)\}^T(\boldsymbol{x}_i^* - \boldsymbol{x}^*) + \frac{1}{2}(\boldsymbol{x}_i^* - \boldsymbol{x}^*)^T\{\boldsymbol{\mathcal{H}} g(\boldsymbol{x}^*)\}(\boldsymbol{x}_i^* - \boldsymbol{x}^*) + \dots$$

$$= g(\boldsymbol{x}^*) + \{\boldsymbol{\nabla} g(\boldsymbol{x}^*)\}^T(\boldsymbol{x}_i^* - \boldsymbol{x}^*) + \frac{1}{2} vec^T\{\boldsymbol{\mathcal{H}} g(\boldsymbol{x}^*)\} vec\{(\boldsymbol{x}_i^* - \boldsymbol{x}^*)(\boldsymbol{x}_i^* - \boldsymbol{x}^*)^T\} + \cdots, \tag{6}$$

where $vec\left(\begin{bmatrix} a & b \\ b & d \end{bmatrix}\right) = [a \quad b \quad b \quad d]^T$ is a vectorization operator, $g(\boldsymbol{x}_i^*)$ represents the function's value at $\boldsymbol{x}_i^*$, $\boldsymbol{\nabla} g(\boldsymbol{x}^*)$ is the (2×1) gradient (derivative vector) at $\boldsymbol{x}^*$, and $\boldsymbol{\mathcal{H}} g(\boldsymbol{x}^*)$ is the (2×2) second derivative matrix (Hessian) at $\boldsymbol{x}^*$. The operation of vectorizing the elements of the lower triangle of a symmetric matrix is represented as $vech\left(\begin{bmatrix} a & b \\ b & d \end{bmatrix}\right) = [a \quad b \quad d]^T$ and $vech\left(\begin{bmatrix} a & b & c \\ b & e & f \\ c & f & i \end{bmatrix}\right) = [a \quad b \quad c \quad e \quad f \quad i]^T$.

$$g(\boldsymbol{x}_i^*) = \theta_0 + \boldsymbol{\theta}_1^T(\boldsymbol{x}_i^* - \boldsymbol{x}^*) + \boldsymbol{\theta}_2^T\, vech\{(\boldsymbol{x}_i^* - \boldsymbol{x}^*)(\boldsymbol{x}_i^* - \boldsymbol{x}^*)^T\} + \cdots \tag{7}$$

Comparing (6) and (7), $\theta_0 = g(\boldsymbol{x}^*)$ becomes the pixel values of interest and vectors $\boldsymbol{\theta}_1$ and $\boldsymbol{\theta}_2$ becomes

$$\boldsymbol{\theta}_1 = \boldsymbol{\nabla} g(\boldsymbol{x}^*) = \left[\frac{\partial g(\boldsymbol{x}^*)}{\partial x_1^*}, \frac{\partial g(\boldsymbol{x}^*)}{\partial x_2^*}\right]^T, \tag{8}$$

$$\boldsymbol{\theta}_2 = \frac{1}{2}\left[\frac{\partial^2 g(\boldsymbol{x}^*)}{\partial {x_1^*}^2}, \; 2\frac{\partial^2 g(\boldsymbol{x}^*)}{\partial x_1^* \partial x_2^*}, \; \frac{\partial^2 g(\boldsymbol{x}^*)}{\partial {x_2^*}^2}\right]^T. \tag{9}$$

Regardless of parameter results, the main goal is to find pixel values. Therefore, the estimation of $\boldsymbol{\theta}_q$ is:

$$\underset{\{\boldsymbol{\theta}_q\}}{min}\sum_{i=1}^{n}[y_i-\boldsymbol{x}_i\beta-\theta_0-\boldsymbol{\theta}_1^T(\boldsymbol{x_i^*}-\boldsymbol{x^*})-\boldsymbol{\theta}_2^T vech\{(\boldsymbol{x_i^*}-\boldsymbol{x^*})(\boldsymbol{x_i^*}-\boldsymbol{x^*})^T\}\dots]^2 K_{\boldsymbol{H}}(\boldsymbol{x_i^*}-\boldsymbol{x^*}) \quad (10)$$

where $K_{\boldsymbol{H}}(t)=\frac{1}{\det(\boldsymbol{H})}K(\boldsymbol{H}^{-1}\boldsymbol{t})$ represents $\boldsymbol{H}$, the (2×2) smoothing matrix, and K, the 2-dimensional kernel function. Selection of $\boldsymbol{H}$ can be obtained using [1]. However, since the β parameters are also unknown here, they must first be estimated.

Let $\boldsymbol{\omega}$ be the weight matrix and $diag$ represent the diagonal matrix:

$$\boldsymbol{\omega}=diag\big[K_{\boldsymbol{H}}(\boldsymbol{x}_1^*-\boldsymbol{x}^*),\ K_{\boldsymbol{H}}(\boldsymbol{x}_2^*-\boldsymbol{x}^*),\dots,K_{\boldsymbol{H}}(\boldsymbol{x}_n^*-\boldsymbol{x}^*)\big]. \quad (11)$$

Let $\widehat{\boldsymbol{\omega}}_x=\boldsymbol{\omega X}$ and $\widehat{\boldsymbol{\omega}}_y=\boldsymbol{\omega}y$ be the new variables stripped of the effect. For the new variables, $\tilde{y}=y-\widehat{\boldsymbol{\omega}}_y$ and $\widetilde{\boldsymbol{X}}=\boldsymbol{X}-\widehat{\boldsymbol{\omega}}_x$, the parametric component β is estimated by:

$$\hat{\beta}=(\widetilde{\boldsymbol{X}}^T\widetilde{\boldsymbol{X}})^{-1}\widetilde{\boldsymbol{X}}^T\tilde{y}. \quad (12)$$

Thus, by adding weights to the least squares method to determine the $\boldsymbol{\theta}$ coefficients, the model is allowed to perform better in situations with varying variance. Consequently:

$$\widehat{\boldsymbol{\theta}}=\underset{\boldsymbol{\theta}}{argmin}\left\|\boldsymbol{y}-\boldsymbol{X}\hat{\beta}-\boldsymbol{X}_{\boldsymbol{x^*}}^*\boldsymbol{\theta}\right\|^2\boldsymbol{\omega}=\underset{\boldsymbol{\theta}}{argmin}\left(\boldsymbol{y}-\boldsymbol{X}\hat{\beta}-\boldsymbol{X}_{\boldsymbol{x^*}}^*\boldsymbol{\theta}\right)^T\boldsymbol{\omega}\left(\boldsymbol{y}-\boldsymbol{X}\hat{\beta}-\boldsymbol{X}_{\boldsymbol{x^*}}^*\boldsymbol{\theta}\right). \quad (13)$$

Here, $\boldsymbol{y}=[y_1,y_2,\dots y_n]^T$ represents the observation vector, $\boldsymbol{\theta}=\left[\theta_0,\boldsymbol{\theta}_1^T,\dots,\boldsymbol{\theta}_q^T\right]^T$ represents the coefficient vector, and $\boldsymbol{X}_{\boldsymbol{x^*}}^*$ represents the matrix containing the distance of each point in the data set to the point $\boldsymbol{x}^*$. Therefore:

$$\boldsymbol{X}_{\boldsymbol{x^*}}^*=\begin{bmatrix}1 & (\boldsymbol{x}_1^*-\boldsymbol{x}^*)^T & vech^T\{(\boldsymbol{x}_1^*-\boldsymbol{x}^*)(\boldsymbol{x}_1^*-\boldsymbol{x}^*)^T\} & \dots\\ 1 & (\boldsymbol{x}_2^*-\boldsymbol{x}^*)^T & vech^T\{(\boldsymbol{x}_2^*-\boldsymbol{x}^*)(\boldsymbol{x}_2^*-\boldsymbol{x}^*)^T\} & \dots\\ \vdots & \vdots & \vdots & \vdots\\ 1 & (\boldsymbol{x}_n^*-\boldsymbol{x}^*)^T & vech^T\{(\boldsymbol{x}_n^*-\boldsymbol{x}^*)(\boldsymbol{x}_n^*-\boldsymbol{x}^*)^T\} & \dots\end{bmatrix}. \quad (14)$$

To estimate the pixel values of the image, regardless of the estimator order q, we focus on the estimators of the θ_0 parameter:

$$\hat{g}(\boldsymbol{x}^*)=\hat{\theta}_0=\boldsymbol{e}_1^T\left(\boldsymbol{X}_{\boldsymbol{x^*}}^{*T}\boldsymbol{\omega}\boldsymbol{X}_{\boldsymbol{x^*}}^*\right)^{-1}\boldsymbol{X}_{\boldsymbol{x^*}}^{*T}\boldsymbol{\omega}\left(y-\boldsymbol{X}\hat{\beta}\right). \quad (15)$$

Here, $\boldsymbol{e}_1$ represents a column vector where the first element is 1 and the remaining elements are 0. For $q=0$, estimator θ_0, which is known as the NWE, is fundamentally different from using a higher-order estimator and then effectively discarding all estimated $\boldsymbol{\theta}_q$ values except for θ_0. Unlike the previous situation, the second method calculates the pixel value estimates assuming a local polynomial structure of degree q.

$\boldsymbol{X}_{\boldsymbol{x^*}}^{*T}\boldsymbol{\omega}\boldsymbol{X}_{\boldsymbol{x^*}}^*$ is a $(q+1)\times(q+1)$ block matrix with the $\boldsymbol{X}_{\boldsymbol{x^*}}^{*T}\boldsymbol{\omega}\boldsymbol{X}_{\boldsymbol{x^*}}^*=\begin{bmatrix}S_{11} & S_{12} & S_{13} & \cdots\\ S_{21} & S_{22} & S_{23} & \cdots\\ S_{31} & S_{32} & S_{33} & \cdots\\ \vdots & \vdots & \vdots & \ddots\end{bmatrix}$ structure in equation (15). Here the block elements are $S_{11}=\sum_{i=1}^{n}K_{\boldsymbol{H}}(\boldsymbol{x_i^*}-\boldsymbol{x^*})$, $S_{12}=S_{21}^T=\sum_{i=1}^{n}(\boldsymbol{x_i^*}-\boldsymbol{x^*})^TK_{\boldsymbol{H}}(\boldsymbol{x_i^*}-\boldsymbol{x^*})$, $S_{22}=\sum_{i=1}^{n}(\boldsymbol{x_i^*}-\boldsymbol{x^*})(\boldsymbol{x_i^*}-\boldsymbol{x^*})^TK_{\boldsymbol{H}}(\boldsymbol{x_i^*}-\boldsymbol{x^*})$, $S_{13}=S_{31}^T=\sum_{i=1}^{n}vech^T\{(\boldsymbol{x}_1^*-\boldsymbol{x}^*)(\boldsymbol{x}_1^*-\boldsymbol{x}^*)^T)\}K_{\boldsymbol{H}}(\boldsymbol{x_i^*}-\boldsymbol{x^*})$, $S_{23}=S_{32}^T=\sum_{i=1}^{n}(\boldsymbol{x_i^*}-\boldsymbol{x^*})vech^T\{(\boldsymbol{x}_1^*-\boldsymbol{x}^*)(\boldsymbol{x}_1^*-\boldsymbol{x}^*)^T)\}K_{\boldsymbol{H}}(\boldsymbol{x_i^*}-\boldsymbol{x^*})$, and $S_{33}=\sum_{i=1}^{n}vech\{(\boldsymbol{x}_1^*-\boldsymbol{x}^*)(\boldsymbol{x}_1^*-\boldsymbol{x}^*)^T)\}vech^T\{(\boldsymbol{x}_1^*-\boldsymbol{x}^*)(\boldsymbol{x}_1^*-\boldsymbol{x}^*)^T)\}K_{\boldsymbol{H}}(\boldsymbol{x_i^*}-\boldsymbol{x^*})$,… Then the weights become, for $q=0$ $\boldsymbol{\omega}(x^*;0)=\frac{K_{\boldsymbol{H}}(\boldsymbol{x_i^*}-\boldsymbol{x^*})}{S_{11}}$ similar to equation (2), for $=1$ $\boldsymbol{\omega}(x^*;1)=\frac{\{1-S_{12}S_{22}^{-1}(\boldsymbol{x_i^*}-\boldsymbol{x^*})\}K_{\boldsymbol{H}}(\boldsymbol{x_i^*}-\boldsymbol{x^*})}{S_{11}-S_{12}S_{22}^{-1}S_{21}}$, and for $q=2$ $\boldsymbol{\omega}(x^*;2)=\frac{\left\{1-S_{12}S_{22}^{-1}(\boldsymbol{x_i^*}-\boldsymbol{x^*})-S_{13}S_{33}^{-1}vech\{(\boldsymbol{x}_1^*-\boldsymbol{x}^*)(\boldsymbol{x}_1^*-\boldsymbol{x}^*)^T)\}\right\}K_{\boldsymbol{H}}(\boldsymbol{x_i^*}-\boldsymbol{x^*})}{S_{11}-S_{12}S_{22}^{-1}S_{21}-S_{13}S_{33}^{-1}S_{31}}$.

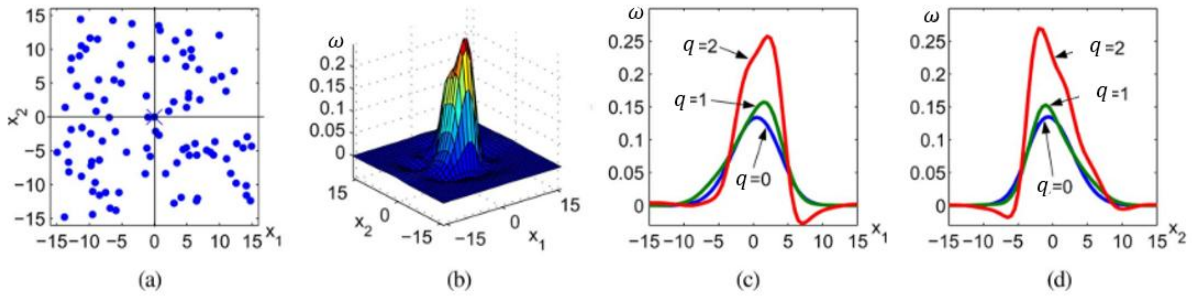

Figure 3. Comparison of kernels for different values of q: (a) irregularly sampled data set, (b) kernel corrector obtained with second-order ($q = 2$) polynomial kernel regression, (c and d) horizontal and vertical sections of correctors with different degrees ($q = 0, 1, 2$) [1].

3.1.1 Data Adapted Partially Linear Regression

In this section, data-adapted partially linear regression methods which take into account not only the spatial sampling density of the data, but also the actual (pixel) values of those samples are introduced. These more sophisticated methods lead to locally adaptive nonlinear extensions of classic kernel regression [1].

Data-adapted partially linear regression methods take into account not only the spatial location and density of the samples but also their radiometric properties. As a result, the size and shape of the regression kernel are locally adjusted to align with image features, such as edges. This approach is structured similarly to (10),

$$\underset{\{\boldsymbol{\theta}_q\}}{min} \sum_{i=1}^{n} [y_i - \boldsymbol{x}_i\beta - \theta_0 - \boldsymbol{\theta}_1^T(\boldsymbol{x}_i^* - \boldsymbol{x}^*) - \boldsymbol{\theta}_2^T vech\{(\boldsymbol{x}_i^* - \boldsymbol{x}^*)(\boldsymbol{x}_i^* - \boldsymbol{x}^*)^T\} \dots]^2 K_{ad}(\boldsymbol{x}_i^* - \boldsymbol{x}^*, y_i - \boldsymbol{x}_i\beta - y - \boldsymbol{x}\beta) \quad (16)$$

where the optimization problem involves a data adapted kernel function K_{ad} that is adapted to the spatial sample locations $\boldsymbol{x}_i^*$s, the sample density, and the radiometric values $y_i - \boldsymbol{x}_i\beta$ of the data.

[1] suggested bilateral kernel, steering kernel and iterative steering kernel regression for the selection of K_{ad}. While bilateral kernel is a data adapted version of NWE, steering kernel is is more appropriate for very noisy data sets, $(y_i - \boldsymbol{x}_i\beta - y - \boldsymbol{x}\beta)$s tend to be zero, and effectively useless. Because iterative steering kernel regression is founded more effective we used this approach for the selection of K_{ad}.

In image processing, partial linear regression is a powerful tool for modeling nonparametric relationships on image data. This methodology allows meaningful analysis of data obtained from image processing and plays a significant role in scientific discoveries. In this technique, relationships between parametric and nonparametric components are examined on image pixels or feature vectors. Initially, high-resolution image data is obtained, and preprocessing steps are performed to analyze this data. Relationships between dependent variables (usually grayscale values or feature vectors) and independent variables (e.g., a feature vector) in the image data can be modeled with parametric and nonparametric components. The obtained parameters and estimates are used to understand the behavior of a specific feature or variable in image processing. For example, the relationship or impact of a specific feature with other features in an image can be examined.

3.2. Application

In image processing and computer vision systems, using partial linear models aims to reduce or completely eliminate the effects of distortions (such as blurring). This process is an optimization effort to obtain the original image from a distorted one [7]. The process is handled as follows in the study:

1. First, the distorted image and the distortion kernel used are defined. This kernel expresses how the distortion occurs.

2. Then, a convolution filter or algorithm is designed for this kernel.

3. Finally, this filter is applied to the distorted image to obtain a clearer or sharper version of the original image.

In image processing, the predicted improved pixel value for each pixel in the blurred image becomes the enhanced pixel value calculated for the parametric component. For the parametric equation $Y = \beta_0 + \beta_1 X_1$, Y represents the pixel value of the predicted image, β_0 represents the expected pixel value of the improved image when the pixel value in the noisy image is 0, and β_1 represents the change in the pixel value of the improved image when the pixel value in the noisy image increases by 1 unit.

For the nonparametric equation $Y = g(\boldsymbol{x}^*)$, Y represents the pixel value of the predicted image, and the function $g(\boldsymbol{x}^*)$ represents the kernel used to model the nonparametric relationship between the pixel values of the blurred image and the pixel values of the improved image.

3.2.1 Partially Linear Regression Algorithm for Blurred Images and Application Images Obtained

Image Creation:

- Input: Path of an image file.
- Output: A blurred black-and-white image

The image file is read, resized with a certain scaling ratio, and converted to grayscale.

Applying Gaussian Filter:

- Input: Blurred image.
- Output: Image with Gaussian filter applied.

A Gaussian kernel is created, and the Gaussian filter is applied to the image.

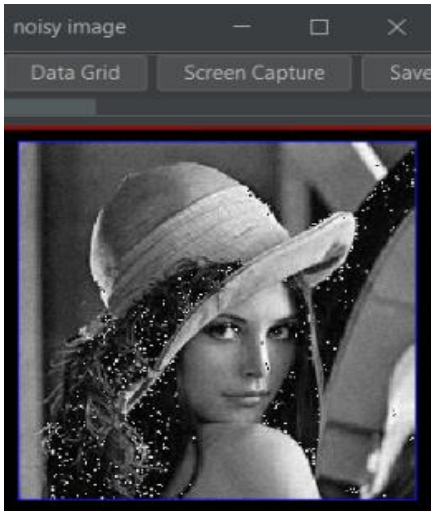

Figure 4. Noisy input image

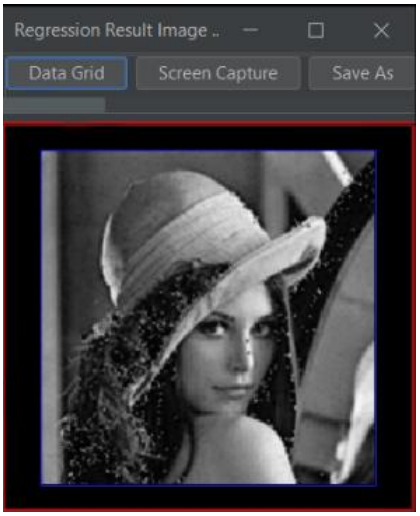

Figure 5. Image with Gaussian filter applied

Applying Histogram Equalization:

- Input: Image with Gaussian filter applied.
- Output: Image with histogram equalization applied

The histogram of the image is calculated, the cumulative distribution of the histogram is examined, and a new pixel value is created by matching each pixel value with the cumulative histogram. An improved image is obtained with new pixel values.

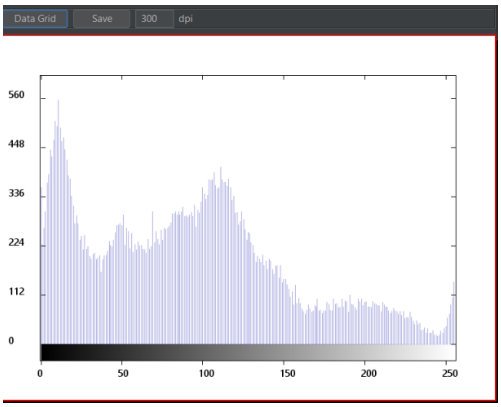

Figure 6. Histogram of the noisy image

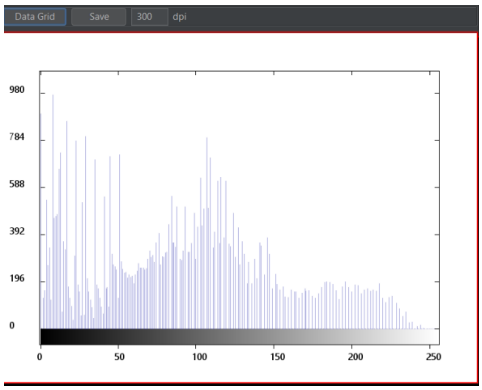

Figure 7. Histogram of the processed image

Applying Partially Linear Regression:

- Input: Blurred and improved images.
- Output: Regression result.

The pixel values of blurred and improved images are collected in pairs. Using data adaptive partially linear regression with the integrated weighting parameter q demonstrates the robustness and adaptability of the proposed approach; the relationship between these pixel pairs is found (regression coefficients are calculated). A new image is created using the calculated regression coefficients.

Displaying Results:

- Input: Images resulting from different processing steps.
- Output: Visual display of the images.

Original, noisy, blurred, improved, and regression result images, which show the effect of the q parameter for 0, 1 and 2, respectively, on image enhancement and deconvolution, are displayed.

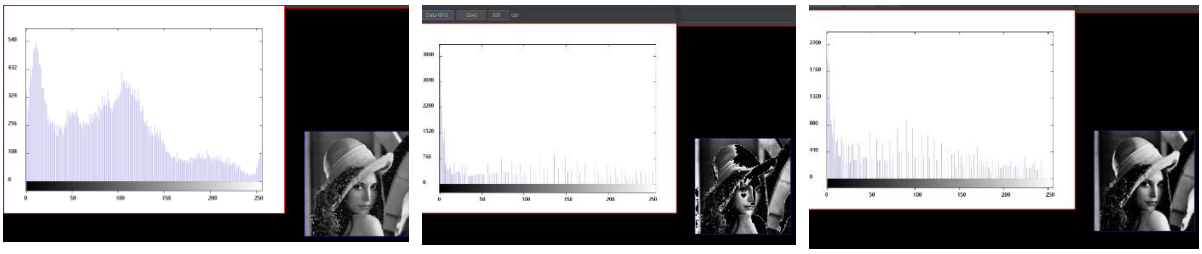

(a) $q = 0$ (b) $q = 1$ (c) $q = 2$

Figure 8. Corrected regression images for $q = 0, 1$ and 2.

Here, Figure 8(a) demonstrates the original distorted image showing significant blur due to the distortion kernel. This is used as the basis for comparison. Figure 8(b) demonstrates an enhanced image generated using standard kernel regression without data adaptation. Although edges are slightly sharper, noise and artifacts persist, especially in areas with complex textures, and Figure 8(c) demonstrates enhanced image generated using partial linear regression model with data adaptation. With the addition of q-weighting parameter, the algorithm exhibited superior performance in edge preservation and noise

reduction. Locally adaptive kernel provides a clearer and more detailed reconstruction by better adapting to image features.

The results are consistent with the theoretical framework discussed in Section 3.1.1. In this section, a data adaptive kernel function was proposed. By adding q-weight, the kernel dynamically adapts by considering both spatial sampling density and pixel features. This leads to the following results:

Improved Edge Preservation: The kernel reduces over-smoothing by adapting its shape and size according to local image features such as edges and texture.

Improved Noise Robustness: The q-parameter affects the regression by weighting regions with high variance or noise, thus preserving critical details in noisy regions while preserving smoother areas.

Iterative Refinement: The iterative guidance kernel regression approach gradually improves the enhanced image by recalculating the kernel, including the locally optimized parameters q.

4. Conclusion

It was observed that as the noise level increased, the image quality decreased. Statistical analyses of the images obtained during this process were performed. Gaussian blurring was applied to the frequency of the noisy image to reduce noise. This application aimed to eliminate noise by softening sharp edges in the image, demonstrating the effectiveness of Gaussian blurring in noise reduction.

In this study, where partially linear regression analysis was applied, the relationship modeling between blurred and improved images was successfully implemented. The operation became an effective modeling approach for processing blurred images. In noise reduction and image smoothing operations image processing techniques are very important.

The partially linear regression operations is demonstrated that each operation, such as reducing or eliminating blurring and increasing contrast, significantly improved image quality. The results obtained showed that the operation would facilitate everyday applications (e.g., medical imaging devices, security cameras, and satellite images). Testing future studies with images obtained under different conditions and larger data sets will allow for a more comprehensive evaluation of the proposed methods' general validity.

Ethical statement

The authors declare that this document does not require ethics committee approval or any special permission. Our study does not cause any harm to the environment and does not involve the use of animal or human subjects.

Acknowledgment

This study was produced from Merve Bingöl Sukutlis' master's thesis named ''The use of partially linear regression model with measurement error in image processing'' in the department of statistics at the Dicle University Institute of Science and supported by Dicle University Scientific Research Projects Unit under Project No. DÜBAP-FEN.23.023. The authors thank Musa Ataş from Siirt University for valuable contributions to conduct the research.

Conflict of interest

The authors declare that this document has not conflict of interest.

Authors' Contributions

All authors contributed to the study conception and design. Material preparation, data collection and analysis were performed by M. B. (%60). The first draft of the manuscript was written by S. Y. (%40) and all authors commented on previous versions of the manuscript. All authors read and approved the final manuscript.

Generative AI statement

The author(s) declare that no Gen AI was used in the creation of this manuscript.

References

[1] Takeda, H., Farsiu, S., Milanfar, P., "Kernel Regression for Image Processing and Reconstruction", *IEEE Transactions on Image Processing*, 16(2), 349-366, 2007.

[2] Montgomery, D.C., Peck, E.A., Vining, G.G., *Introduction to Linear Regression Analysis*. 5th ed., John Wiley & Sons, New York, 2012.

[3] Ni, K., Nguyen, T., "Image Superresolution Using Support Vector Regression", *IEEE Transactions on Image Processing*, 16, 1596-1610, 2007.

[4] Tomasi, C., Manduchi, R., "Bilateral filtering for gray and color images", Proceeding of IEEE Int. Conf. Computer Vision, New Delhi, India, 1998, pp. 836-846.

[5] Toprak, S., Partially Linear Regression Models with Measurement Errors, PhD thesis, Dicle University, Diyarbakır, Turkey, 2015.

[6] Yalaz, S., Tez, M., "Partially linear multivariate regression in the presence of measurement error", *Communications for Statistical Applications and Methods*, 27, 511-521, 2020.

[7] Ataş, M., "Open Cezeri Library: A novel java based matrix and computer vision framework", *Computer Applications in Engineering Education*, 24(5), 736-743, 2016.

Middle East Journal of Science

https://dergipark.org.tr/mejs

MEJS

e-ISSN:2618-6136

Research Article

DECISION MAKING WITH BIJECTIVE SOFT ROUGH SET MODEL

Nurettin BAĞIRMAZ

Vocational Higher Schools of Mardin, Mardin Artuklu University, Mardin, Türkiye
Corresponding author: nurettinbagirmaz@artuklu.edu.tr

Abstract: *Rough sets and soft sets are two important mathematical tools for dealing with uncertainty. Methods that combine properties of both sets can provide more effective solutions in certain applications. This paper aims to present an application of one such method, bijective soft rough sets. Subsequently, an algorithm based on bijective soft rough sets for decision making is developed and a real-life application of the proposed method is presented*

Keywords*: Rough sets, soft sets, bijective soft sets, bijective soft rough sets, decision making method.*

Received: April 16, 2025 *Accepted: June 12, 2025*

1. Introduction

Real-life applications often require more advanced and efficient mathematical tools to deal with uncertainties. Data associated with complex problems in engineering, marketing, medical science, environmental science and other fields often contain various types of incomplete information. Therefore, various mathematical theories such as fuzzy set theory [1], intuitionistic fuzzy set theory [2], uncertain set theory [3], and rough set theory [4] have been developed to handle uncertain situations and draw meaningful conclusions. While all these theories are valuable tools for describing imprecision, each possesses inherent complexities, as highlighted by Molodtsov [5].

To address these challenges, Molodtsov [5] introduced soft set theory, which has since gained recognition as an effective approach for handling uncertainty. In recent years, substantial advancements have been made in both its theoretical underpinnings and practical implementations. Maji et al. [6] enhanced the field by formulating algebraic operations for soft sets and providing an in-depth theoretical analysis. In [7], Ali et al. contributed to the theory with the definition of new operations such as restricted union, intersection and difference. The effectiveness of soft sets in decision-making scenarios was highlighted by Maji et al. [8], and Chen et al. [9] focused on parameter reduction techniques within soft sets, drawing comparisons with feature reduction in rough set theory. Moreover, Gong et al. [10] introduced the concept of bijective soft sets, outlining their key operations. In [11], Aktaş presented the concept of bijective soft groups and discussed their potential applications. Koyuncu introduced bijective soft rings and explored their applications in [12]. Recent research has further explored the potential applications of these bijective soft sets [13–14].

Rough set theory, originally created by Pawlak [4], is another powerful mathematical instrument for dealing with vagueness and granularity in information systems. It approximates uncertain or inexact concepts using lower and upper approximation sets. This approach has proved essential in numerous domains, including data analysis, mereology, image processing, intelligent systems, and knowledge discovery in databases [15–19].

Despite their individual strengths, these theories may not always yield optimal results when used in isolation. As well, researchers have explored hybrid approaches that combine the strengths of different models. For instance, Herawan and Deris [20] revisited the rough set models of Pawlak and Iwinski through the lens of soft set theory. In [21], several hybrid models—such as soft rough sets, rough soft sets, and soft rough fuzzy sets—were introduced. Feng et al. [22] further explored the concept of soft rough sets, representing an integration of soft and rough set theories. Over time, numerous studies have examined the application of such hybrid models to decision-making problems [23–25]. Recently, a new unification of soft and rough set theories has been proposed by Bağırmaz [26] in the form of bijective soft rough sets.

This study introduces a fresh hybrid framework that is compatible with rough set theory while preserving the essential properties of soft sets. A decision methodology built on bijective soft rough sets is developed, including a detailed algorithm and a practical application that demonstrates the usefulness of the proposed model.

2. Preliminaries

Key concepts and definitions of rough sets, soft sets, soft rough sets, bijective soft sets, bijective soft rough sets and similar structures are sketched in this part.

Definition 2.1 [4] Let's take a non-empty set U and an equivalence relation θ on the set U. *In* this case, the pair (U,θ) is called the approximation space. The equivalence class of $a \in U$ is denoted by $\theta(a)$. For a subset $X \subseteq U$,

$$\underline{X} = \underset{a\in U}{\cup} \{\theta(a): \theta(a) \subseteq X\},$$

$$\overline{X} = \underset{a\in U}{\cup} \{\theta(a): \theta(a) \cap X \neq \emptyset\}.$$

The sets $\underline{X}, \overline{X}$ are called the lower and upper approximations of X with respect to (U,θ), respectively. $Bnd(X) = \overline{X} - \underline{X}$ is called rough boundary regions of X. If $Bnd(X) = \emptyset$; X is said to be rough definable; otherwise X is called a rough set.

Definition 2.3 [5] Let U be a certain set called the universe, and E be a set of parameters representing the properties of the elements in U. If $A \subseteq E$ and $f: A \to P(U)$ is a set-valued mapping, a pair $S = (f, A)$ is called a soft set on U.

Definition 2.4 [6] Let (f, A) and (g, B) be two soft sets over U. Then (f, A) is called a soft subset of (g, B), denoted by $(f, A) \tilde{\subset} (g, B)$, if $A \subseteq B$ and $\forall\, e \in A$, $f(e)$ and $g(e)$ have the same approximations.

Definition 2.5 [6] Let (f, A) and (g, B) be two soft sets over U. The union of (f, A) and (g, B) is defined as (h, C), where $C = A \cup B$ and for all $e \in C$,

$$h(e) = \begin{cases} f(e), if e \in A \backslash B, \\ g(e), if e \in B \backslash A, \\ f(e) \cup g(e), if\ \ e \in A \cap B \end{cases}$$

This is denoted by $(f, A) \tilde{\cup} (g, B) = (h, C)$.

Definition 2.6 [2] If (f, A) and (g, B) are two soft sets then *"*(f, A) *AND* (g, B)*"* (also denoted as $(f, A) \wedge (f, B)$) is defined by $(f, A) \wedge (f, B) = (h, A \times B)$, where $h(a, b) = f(a) \cap g(b)$ for all $(a, b) \in A \times B$.

Definition 2.7 [10] Let (f, A) be a soft set on U, where f is a set-valued mapping $f: A \to P(U)$

and A is a non-empty set of parameters. (f, A) is called a bijective soft set if it satisfies the following conditions:

1. $\cup_{e\in A} f(e) = U$,
2. For two arbitrary parameters $e_i, e_j \in A$, $e_i \neq e_j$, $f(e_i) \cap f(e_j) = \emptyset$.

Example 2.8 Let (f, E) be a soft set over the set $U = \{a_1, a_2, a_3, a_4, a_5\}$ and set of parameters $E = \{e_1, e_2, e_3, e_4\}$. *Let* $A = \{e_1, e_2, e_3\}$, $B = \{e_2, e_4\}$.

Let the mapping (f, E) be given by

$$f(e_1) = \{a_1\}, f(e_2) = \{a_2, a_4\}, f(e_3) = \{a_3, a_5\}, f(e_4) = \{a_1, a_3, a_4\}.$$

From Definition 2.7, (f, A) is bijective soft set. Whereas (f, B) is not bijective soft set.

Proposition 2.9 [10] If (f, A) and (g, B) are two bijective soft sets over U, then $(h, C) = (f, A) \wedge (g, B)$ is also a bijective soft set.

Definition 2.10 [22] Let (f, A) be a soft set over the universe U. In this case, the triple (U, f, A) is referred to as a soft approximation space. Depending on (U, f, A), for any subset X of U, following two operators are defined

$$\underline{A}(\mathrm{X}) = \{x \in U: \exists e \in A[x \in f(e) \subseteq X]\},$$
$$\overline{A}(\mathrm{X}) = \{x \in U: \exists e \in A[x \in f(e), f(e) \cap X \neq \emptyset]\}.$$

The subsets $\underline{A}(\mathrm{X})$ and $\overline{A}(\mathrm{X})$ are called the lower and upper soft rough approximations of X on (U, f, A), respectively.

A rough set is given by a universe set U and an equivalence relation $\theta \subseteq U \times U$ in the well-known Pawlak approximation space. In the notion of a subjective soft set, each item in the universe can be mapped to only one parameter, and the union of the partitions formed by these parameters constitutes the universe of discussion. According to Definition 2.7, since the expression $\mathfrak{C} = \{f(e_1), f(e_2), \ldots, f(e_n)\}$, $e_1, e_2, \ldots, e_n \in A$, is both a partition and a cover of the universe, the expression $f(e)$ can be considered as an equivalence class of e. In this context, the structure of the universe can be analysed in the framework of a subjective soft set.

Let (f, A) be a bijective soft set on U. Then, corresponding pair $\mathfrak{B} = (U, f, A)$ is called a bijective soft rough approximation space. Then, the set $\mathfrak{C} = \{f(e_1), f(e_2), \ldots, f(e_n)\}$, where $e_1, e_2, \ldots, e_n$ are elements of A, will be called a class of values and can be defined by the equivalence relation $\theta \subseteq U \times U$, defined as follows $(x, y) \in \theta \Leftrightarrow x, y \in f(e)$ for all $x, y \in U$ and only one $e \in A$. Thus

$\theta(x) = f(e) \Leftrightarrow x \in f(e)$. Therefore, we can identify the notion of the class of values $\mathfrak{C}_A$ of the bijective soft set (f, A) and the quotient set U / θ in $\mathfrak{B} = (U, f, A)$.

Definition 2.11 [26] Let (f, A) be a bijective soft set over U and $\mathfrak{B} = (U, f, A)$ be a bijective soft rough approximation space. Let X be a nonempty subset of U. Then the sets

$$\underline{A}_{\mathfrak{B}}(X) = \underset{e\in A}{\cup} \{f(e): f(e) \subseteq X\} \text{ and } \overline{A}_{\mathfrak{B}}(X) = \underset{e\in A}{\cup} \{f(e): f(e) \cap X \neq \emptyset\}$$

are called, respectively, lower and upper bijective soft rough approximations of X based on $\mathfrak{B} = (U, f, A)$.

Moreover, $Bnd_{\mathfrak{B}}(X) = \overline{A}_{\mathfrak{B}}(X) - \underline{A}_{\mathfrak{B}}(X)$ is called bijective soft rough boundary regions of X. If $Bnd_{\mathfrak{B}}(X) = \emptyset$, X is said to be bijective soft rough definable; otherwise X is called a bijective soft rough

set.

From this point on, throughout this study, each bijective soft set (f, A) defined over the universe U will be considered together with its corresponding bijective soft rough approximation space $\mathfrak{B} = (U, f, A)$, and for convenience will be denoted as $(f, A) \in \mathfrak{B}$.

Example 2.12 Let the soft set (f, E) be defined on the set $U = \{x_1, x_2, x_3, x_4, x_5\}$ with parameters $E = \{e_1, e_2, e_3, e_4, e_5\}$. The mapping of (f, E) is as follows:

$$f(e_1) = \{x_1, x_2\}, f(e_2) = \{x_3, x_4, x_5\}, f(e_3) = \{x_1, x_2, x_3\}, f(e_4) = \{x_4\} \text{ and } f(e_5) = \{x_5\}.$$

We can tabulate this soft set as shown in Table 1. If $x_i \in f(e)$ then $x_{ij} = 1$, otherwise $x_{ij} = 0$, where x_{ij} are the entries Table 1.

Table 1. Soft set (f, E).

	e_1	e_2	e_3	e_4	e_5
x_1	1	0	1	0	0
x_2	1	0	0	1	0
x_3	0	1	0	0	1
x_4	0	1	0	0	1
x_5	0	1	0	1	0

Let $A = \{e_1, e_2\} \subseteq E$, $B = \{e_3, e_4, e_5\} \subseteq E$. From Definition 2.7, (f, A) and (f, B) are bijective soft sets.

Then

$$\mathfrak{C}_A = \{f(e_1), f(e_2)\} = \{\{x_1, x_2\}, \{x_3, x_4, x_5\}\},$$
$$\mathfrak{C}_B = \{f(e_3), f(e_4), f(e_5)\} = \{\{x_1\}, \{x_2, x_5\}, \{x_3, x_4\}\}.$$

For $X = \{x_1, x_2, x_4\} \subseteq U$ and $Y = \{x_3, x_5\} \subseteq U$ we can write

$$\underline{A}_{\mathfrak{B}}(X) = \{x_1, x_2\},\ \overline{A}_{\mathfrak{B}}(X) = U$$

and

$$\underline{B}_{\mathfrak{B}}(Y) = \emptyset,\ \overline{B}_{\mathfrak{B}}(Y) = \{x_2, x_3, x_4, x_5\}.$$

Thus, by Definition 2.11, X and Y are bijective soft rough sets.

Proposition 2.13 [26] Let $S = (f, A) \in \mathfrak{B}$. Then, for every $X, Y \subseteq U$ following properties hold:

1. $\underline{A}_{\mathfrak{B}}(X) \subset X \subset \overline{A}_{\mathfrak{B}}(X)$,
2. $\underline{A}_{\mathfrak{B}}(\emptyset) = \overline{A}_{\mathfrak{B}}(\emptyset) = \emptyset$,
3. $\underline{A}_{\mathfrak{B}}(U) = \overline{A}_{\mathfrak{B}}(U) = U$,
4. $\underline{A}_{\mathfrak{B}}(X \cap Y) = \underline{A}_{\mathfrak{B}}(X) \cap \underline{A}_{\mathfrak{B}}(Y)$,
5. $\overline{A}_{\mathfrak{B}}(X \cup Y) = \overline{A}_{\mathfrak{B}}(X) \cup \overline{A}_{\mathfrak{B}}(Y)$,
6. $X \subset Y \Rightarrow \underline{A}_{\mathfrak{B}}(X) \subset \underline{A}_{\mathfrak{B}}(Y)$,

7. $X \subset Y \Rightarrow \overline{A}_{\mathfrak{B}}(X) \subset \overline{A}_{\mathfrak{B}}(Y)$,

8. $\overline{A}_{\mathfrak{B}}(X \cap Y) \subseteq \overline{A}_{\mathfrak{B}}(X) \cap \overline{A}_{\mathfrak{B}}(Y)$,

9. $\underline{A}_{\mathfrak{B}}(X \cup Y) \supseteq \underline{A}_{\mathfrak{B}}(X) \cup \underline{A}_{\mathfrak{B}}(Y)$.

Definition 2.14 [26] Let $(f, A), (g, B) \in \mathfrak{B}$. Then we can define the following two operations on bijective soft rough set $(h, C) = (f, A) \wedge (g, B)$; for every subset $X \subseteq U$

$$\underline{C}_{\mathfrak{B}}(X) = \bigcup_{e \in C} \{h(e): h(e) \subseteq X\},$$
$$\overline{C}_{\mathfrak{B}}(X) = \bigcup_{e \in C} \{h(e): h(e) \cap X \neq \emptyset\},$$

where $h(e) = f(a) \cap g(b), \forall e = (a, b) \in A \times B$.

Proposition 2.15 [26] Let $(f, A), (g, B) \in \mathfrak{B}$. Then approximation on $(h, C) = (f, A) \wedge (g, B)$, for every $X \subseteq U$ following properties hold:

1. $\underline{C}_{\mathfrak{B}}(X) \supseteq \underline{A}_{\mathfrak{B}}(X) \cap \underline{B}_{\mathfrak{B}}(X)$,

2. $\overline{C}_{\mathfrak{B}}(X) \subseteq \overline{A}_{\mathfrak{B}}(X) \cap \overline{B}_{\mathfrak{B}}(X)$.

Example 2.16 We reconsider the bijective soft sets (f, A) and (f, B) given in Example 2.12. For $X = \{x_1, x_2, x_4\} \subseteq U = \{x_1, x_2, x_3, x_4, x_5\}$, we obtain

$$\underline{A}_{\mathfrak{B}}(X) = \{x_1, x_2\}, \ \overline{A}_{\mathfrak{B}}(X) = U$$

and

$$\underline{B}_{\mathfrak{B}}(X) = \{x_1\}, \ \overline{B}_{\mathfrak{B}}(X) = U.$$

Also

$$\underline{A}_{\mathfrak{B}}(X) \cap \underline{B}_{\mathfrak{B}}(X) = \{x_1\},$$

and

$$\overline{A}_{\mathfrak{B}}(X) \cap \overline{B}_{\mathfrak{B}}(X) = U.$$

Now taking $(h, C) = (f, A) \wedge (f, B), h(e) = f(a) \cap f(b), \forall e = (a, b) \in A \times B$.
Then we obtain

$$\mathfrak{C}_C = \{h(e_1), h(e_2), h(e_3), h(e_4)\} = \{\{x_1\}, \{x_2\}, \{x_3, x_4\}, \{x_5\}\}$$

and

$$\underline{C}_{\mathfrak{B}}(X) = \{x_1, x_2\}, \ \overline{C}_{\mathfrak{B}}(X) = \{x_1, x_2, x_3, x_4\}.$$

Thus

$$\underline{C}_{\mathfrak{B}}(X) \not\subseteq \underline{A}_{\mathfrak{B}}(X) \cap \underline{B}_{\mathfrak{B}}(X) \text{ and } \overline{A}_{\mathfrak{B}}(X) \cap \overline{B}_{\mathfrak{B}}(X) \not\subseteq \overline{C}_{\mathfrak{B}}(X)$$

Corollary 2.17 [26] Let $(f_i, A_i) \in \mathfrak{B}$, where $(i = 1,2,3, \ldots, n)$. Then approximations on $(h_n, C_n) = \wedge_{i=1}^{n} (f_i, A_i)$, for every $X \subseteq U$ following properties hold:

1. $\left(\underline{C_n}\right)_{\mathfrak{B}}(X) \supseteq \cap_{i=1}^{n} \left(\underline{A_i}\right)_{\mathfrak{B}}(X)$,

2. $\left(\overline{C_n}\right)_{\mathfrak{B}}(X) \subseteq \cap_{i=1}^{n} \left(\overline{A_i}\right)_{\mathfrak{B}}(X)$.

Proposition 2.18 [26] Let $(f_i, A_i) \in \mathfrak{B}$, where $(\mathrm{i} = 1,2,3, \ldots, \mathrm{n})$. Then approximations on

$(h_n, C_n) = \wedge_{i=1}^{n} (f_i, A_i)$, for every $X \subseteq U$ following properties hold:

1. $\left(\underline{C_n}\right)_{\mathfrak{B}}(X) \supseteq \left(\underline{C_m}\right)_{\mathfrak{B}}(X)$,
2. $\left(\overline{C_n}\right)_{\mathfrak{B}}(X) \subseteq \left(\overline{C_m}\right)_{\mathfrak{B}}(X)$,

where $m \leq n$.

Definition 2.19 [26] Let $(f, A) \in \mathfrak{B}$. The accuracy measure of any subset $X \subseteq U$ with respect to A is defined as

$$\beta_{\mathfrak{B}}^{A}(X) = \frac{\left|\underline{A}_{\mathfrak{B}}(X)\right|}{\left|\overline{A}_{\mathfrak{B}}(X)\right|}.$$

Obviously $0 \leq \beta_{\mathfrak{B}}^{A}(X) \leq 1$. If $\beta_{\mathfrak{B}}^{A}(X) = 1$, X is crisp with respect to A, and otherwise, if $\beta_{\mathfrak{B}}^{A}(X) < 1$, X is bijective soft rough with respect to A.

Let us depict above definition by examples referring to Example 2.16.

For $X = \{x_1, x_2, x_4\} \subseteq U$ and $A \subseteq E$ we have $\underline{A}_{\mathfrak{B}}(X) = \{x_1, x_2\}$, $\overline{A}_{\mathfrak{B}}(X) = U$. For this case $\beta_{\mathfrak{B}}^{A}(X) = \frac{\left|\underline{A}_{\mathfrak{B}}(X)\right|}{\left|\overline{A}_{\mathfrak{B}}(X)\right|} = \frac{2}{5}$.

It means that the parameter set A is less characteristic for X.

For $X = \{x_1, x_2, x_4\} \subseteq U$ and $B \subseteq E$ we have $\underline{B}_{\mathfrak{B}}(X) = \{x_1\}$, $\overline{B}_{\mathfrak{B}}(X) = U$. For this case $\beta_{\mathfrak{B}}^{B}(X) = \frac{\left|\underline{B}_{\mathfrak{B}}(X)\right|}{\left|\overline{B}_{\mathfrak{B}}(X)\right|} = \frac{1}{5}$.

It means that this parameter set B is much less characteristic for X.

For $X = \{x_1, x_2, x_4\} \subseteq U$ and $C \subseteq E$ we have $\underline{C}_{\mathfrak{B}}(X) = \{x_1, x_2\}$, $\overline{C}_{\mathfrak{B}}(X) = \{x_1, x_2, x_3, x_4\}$. For this case $\beta_{\mathfrak{B}}^{C}(X) = \frac{\left|\underline{C}_{\mathfrak{B}}(X)\right|}{\left|\overline{C}_{\mathfrak{B}}(X)\right|} = \frac{2}{4}$. It means that the set X can be characterized partially by parameter sets A and B.

Proposition 2.20 [26] Let $(f_i, A_i) \in \mathfrak{B}$, where $(i = 1,2,3,\ldots,n)$. Let $(h_n, C_n) = \wedge_{i=1}^{n} (f_i, A_i)$. Then, for every $X \subseteq U$ and $m \leq n$,

$$\beta_{\mathfrak{B}}^{C_m}(X) \leq \beta_{\mathfrak{B}}^{C_n}(X).$$

3. Bijective soft rough sets in decision making

Concepts for creating a decision method using bijective soft rough sets are presented in here. It also includes a decision algorithm and an application of the proposed method.

Definition 3.1 Let $(f, A) \in \mathfrak{B}$ and let $(g, B) \in \mathfrak{B}$ be a bijective soft rough set. Then, accuracy measure of parameter $e \in B$ with respect to A is defined as

$$\beta_{\mathfrak{B}}^{A}\big(g(e)\big) = \frac{\left|\underline{A}_{\mathfrak{B}}(g(e))\right|}{\left|\overline{A}_{\mathfrak{B}}(g(e))\right|}.$$

The accuracy measure of bijective soft rough set (g, B) with respect to A, denoted by $\sigma_{\mathfrak{B}}^{A}(g)$, is defined as

$$\sigma_{\mathfrak{B}}^{A}(g) = \frac{1}{|B|} \sum_{e \in B} \beta_{\mathfrak{B}}^{A}\big(g(e)\big).$$

Definition 3.2 Let $(f_i, A_i), (g, B) \in \mathfrak{B}$, where $(\mathrm{i} = 1,2,\ldots,\mathrm{n})$, and $(h_n, C_n) = \wedge_{i=1}^{n} (f_i, A_i)$. If $\sigma_{\mathfrak{B}}^{C_n}(g) = \sigma_{\mathfrak{B}}^{C_m}(g)$, where $m < n$, then, we call the soft set $(f', A') = \tilde{\cup}_{i=1}^{m} (f_i, A_i)$ is a reduct of the soft set $(f, A) = \tilde{\cup}_{i=1}^{n} (f_i, A_i)$.

Definition 3.3 Let $(f, A) \in \mathfrak{B}$ and let $(g, B) \in \mathfrak{B}$ be a bijective soft rough set. Then, certainty measure of decision parameter $e_j \in B$ with the help *of* $e_i \in A$ *is defined as*

$$d^{e_i}(e_j) = \frac{|f(e_i) \cap g(e_j)|}{|f(e_i)|},$$

where $e_i \in A$ and $e_j \in B$.

Definition 3.4 Let $(f, A) \in \mathfrak{B}$ and let $(g, B) \in \mathfrak{B}$ be a bijective soft rough set. Then, a decision rule is defined as *"if* e_i then e_j*"* with the certainty measure $d^{e_i}(e_j)$, where $e_i \in A$ and $e_j \in B$.

If $d^{e_i}(e_j) = 1$, then "if e_i then e_j" will be referred to as a certain decision rule; if $0 < d^{e_i}(e_j) < 1$ the decision rule will be considered uncertain.

Now, based on the concepts presented above, the following algorithm will be introduced:

1. Construct bijective soft rough sets (f_i, A_i) and bijective soft rough set (g, B),

2. Compute the accuracy measure $\sigma_{\mathfrak{B}}^{C_i}(g)$ for each bijective soft rough set $\wedge (f_i, A_i)$ by Definition 3.1,

3. Find a reduct bijective soft rough set $(h_m, C_m) = \wedge_{i=1}^{m} (f_i, A_i)$ by Definition 3.2,

4. Find the certainty measure $d^{e_i}(e_j)$ for all $e_j \in B$ with respect to $e_i \in C_m$ by Definition 3.3,

5. Obtain the decision rules by Definition 3.4.

Let us apply the above algorithm on a real life application as follows:

Example 3.5 Let a public health department examine "life expectancy" situation of its citizens according to their some informations to better serve the citizens. Consider the soft set (f, E) representing *"life expectancy"*. Let's assume that the set $U = \{x_1, x_2, x_3, x_4, x_5, x_6, x_7, x_8\}$ consists of eight people and E denotes the parameter set, $E = A_1 \cup A_2 \cup A_3 \cup B$, A_1 describes *"sex"*, A_2 describes *"living area"*, A_3 describes *"habits"* and A_4 describes *"decision"*. The sets of these parameters are $A_1 = \{female, male\}$, $A_2 = \{village, city,\}$, $A_3 = \{smoke, smoke\ and\ drinking, no\ smoke\ no\ drinking\}$ and $B = \{healthy, drug\ addict, under\ stress\}$, respectively. From Definition 2.8 and Definition 2.11, (f_i, A_i) and (g, B) are bijective soft rough subsets of (f, E), where $\mathrm{i} = 1,2,3$. The mapping of each bijective soft rough sets over U defined as Table 2.

Table 2. Table of bijective soft sets for life expectancy.

	e_1	e_2	e_3	e_4	e_5	e_6	e_7	e_8	e_9	$\mathbf{e}_{10}$
x_1	1	0	1	0	0	0	1	1	0	0
x_2	1	0	1	0	0	0	1	1	0	0
x_3	0	1	1	0	1	0	0	1	0	0
x_4	0	1	0	1	0	1	0	0	1	0
x_5	0	1	1	0	1	0	0	0	0	1
x_6	0	1	0	1	0	0	1	1	0	0
x_7	0	1	0	1	0	1	0	0	1	0
x_8	1	0	1	0	1	0	0	0	0	1

We use abbreviation "e_1" for female, "e_2" for male, "e_3" for village, "e_4" for city,"e_5" for smoke, "e_6" for smoke and drinking, "e_7" for no smoke no drinking, "e_8" for healthy, "e_9" for drug addict and "e_{10}" for under stress in the Table 2.

Step 1. According to collected information in Table 2, the mapping of condition bijective soft rough sets (f_i, A_i), $i = 1,2,3$ and the mapping of decision bijective soft rough set (g, B) are given below:

$$f_1(e_1) = \{x_1, x_2, x_8\}, \quad f_1(e_2) = \{x_3, x_4, x_5, x_6, x_7\},$$

$$f_2(e_3) = \{x_1, x_2, x_3, x_5, x_8\}, \quad f_2(e_4) = \{x_4, x_6, x_7\},$$

$$f_3(e_5) = \{x_3, x_5, x_8\}, \; f_3(e_6) = \{x_4, x_7\}, \; f_3(e_7) = \{x_1, x_2, x_6\},$$

$$g(e_8) = \{x_1, x_2, x_3, x_6\}, g(e_9) = \{x_4, x_7\}, \mathrm{g}(e_{10}) = \{x_5, x_8\}.$$

Step 2. We can calculate accuracy measure of bijective soft rough set (f_4, A_4) with respect to $\wedge (f_i, A_i), \mathrm{i} = 1,2,3$, as Table 3 and 4.

Table 3. Table of the accuracy measure of parameters in B for each bijective soft rough set $\wedge (f_i, A_i), \mathrm{i} = 1,2,3$.

	$\beta_{\mathfrak{B}}^{A_1}$	$\beta_{\mathfrak{B}}^{A_2}$	$\beta_{\mathfrak{B}}^{A_3}$	$\beta_{\mathfrak{B}}^{A_{1,2}}$	$\beta_{\mathfrak{B}}^{A_{1,3}}$	$\beta_{\mathfrak{B}}^{A_{2,3}}$	$\beta_{\mathfrak{B}}^{A_{1,2,3}}$
$g(e_8)$	0	0	0	0	0,6	0,33	0,6
$\mathrm{g}(e_9)$	0	0	1	0	1	1	1
$\mathrm{g}(e_{10})$	0	0	0	0	0,33	0	0,33

Table 4. Table of the accuracy measure of bijective soft rough set (g, B) for each bijective soft rough sets $\wedge (f_i, A_i), \mathrm{i} = 1,2,3$.

$\sigma_{\mathfrak{B}}^{A_1}(g)$	$\sigma_{\mathfrak{B}}^{A_2}(g)$	$\sigma_{\mathfrak{B}}^{A_3}(g)$	$\sigma_{\mathfrak{B}}^{A_{1,2}}(g)$	$\sigma_{\mathfrak{B}}^{A_{1,3}}(g)$	$\sigma_{\mathfrak{B}}^{A_{2,3}}(g)$	$\sigma_{\mathfrak{B}}^{A_{1,2,3}}(g)$
0	0	0,33	0	0,57	0,44	0,57

Step 3. From step 2, we have $\sigma_{\mathfrak{B}}^{A_{1,3}}(g) = \sigma_{\mathfrak{B}}^{A_{1,2,3}}(\mathrm{g})$, and so $(f_1, A_1) \tilde{\cup} (f_3, A_3)$ a reduct bijective soft rough set of $\tilde{\cup}_{i=1}^{3} (f_i, A_i)$. Let $(h, C) = (f_1, A_1) \wedge (f_3, A_3)$. The tabular form of (h, C) is given in Table 5, where $\mathrm{c}_i \in C, i = 1,2,3,4,5$.

Table 5. Table for bijective soft rough sets $(h, C) = (f_1, A_1) \wedge (f_3, A_3)$ and (g, B)

	c_1	c_2	c_3	c_4	c_5
x_1	1	0	0	0	0
x_2	1	0	0	0	0
x_3	0	1	0	0	0
x_4	0	0	1	0	0
x_5	0	1	0	0	0
x_6	0	0	0	0	1
x_7	0	0	1	0	0
x_8	0	0	0	1	0

The parameters of C are
$c_1 =$ (female) and (no smoke no drinking),
$c_2 =$ (male) and (smoke),
$c_3 =$ (male) and (smoke and drinking),
$c_4 =$ (female) and (smoke),
$c_5 =$ (male) and (no smoke no drinking).

$Step$ 4. We have certainty measure for e_8, e_9 and e_{10} as Table 6.

Table 6. Table of the certainty measure for e_8, e_9 and e_{10}.

	c_1	c_2	c_3	c_4	c_5
$d^{e_i}(e_8)$	1	0,5	0	0	1
$d^{e_i}(e_9)$	0	0	1	0	0
$d^{e_i}(e_{10})$	0	0,5	0	1	0

$Step$ 5. Following the steps in Definition 3.4, we can determine decision rules as follows:

1. if (female) and (no smoke no drinking) then (healthy), $(d^{e_1}(e_8) = 1)$,
2. if (male) and (smoke) then (healthy), $(d^{e_2}(e_8) = 0{,}5)$,
3. if (male) and (smoke) then (under stress), $(d^{e_2}(e_{10}) = 0{,}5)$,
4. if (male) and (smoke and drinking) then (drug addict), $(d^{e_3}(e_9) = 1)$,
5. if (male) and (no smoke no drinking) then (healthy), $(d^{e_4}(e_8) = 1)$,
6. if (female) and (smoke) then (under stress), $(d^{e_5}(e_{10}) = 1)$.

As a result of the algorithm, the following rules are defined as final decision rules: , "if c_1 then e_8", "if c_3 then e_9", "if c_4 then e_8" and "if c_5 then e_{10}" These rules express precise pairings that allow precise decisions to be made under certain conditions.

4. Conclusion

This study makes important contributions from both theoretical and practical perspectives. The primary goal of the research is to develop a novel decision algorithm based on objective soft rough sets and to test the effectiveness of this algorithm on an example. The findings show the practical applicability of this algorithm. Accordingly, this research has the potential to pave the way for many new studies on real-life applications.

Ethical statement

The author declares that this document requires no ethical approval or special permission.

Conflict of interest

The authors of the study emphasize that there are no conflicts of interest.

Generative AI statement

The author(s) declare that no Gen AI was used in the creation of this manuscript.

References

[1] Zadeh, L.A., "Fuzzy sets", *Information and Control,* 8(3), 338-353, 1965. https://doi.org/10.1016/S0019-9958(65)90241-X

[2] Atanassov, K., "Intuitionistic fuzzy sets", *Fuzzy Sets and Systems*, 20(1), 87–96, 1986. https://doi.org/10.1016/S0165-0114(86)80034-3

[3] Gau, W.L., Buehrer, D.J., "Vague sets", *IEEE Trans. Syst. Man. Cybern*., 23(2), 610–614, 1993. DOI: 10.1109/21.229476

[4] Pawlak, Z., "Rough sets", *International Journal of Computer & Information Sciences*, 11(5), 341–356, 1982. https://doi.org/10.1007/BF01001956

[5] Molodtsov, D., "Soft set theory – First results", *Computers and Mathematics with Applications*, 37(4-5), 19–31, 1999. https://doi.org/10.1016/S0898-1221(99)00056-5

[6] Maji, P.K., Biswas, R., Roy, A.R., "Soft set theory", *Computers and Mathematics with Applications,* 45(4-5), 555–562, 2003. https://doi.org/10.1016/S0898-1221(03)00016-6

[7] Ali, M.I., Feng, F., Liu, X., Min, W.K., Shabira, M., "On some new operations in soft set theory", *Computers and Mathematics with Applications*, 57(9), 1547-1553, 2009. https://doi.org/10.1016/j.camwa.2008.11.009

[8] Maji, P.K., Roy, A.R., Biswas, R., "An application of soft sets in a decision making problem", *Computers and Mathematics with Applications*, 44(8-9), 1077–1083, 2002. https://doi.org/10.1016/S0898-1221(02)00216-X

[9] Chen, D., Tsang, E.C.C., Yeung, D.S., Wang, X., "The parameterization reduction of soft sets and its applications", *Computers and Mathematics with Applications*, 49(5-6), 757-763, 2005. https://doi.org/10.1016/j.camwa.2004.10.036

[10] Gong, K., Xiao, Z., Zhang, X., "The bijective soft set with its operations", *Computers and Mathematics with Applications*, 60(8), 2270–2278, 2010. https://doi.org/10.1016/j.camwa.2010.08.017

[11] Aktaş, H., " Some algebraic applications of soft sets", *Applied Soft Computing*, 28, 327-331, 2015. https://doi.org/10.1016/j.asoc.2014.11.045

[12] Koyuncu, F., "Bijective soft rings with applications", *Journal of New Results in Science*, 13(1), 47-60, 2024. https://doi.org/10.54187/jnrs.1464556

[13] Gong, K., Wang, P., Peng, Y. "Fault-tolerant enhanced bijective soft set with applications", *Applied Soft Computing*, 54, 431-439, 2017. https://doi.org/10.1016/j.asoc.2016.06.009

[14] Tiwari, V., Jain, P.K., Tandon, P., "A bijective soft set theoretic approach for concept selection in design process", *Journal of Engineering Design*, 28(2), 100-117, 2017. https://doi.org/10.1080/09544828.2016.1274718

[15] Pawlak, Z., Skowron, A., "Rough sets and Boolean reasoning", *Information Sciences*, 177(1), 41–73, 2007. https://doi.org/10.1016/j.ins.2006.06.007

[16] Pawlak, Z., "Rough sets and intelligent data analysis", *Information Sciences*, 147(1-4), 1-12, 2002. https://doi.org/10.1016/S0020-0255(02)00197-4

[17] Pawlak, Z., Skowron, A., "Rudiments of rough sets", *Information Sciences*, 177(1), 3-27, 2007. https://doi.org/10.1016/j.ins.2006.06.003

[18] Polkowski, L., Skowron, A., "Rough mereology: a new paradigm for approximate reasoning", *International Journal of Approximate Reasoning*, 15(4), 333–365, 1997. https://doi.org/10.1016/S0888-613X(96)00072-2

[19] Peters, J.F., Pal, S.K., Cantor, Fuzzy, Near, and Rough Sets in Image Analysis, in: Rough Fuzzy Image Analysis: Foundations and Methodologies, (Eds: Pal, S.K. and Peters, J. F.) CRC Pres, Taylor and Francis Group, Boca Raton, U.S.A, pp. 1.1-1.16., 2010.

[20] Herawan, T., Deris, M.M., "A direct proof of every rough set is a soft set", Third Asia International Conference on Modelling & Simulation, Bali, Indonesia, 2009, pp. 119 -124.

[21] Feng, F., Li, C., Davvaz, B., Ali, M.I., "Soft sets combined with fuzzy sets and rough sets: A tentative approach", *Soft Computing*, 14(9), 899–911, 2010. https://doi.org/10.1007/s00500-009-0465-6

[22] Feng, F., Liu, X., Leoreanu-Fotea, V., Jun, Y.B., "Soft sets and soft rough sets", *Information Sciences*, 181(6), 125–1137, 2011. https://doi.org/10.1016/j.ins.2010.11.004

[23] Pan, W., Zhan, J., "Soft Rough Groups and Corresponding Decision Making", *Italian Journal of Pure and Applied Mathematics*, 38, 158-171, 2017.

[24] Zhan, J., Liu, Q., Herawan, T., "A novel soft rough set: Soft rough hemirings and corresponding multicriteria group decision making", *Applied Soft Computing*, 54, 393-402, 2017. https://doi.org/10.1016/j.asoc.2016.09.012

[25] Wang, Q., Zhan, J., Borzooei, R.A., "A study on soft rough semigroups and corresponding decision making applications", *Open Mathematics*, 15(1), 1400–1413, 2017. https://doi.org/10.1515/math-2017-0119

[26] Bağırmaz, N., *Bijective Soft Rough Sets, in: Unified Perspectives in Mathematics and Geometry* (Ed. İ. Eryılmaz). BIDGE Publications, Ankara, pp. 142-161, 2024.

Middle East Journal of Science

https://dergipark.org.tr/mejs **MEJS**

e-ISSN:2618-6136

Research Article

PREPARATION AND CHARACTERIZATION OF A NEW SILICA GEL - BASED PIRKLE - TYPE CHIRAL STATIONARY PHASE AS A NEW HPLC COLUMN PACKING MATERIAL

***Ramazan ALTINDAĞ*[1] *Murat SUNKUR*[2] *Reşit ÇAKMAK*[3] *Giray TOPAL**[4]

[1] Department of Chemistry, Institute of Science, Dicle University, Diyarbakır, Türkiye
[2] Department of Chemistry, Faculty of Sciences and Arts, Batman University, Batman, 72060, Türkiye
[3]Medical Laboratory Techniques Prog., Vocational School of Health Services, Batman Uni., Batman, Türkiye
[4]Department of Chemistry, Ziya Gökalp Faculty of Education, Dicle University, Diyarbakır, Türkiye
* Corresponding author: gtopal@dicle.edu.tr

Abstract: *In this study, a new silica-based Pirkle-type chiral stationary phase was successfully prepared by using silica gel 60 as a matrix, 3-(chloropropyl)-trimethoxysilane as a spacer arm, and (S)-4-amino-N-(1-cyclohexylethyl)benzamide (II) a chiral selector; and loaded onto the high performance liquid chromatography column by using a mobile phase to prepare a new chiral high performance liquid chromatography column. The chiral selector was synthesized in two steps. In the first step, (S)-N-(1-cyclohexylethyl)-4-nitrobenzamide(I) was obtained, and then the aromatic amine derivative (II) of this compound was obtained with hydrazine hydrate and Pd/C catalyst. The prepared chiral selector (II) was then immobilized on 3-chloropropyl functionalized silica gel (III) prepared by condensation reaction of 3-(chloropropyl)-trimethoxy silane with silica gel 60. In the last step, the new chiral stationary phase derived from silica (IV) was loaded onto a commercial column with the aid of a column-packing apparatus using known methods. The structures of the synthesized chiral selector (II), the new chiral stationary phase (IV), and the characteristic features of the prepared column were investigated by spectroscopic techniques. As a result of the spectroscopic analysis, it was determined that the new chiral stationary phase was prepared successfully.*

Keywords*: Chirality, Chiral stationary phase, Silica-based chiral high performance liquid chromatography column.*

Received: April 18, 2025 *Accepted: June 4, 2025*

1. Introduction

Chirality refers to a situation in which mirror images of compounds are not superimposable [1]. These compounds usually consist of at least two enantiomers that can have different effects in biological systems [2-4]. Nowadays, chiral high performance liquid chromatography (HPLC) columns containing specially designed chiral stationary phases (CSPs) are used to make enantiomeric resolution of racemic mixtures, which are equal mixtures of two enantiomers [5,6]. In the preparation of chiral HPLC columns, different matrices are used as column packing materials. For example, silica gel is one of them. The surface of silica gel is modified with chiral selectors having chiral groups to create a chiral environment. In this way, the behavior of enantiomers that encounter a chiral environment towards the chiral stationary phase differs. As a result of this differentiation, racemic mixtures can be divided into their enantiomers [7,8].

On the other hand, polymer-based stationary phases are among the important stationary phases used in the preparation of chiral HPLC columns. These stationary phases are usually made of natural

or synthetic polymers and contain suitable chiral groups that can separate enantiomers [9]. Apart from these, other CSPs can be prepared from macrocyclic glycopeptide antibiotics, protein-based structures, ligand exchange-based structures, and polysaccharide-based structures [10]. Chiral ligands are used to enable different interactions between enantiomers by binding to the surface of stationary phases. Generally, these stationary phases are cyclic structures such as crown ethers and cyclodextrins containing chiral cavities. CSPs based on ion exchange are structures in which ion exchange is carried out under the coordination of a dominant metal ion and operate on the basis of ion exchange [11,12]. In recent years, a new stationary phase has been added to these stationary phases. Previously known as Brush-type CSP and later called Pirkle-type stationary phases, these new generation stationary phases are formed by attacking and permanently binding a small chiral organic molecule attached to a support arm such as a 3,5-dinitro benzoyl group to the silica surface, and the chiral groups on the silica surface have a combed brush appearance [13,14]. The enantiomer pair to be separated is physically attached to these surfaces through pi bond interactions, hydrogen bond interactions, ion-dipole interactions. The chiral groups used can be acidic or basic amino acids, as well as chiral amino alcohol, amide alcohol, ester or chiral carboxylic acid derivatives [15].

Pirkle-type CSPs are mostly silica-based materials containing chiral separating selectors [16]. These CSPs were first developed by W. H. Pirkle and colleagues in 1967 and were designed based on the idea that molecules containing chiral groups could be interacted with non-chiral connecting arms or surfaces to form a series of new ligands containing chiral groups [17,18]. These systems enable the separation of enantiomers by using different interactions of optical equivalents. Pirkle ligands are chiral organic molecules usually derived from natural or synthesized compounds [19]. These ligands can provide selective interactions based on the different physicochemical properties of the enantiomers, presenting a specific stereo chemical structure. For instance, some of Pirkle ligands may contain β-amino acid derivatives and other similar chiral structures [20]. In these CSPs, chiral molecules are attached to the silica gel by ionic or covalent bonds. In general, we can talk about three types of Pirkle-type CSPs. These are π-acidic CSPs, π-basic CSPs, and π-acidic-basic CSPs [21]. The first stationary phase of ionic bonding developed by Pirkle is (*R*)-3,5-dinitrobenzoyl phenyl glycine. The most commonly used spacer arm is 3,5-dinitrophenyl group, which is known for its reactions with 3,5-dinitrobenzoyl chloride on chiral selectors including amino acids, amino alcohols, and amines. The first CSP designed based on ionic bonding was designed by Pirkle and contained 3,5-dinitro benzoyl groups a spacer arm [22]. These CSPs contain phenyl or alkyl-substituted phenyl groups. Pirkle-type CSPs are quite stable and have good chiral selectivity. This type of CSP is frequently used for the separation of racemic drugs and amino acid analysis [23]. Firstly, these CSPs achieved chiral separation of racemic compounds. However, in some cases, racemic compounds may need to be previously derivatized with achiral reagents. Experimental studies have shown that this type of CSPs is more effective than other CSPs in chiral separation. In such CSPs, chiral separations are usually performed in normal phase mode. However, with the development of new and more stable phases, the reverse phase mode has become more popular [24-28].

In the current study, a new Pirkle-type CSP was obtained as a new silica gel based column-packing material and the prepared CSP was loaded onto the column to prepare a new chiral HPLC column. In this context, a chiral selector was synthesized and elucidated by spectroscopic techniques including ^{1}NMR, ^{13}C NMR and FTIR. The molecular structure of newly prepared CSP was characterized by FT-IR, elemental analysis and BET measurement, respectively.

2. Materials and Methods

2.1. Chemistry and Analysis

All chemicals (4-nitrobenzoylchloride, (*S*)-(+)-1-cyclohexylethylamine, hydrazine monohydrate (H_2N-NH_2.H_2O), palladium on carbon (Pd/C), tetrahydrofuran, toluene, chloroform, triethylamine, silica gel (Lichrospher Si 60, 5 µm, 60 Å) and 3-chloropropyltrimethoxy silane) used in the preparation of the chiral ligand and the targeted CSP were commercially obtained from Sigma, Merck or Fluka. These chemicals were used without any further purification. Deionized water (Millipore Milli-Q water system) was used in the preparation of all aqueous solutions. Melting points of the targeted compounds were determined by using a Barnstead IA9100 electrothermal digital melting points apparatus. The structures of the synthesized compounds were determined by FT-IR (PerkinElmer Spectrum 100 FT-IR spectrophotometer), ^{1}H (400 MHz) and ^{13}C (100 MHz) NMR spectra (Bruker DPX-400 High Performance Digital FT-NMR spectrometer), and elemental analysis (Thermo Scientific FLASH 2000 instrument). Empty HPLC column was obtained from Quality System Merieux Nutrisciences Company (Istanbul, Turkey). The synthesized chiral stationary phase was packed into the empty HPLC columns using an easypack analytical column packing system (Compressor model DA7001). Specific surface area analysis was made using single-point BET measurements on a Micromeritics Tristar II Plus BET analyzer.

2.2. Synthesis of (*S*)-*N*-(1-cyclohexylethyl)-4-nitrobenzamide (I)

A solution of *p*-nitrobenzoyl chloride (0.0314 mmol) and triethylamine (4.5 mL) in 100 mL of tetrahydrofuran was vigorously stirred at room temperature for 30 min. Then, (*S*)-(+)-1-cyclohexylethylamine (0.0314 mol) in 100 mL of tetrahydrofuran was added dropwise to this solution, and then the obtained reaction mixture was stirred at room temperature for 24 h. After completion of the reaction, the precipitated triethylammonium chloride was removed by vacuum filtration. The resulting filtration was concentrated by rotary evaporation to remove the solvent. The crude product was recrystallized from a 3:2 ethanol/methanol mixture. The product, obtained as off-white needle-like crystals, was collected by vacuum filtration and washed with diethyl ether or petroleum ether (40–60 °C). The final product was dried in air at room temperature.

2.2.1 (*S*)-*N*-(1-cyclohexylethyl)-4-nitrobenzamide

Yield: 6.93 g (79%), melting point: 199–200 °C. FT-IR (cm^{-1}): 3290, 3079 (Aromatic C–H stretching), 2961, 2849 (Aliphatic C–H stretching), 1636 (Amide C=O stretching), 1598 (NO_2 asymmetric stretching), 1546–1442 (C–C stretching, aromatic benzene ring), 1342 (C–H bending vibrations), 1106–1188 (C–N and aromatic C–O stretching). ^{1}H NMR (δ, ppm, $CDCl_3$): 1.23–1.82 (m, 14H, aliphatic H), 4.05–4.10 (m, 1H, CH), 6.14 (d, 1H, NH), 7.92 (d, 2H, Ar–H, J = 2.0 Hz), 8.27 (d, 2H, Ar–H, J = 2.0 Hz). ^{13}C NMR (δ, ppm, $CDCl_3$): 17.92, 26.13, 29.18, 43.15, 50.49, 123.76, 128.06, 140.76, 149.43, 164.86.

2.3. Synthesis of (*S*)-4-amino-*N*-(1-cyclohexylethyl)benzamide (II)

To a 500 mL two-necked, round-bottom flask equipped with a reflux condenser, 5.56 g of (*S*)-*N*-(1-cyclohexylethyl)-4-nitrobenzamide was added along with 200 mL of absolute ethanol. The mixture was stirred using a magnetic stirrer under gentle heating until complete dissolution was achieved. Then, 0.5 g of palladium on carbon (Pd/C) was added to this solution, and the reaction temperature was increased to 65 °C. After stirring for 30 min, 100 mL of hydrazine hydrate, previously placed in a 250 mL dropping funnel, was added dropwise over 30 min. The reaction mixture was then refluxed under continuous stirring for 7 h. After completion of the reaction, the

mixture was filtered many times by filtration to remove the Pd/C catalyst until a clear and light-colored filtrate was obtained. The filtrate was transferred to a rotary evaporator, and the solvent was removed under reduced pressure. The solid residue was crystallized from an ethanol/hexane mixture. The resulting product is formed as shiny white, fluffy crystals. The crystals were collected by vacuum filtration and dried in a desiccator.

2.3.1 (*S*)-4-amino-*N*-(1-cyclohexylethyl)benzamide (II)

Yield: 4.56 g (92%). melting point: 180–182 °C. FT-IR (cm^{-1}): 3316 (N–H stretching, doublet), 3200 (Aromatic C–H stretching), 2919, 2849 (Aliphatic C–H stretching), 1624 (Amide C=O), 1538–1446 (C–C stretching, aromatic ring), 1344 (C–H bending), 1283–1273 (Aromatic substitutions). ^{1}H NMR (δ, ppm, $CDCl_3$): 1.10–1.84 (m, 16H, aliphatic), 4.08–4.13 (m, 1H, CH), 5.97 (d, 1H, NH), 7.93 (d, 2H, Ar–H, J = 2.1 Hz), 8.30 (d, 2H, Ar–H, J = 2.1 Hz). ^{13}C NMR (δ, ppm, $CDCl_3$): 18.01, 26.23, 29.17, 43.21, 50.42, 123.82, 128.05, 140.75, 149.49, 164.81.

2.4. Preparation of 3-Chloropropyl Functionalized Silica Gel (III)

4 g of silica gel and 2.5 g of 3-chloropropyltrimethoxysilane were added to a 100 mL single neck round bottom flask. Then, 30 mL of toluene was added to this mixture and the reaction mixture was stirred under reflux for 4 days. After the reaction was completed, the mixture was filtered through standard filter paper. The solid was wrapped in double filter paper and placed in the Soxhlet apparatus. The solid was extracted with 150 mL of chloroform overnight. After the extraction process, the product was dried in a desiccator. At the end of the reaction, 5.5 g of 3-chloropropyl functionalized silica gel was obtained.

2.5. Preparation of the Novel CSP (IV)

5.5 g of 3-chloropropyl functionalized silica gel (III) and 2.9 g of compound II dissolved in 40 mL of toluene were added to a 100 mL single neck round bottom flask. The reaction mixture was then stirred under reflux in an oil bath at 130 °C for 6 days. Next, the reaction mixture cooled to room temperature and filtered. The filtrate was washed with methanol to remove unreacted amine. The solid product remaining on the filter paper was then placed in a Soxhlet apparatus and washed with chloroform for 3 days. The resulting yellowish material (CSP) was dried in a desiccator for 7 days. At the end of the reaction, a total of 7 g of new CSP was obtained.

2.6. Preparation of Chiral HPLC Column

Firstly, 3.5 g of the freshly prepared CSP was suspended in 30 mL of methanol. Then, the suspension was loaded onto the column with the help of a column packing apparatus using a 300 mL of methanol: isopropanol (1:1) mixture as the mobile phase. The column filling process was carried out entirely in the column-packing apparatus and at room temperature, and the maximum filling pressure was 500 bar. The flow rate was adjusted by filling the column with the 300 mL suspension for 2 h. Initially, a greenish liquid came from the column during loading. Over time, the color lightened and became clear. Several properties of the newly prepared column are given in Table 1.

Table 1. Properties of the newly prepared chiral HPLC column

Limit Pressure	**500 bar**
[a]Max. flow rate for 100% methanol	2.5 mL/min (250 bar)
[a]Max. flow rate for methanol/isopropanol:50/50	4.5 mL/min (450 bar)
Packing Time	2 h
[b]Particle Size	5 µm
[b]Pore Size	60 Å
Matrix active group	amide, cycloalkyl, aromatic amine
Column dimensions	250 x 4.6 mm
[c]Total pore volume	0.20953 cm^3/g
[c]Surface area	238.1289 m^2/g
[c]Micropore volume	0.04782 cm^3/g
[c]Mesopore volume	0.16171 cm^3/g
[c]Average pore diameter	nm
[d]Extent of labelling	3.73% carbon loading

[a]Max. flow rate was determined at the maximum operation pressure (500 bar) at 25°C.

[b]Physical properties of commercially available silica (unmodified, blank silica) (Sigma-Aldrich).

[c]Based on the BET analysis.

[d]Based on the elemental analysis.

On the other hand, the elemental analysis results of blank silica and silica gel-based new CSP are given in Table 2.

Table 2. The elemental analysis results of blank silica and new CSP

Elemental analysis results (%)	**C**	**H**	**N**
Blank Silica	0	0.04	0
Average	3.73	0.56	0.47

3. Results and Discussion

3.1. Synthesis and Characterization

HPLC separation is among the popular research areas. In recent years, significant efforts have been made to prepare new and efficient HPLC columns. For this purpose, various HPLC columns have been prepared and tested so far using different novel CSPs for various purposes, including enantiomeric resolution or molecular separation [1,7,17,27,29]. In this research, a new Pirkle-type CSP (IV), a new silica gel-based column packing material, was prepared by the condensation reaction of 3-chloropropylfunctionalized silica gel (III) with the chiral selector, and then the prepared novel CSP was loaded onto the HPLC column to obtain a novel chiral HPLC column. To prepare the new CSP, silica gel 60 as a matrix, 3-(chloropropyl)-trimethoxysilane as a spacer arm, and (*S*)-4-amino-*N*-(1-cyclohexylethyl)benzamide (II) as a chiral selector were used. The chiral selector was successfully synthesized in two steps using (*S*)-(+)-1-cyclohexylethylamine as the starting material. The targeted chiral selector and novel CSP were successfully characterized by various spectroscopic techniques.

The synthesis route to obtain the chiral selector (II) and the newly synthesized CSP (IV) is described in Scheme 1.

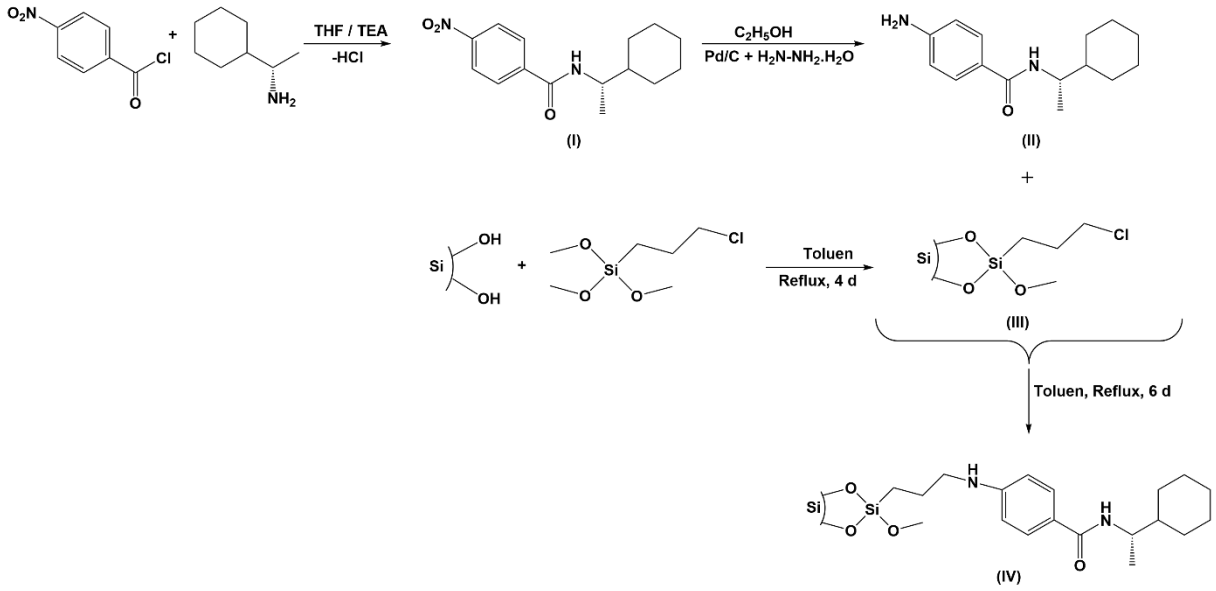

Scheme 1. Synthetic route to the preparation of the chiral selector (II) and the novel SP (IV)

When examining the IR spectra of compounds used in the synthesis of the chiral selector, while no peaks were observed in the IR spectrum of compound I in the 3300-3500 cm^{-1} region, the characteristic N-H stretching vibrations of primary amines were observed at 3316 cm^{-1} and 3220 cm^{-1} in the IR spectrum of compound II. The 1598 cm^{-1} stretching vibration peak belonging to the nitro group seen in the IR spectrum of compound I disappeared in compound II. Moreover, the observation of amine N-H in-plane bending vibrations at 1602 cm^{-1} in the IR spectrum of compound II indicates that reduction has occurred. In the IR spectrum of compound III, only bands belonging to C-H stretching vibrations (aliphatic C-H stretching is more dominant) are visible around 2971 $cm^{-1,}$ while new peaks were observed at 1610 cm^{-1}, 1506 cm^{-1} and 1448 cm^{-1} in the IR spectrum of compound IV. The new peaks were evaluated as C=O stretching of amide carbonyl, C-H bending of alkyl groups and aromatic ring C=C stretching vibrations, respectively. No change was observed in the basic peaks in the fingerprint region. This is evidence that the amine group was replaced by the chlorine atom in the chlorinated silica (III) as a result of a nucleophilic reaction and that compound II was bound to the silica surface. The fact that the comparative IR spectra of compound III and compound IV do not overlap is another proof that binding has occurred. In the NMR spectra of the chiral selector, the increase in the number of H atoms in the ^{1}H NMR spectrum of compound II obtained as a result of the reduction reaction is another evidence that the NO_2 group has transformed into the NH_2 group. In ^{13}C NMR spectra of the chiral selector (II), the signal at 164 ppm belongs to the carbonyl group, and the signals between 18 and 50 ppm belong to aliphatic carbons. In addition, the peak at 5.97 ppm in the ^{1}H NMR spectrum belongs to the amide proton in the structure. On the other hand, the specific surface area and the total pore volume of the new CSP measured by using BET analysis were calculated to be 238.1289 m^2g^{-1} and 0.20953 $cm^3\ g^{-1}$, respectively, which are greatly reduced compared to those of the blank silica (737 m^2g^{-1} and 0.75 cm^3g^{-1})[7], as seen in Table 1. In addition, elemental analysis of blank silica and new CSP was carried out to measure the elemental composition. As shown in Table 2, the carbon (C), hydrogen (H) and nitrogen (N) contents of the new CSP were calculated as 3.73 0.56 0.47, respectively. FTIR, BET measurement and the elemental analysis results of novel silica gel-based CSP

demonstrate the successful preparation of the targeted column packing material. FT-IR, ^{1}H, and ^{13}CNMR spectra of chiral selector (I and II), 3-chloropropyl functionalized silica gel (III) and novel CSP (IV) are given in the Supplementary Materials, Figures S1−S9.

4. Conclusion

In this study, a new Pirkle-type CSP (IV) as a new silica gel-based column packing material was easily obtained by the reaction of a chiral selector (II) with 3-chloropropyl functionalized silica gel (III). Then, the prepared new CSP (IV) was loaded onto the HPLC column using a mobile phase. For this study, the chiral selector was synthesized in two steps and in high purity, and then elucidated by spectroscopic techniques (^{1}NMR, ^{13}C NMR and FTIR). The structure of the targeted novel CSP was characterized by FT-IR, elemental analysis and BET measurement. At the end of the study, we can say that the newly prepared chiral HPLC column has the potential to be used in enantiomeric resolution of racemic compounds or molecular separation studies of bioactive or important molecules.

Ethical statement

The author declares that this document does not require ethics committee approval or any special permission. This study does not cause any harm to the environment.

Acknowledgment

The authors would like to thank Dicle University Scientific Research Projects Coordination Unit for the financial support provided to them through project number **FBE.21.008**.

Conflict of interest:

The article's authors declare that there is no conflict of interest between them.

Authors' Contributions:

R. A: Methodology, Validation, Formal analysis, Investigation (%35)

M. S: Validation, Formal analysis, Methodology, Investigation, Writing - original draft preparation (%25)

R. Ç: Validation, Formal analysis, Writing - original draft preparation (%10)

G. T: Conceptualization, Methodology, Validation, Investigation, Resources, Writing – review & editing, Supervision, Project administration, Funding acquisition (%30)

Generative AI statement

The author(s) declare that no Gen AI was used in the creation of this manuscript.

References

[1] Yılmaz, H., Topal, G., Çakmak, R., Hosgoren, H., Resolution of (±)-β-methylphenylethylamine by a novel chiral stationary phase for Pirkle-type column chromatography. *Chirality*: The Pharmacological, Biological, and Chemical Consequences of Molecular Asymmetry, 22(2), 252-257, 2010.

[2] Basaran, E., Sogukomerogullari, H.G., Çakmak, R., Akkoc, S., Taskin-Tok, T., Köse, A., "Novel chiral Schiff base Palladium (II), Nickel (II), Copper (II) and Iron (II) complexes: Synthesis, characterization, anticancer activity and molecular docking studies", *Bioorganic Chemistry*, 129, 106176, 2022. https://doi.org/10.1016/j.bioorg.2022.106176.

[3] Başaran, E., Karaküçük-Iyidoğan, A., Schols, D., Oruç-Emre, E.E., "Synthesis of novel chiral sulfonamide-bearing 1, 2, 4-triazole-3-thione analogs derived from D-and L-phenylalanine esters as potential anti-influenza agents", *Chirality*, 28(6), 495-513, 2016. https://doi.org/10.1002/chir.22607.

[4] Karaküçük-İyidoğan, A., Başaran, E., Tatar-Yılmaz, G., Oruç-Emre, E.E. "Development of new chiral 1, 2, 4-triazole-3-thiones and 1, 3, 4-thiadiazoles with promising in vivo anticonvulsant activity targeting GABAergic system and voltage-gated sodium channels (VGSCs)", *Bioorganic Chemistry*, 151, 107662. 2024, https://doi.org/10.1016/j.bioorg.2024.107662.

[5] Okamoto, Y., Ikai, T., "Chiral HPLC for efficient resolution of enantiomers", *Chemical Society Reviews*, 37(12), 2593-2608, 2008. https://doi.org/10.1039/B808881K.

[6] Lomenova, A., Hroboňová, K., "Comparison of HPLC separation of phenylalanine enantiomers on different types of chiral stationary phases", *Food Analytical Methods*, 11, 3314-3323, 2018. https://doi.org/10.1007/s12161-018-1308-9.

[7] Aral, H., Çelik, K.S., Altındağ, R., Aral, T., "Synthesis, characterization, and application of a novel multifunctional stationary phase for hydrophilic interaction/reversed phase mixed-mode chromatography", *Talanta*, 174, 703-714, 2017. https://doi.org/10.1016/j.talanta.2017.07.014.

[8] Lorenz, H., Seidel-Morgenstern, A., "Processes to separate enantiomers", *Angewandte Chemie International Edition*, 53(5), 1218-1250, 2014, https://doi.org/10.1002/anie.201302823.

[9] Wang, Y., Chen, H., Xiao, Y., Ng, C.-H., Oh, T.S., Tan, T.T.Y., Ng, S.C., "Preparation of cyclodextrin chiral stationary phases by organic soluble catalytic'click'chemistry", *Nature protocols*, 6(7), 935-942, 2011. https://doi.org/10.1038/nprot.2011.340.

[10] Ali, I., Kumerer, K., Aboul-Enein, H.Y., "Mechanistic principles in chiral separations using liquid chromatography and capillary electrophoresis", *Chromatographi*a, 63, 295-307, 2006. https://doi.org/10.1365/s10337-006-0762-5.

[11] Ward, T.J., "Chiral separations", *Analytical Chemistry*, 72(18), 4521-4528, 2000. https://doi.org/10.1021/ac000841o.

[12] Kuhn, R., Stoecklin, F., Erni, F., "Chiral separations by host-guest complexation with cyclodextrin and crown ether in capillary zone electrophoresis", *Chromatographia*, 33, 32-36, 1992. https://doi.org/10.1007/BF02276847.

[13] Wolf, C., Pirkle, W.H., "Synthesis and evaluation of a copolymeric chiral stationary phase", *Journal of Chromatography A*, 799(1-2), 177-184, 1998. https://doi.org/10.1016/S0021-9673(97)01063-7.

[14] Pirkle, W.H., Burke Iii, J.A., "Chiral stationary phase designed for β-blockers", *Journal of Chromatography A*, 557, 173-185, 1991. https://doi.org/10.1016/S0021-9673(01)87131-4.

[15] Pirkle, W.H., Sikkenga, D.L., "Resolution of optical isomers by liquid chromatography", *Journal of Chromatography A*, 123(2), 400-404, 1976. https://doi.org/10.1016/S0021-9673(00)82210-4.

[16] Vedovello, P., Costa, J.A.S., Fernandes, C., Tiritan, M. E., Paranhos, C.M., "Evaluation of chiral separation by Pirkle-type chiral selector based mixed matrix membranes", *Separation and Purification Technology*, 289, 120722, 2022. https://doi.org/10.1016/j.seppur.2022.120722.

[17] Çakmak, R., Ercan, S., Sunkur, M., Yilmaz, H., Topal, G., "Design, preparation and application of a Pirkle-type chiral stationary phase for enantioseparation of some racemic organic acids and

molecular dynamics studies", *Organic Communications*, 10(3), 216–227, 2017. http://doi.org/10.25135/acg.oc.25.17.07.0.

[18] Pirkle, W.H., Pochapsky, T.C., "Considerations of chiral recognition relevant to the liquid chromatography separation of enantiomers", *Chemical Reviews*, 89(2), 347-362, 1989. https://doi.org/10.1021/cr00092a006.

[19] Zhao, Y., Zhu, X., Jiang, W., Liu, H., Wang, J., Sun, B., "Natural and artificial chiral-based systems for separation applications", *Critical Reviews in Analytical Chemistry*, 53(1), 27-45, 2023. https://doi.org/10.1080/10408347.2021.1932408.

[20] Peter, A., Lazar, L., Fülöp, F., Armstrong, D.W., "High-performance liquid chromatographic enantioseparation of β-amino acids," *Journal of Chromatography A*, 926(2), 229-238, 2001. https://doi.org/10.1016/S0021-9673(01)01078-0.

[21] Vargas-Caporali, J., Juaristi, E., "Fundamental Developments of Chiral Phase Chromatography in Connection with Enantioselective Synthesis of β-Amino Acids", *Israel Journal of Chemistry,* 57(9), 896-912, 2017. https://doi.org/10.1002/ijch.201700011.

[22] Simeonov, S.P., Simeonov, A.P., Todorov, A.R., Kurteva, V.B., "Enantioresolution of a series of chiral benzyl alcohols by HPLC on a dinitrobenzoylphenylglycine Stationary Phase after Achiral Pre-Column Derivatization", *American Journal of Analytical Chemistry*, 1(1), 1-13, 2010. https://doi.org/10.4236/ajac.2010.11001.

[23] Mane, S., "Racemic drug resolution: a comprehensive guide", *Analytical Methods*, 8(42), 7567-7586, 2016. https://doi.org/10.1039/C6AY02015A.

[24] Aral, H., Çelik, K.S., Aral, T., Topal, G., "Preparation of a novel ionic hybrid stationary phase by non-covalent functionalization of single-walled carbon nanotubes with amino-derivatized silica gel for fast HPLC separation of aromatic compounds", *Talanta*, 149, 21-29, 2016. https://doi.org/10.1016/j.talanta.2015.11.029.

[25] Ilisz, I., Aranyi, A., Péter, A., "Chiral derivatizations applied for the separation of unusual amino acid enantiomers by liquid chromatography and related techniques", *Journal of Chromatography A*, 1296, 119-139, 2013. https://doi.org/10.1016/j.chroma.2013.03.034.

[26] Colin, H., Guiochon, G., "Introduction to reversed-phase high-performance liquid chromatography*", Journal of Chromatography A*, 141(3), 289-312, 1977. https://doi.org/10.1016/S0021-9673(00)93537-4.

[27] Erdoğan, Ö., Topal, G., Çakmak, R., Sünkür, M., Canpolat, M., "The preparation of a new protein based HPLC column packing material and enantiomeric resolution of some pharmaceutical related compounds via this column", *Middle East Journal of Science*, 2(1), 77-92, 2016. https://doi.org/10.23884/mejs/2016.2.1.07.

[28] Engelhardt, H., Jungheim, M., "Comparison and characterization of reversed phases", *Chromatographia*, 29, 59-68, 1990. https://doi.org/10.1007/BF02261141.

[29] Kalili, K. M., de Villiers, A., "Recent developments in the HPLC separation of phenolic compounds", *Journal of Separation Science*, 34(8), 854-876, 2011. https://doi.org/10.1002/jssc.201000811.

Middle East Journal of Science

https://dergipark.org.tr/mejs **MEJS**

e-ISSN:2618-6136

Research Article

ELECTROCOAGULATION USING STAINLESS STEEL ANODES: THE REMOVAL OF NITRATE FROM AGRO-BASED GROUNDWATER

Benan YAZICI KARABULUT*[1]

[1]Harran University, Engineering Faculty, Department of Environmental Engineering, Sanliurfa, Türkiye

* Corresponding author: benanyazici@harran.edu.tr

Abstract: *This study covers groundwater treatment for nitrate (NO_3^-) removal by the electrocoagulation (EC) method for March (pre-irrigation) and October (post-irrigation) of 2023 for ten observation points in an arid and semi-arid region. Stainless steel (SS) plate electrodes were used in the process, and energy consumption and cost assessment were also carried out. The study area is covered with fertile agricultural lands, and the people of the region make their living from agricultural activities. Therefore, the actual groundwater samples used in the study contain high concentrations of NO_3^-. The effectiveness of the main operational parameters, such as initial pH, electrical conductivity, and current density, was analyzed. It was observed that nitrate removal at the highest electrical conductivity value (2239 µS/cm) had the lowest energy consumption value (0.81 kWh/m^3). The SS values measured at the end of the EC process were < 0.4. In other words, the SS value passing into the water is very low and has no adverse effect on human health. In this study specific to the Harran Plain, a cost of $1.06 per m^3 was calculated for nitrate removal using current electricity costs.*

Keywords: *Electrocoagulation, energy consumption, nitrate removal, stainless steel.*

Received: January 22, 2025 *Accepted: May 12, 2025*

1. Introduction

The electrocoagulation (EC) process utilizing stainless steel electrodes has emerged as a promising method for the treatment of nitrate-contaminated groundwater. This technique leverages the electrochemical reactions that occur when an electric current is applied to electrodes submerged in water, leading to the destabilization and aggregation of pollutants, including nitrates (NO_3^-). The efficiency of this process is influenced by several factors, including electrode material, current density, pH, and operational parameters. Electrocoagulation operates by generating metal hydroxides through the dissolution of the electrodes, which then interact with dissolved contaminants. Stainless steel (SS) electrodes are particularly advantageous due to their durability and resistance to corrosion, which can enhance the longevity of the treatment system [1,2]. Studies have shown that stainless steel electrodes can achieve significant nitrate removal efficiencies, often exceeding 90% under optimal conditions [3,4]. For instance, research indicates that the electrocoagulation process can effectively reduce nitrate levels in groundwater, with operational parameters such as current density and electrode spacing playing critical roles in optimizing removal rates [5,6]. The mechanism of nitrate removal via EC involves both adsorption and electrochemical reduction. The hydroxide ions generated at the cathode facilitate the

formation of flocs that capture nitrate ions, while the applied electric current promotes the reduction of nitrates to nitrogen gas or ammonia [7,8]. This dual mechanism not only enhances the removal efficiency but also allows for the potential recovery of valuable by-products, such as ammonia, which can be utilized in various applications [9,10]. Various traditional techniques such as adsorption, ion exchange, reverse osmosis, electrochemical, chemical, and biological methods have been developed to remove nitrate from water [11,12]. Furthermore, the integration of electrocoagulation with other treatment methods, such as adsorption, has been explored to further enhance nitrate removal efficiencies [13].

The EC process has emerged as a promising technology for the removal of nitrates from groundwater, particularly when utilizing SS electrodes. This method leverages the electrochemical generation of coagulants, primarily metal hydroxides, which destabilize and aggregate contaminants, facilitating their removal from aqueous solutions. The efficiency of EC in treating nitrate-laden water is influenced by various operational parameters, including electrode material, current density, pH, and contact time, which collectively dictate the effectiveness of the process. Stainless steel electrodes have garnered attention due to their durability and effectiveness in electrocoagulation applications. Studies have shown that stainless steel electrodes can effectively generate the necessary coagulants while exhibiting resistance to corrosion, which is a significant advantage over more traditional materials like aluminum or iron [3,14]. The use of stainless steel also minimizes the risk of introducing additional contaminants into the treated water, which is a critical consideration in groundwater remediation efforts [15]. The operational parameters of the electrocoagulation process are crucial for optimizing nitrate removal. Research indicates that the optimal contact time for effective nitrate removal typically ranges from 15 to 60 minutes, with a peak efficiency observed at around 30 minutes [16]. Additionally, the current density applied during the electrocoagulation process plays a pivotal role in determining the rate of nitrate removal. Higher current densities have been associated with increased production of hydroxides, thereby enhancing the coagulation process [1]. However, it is essential to balance the current density with energy consumption, as excessively high values may lead to diminishing returns in nitrate removal efficiency and increased operational costs [8]. The pH of the solution is another critical factor influencing the electrocoagulation process. The removal efficiency of nitrates tends to be higher at acidic pH levels, where the presence of hydrogen ions can facilitate the reduction of nitrate ions [17]. In addition to the operational parameters, the configuration of the electrocoagulation system, including the distance between electrodes and the arrangement of the electrodes, can significantly impact the treatment efficiency. Studies have shown that maintaining an optimal gap between stainless steel electrodes can enhance the electric field strength, thereby improving the coagulation process [14]. Furthermore, the design of the electrocoagulation reactor, such as the use of batch versus continuous flow systems, can also influence the overall effectiveness of nitrate removal [18]. The integration of electrocoagulation with other treatment methods can further enhance nitrate removal efficiencies. For instance, coupling electrocoagulation with activated carbon filtration has been shown to improve the overall quality of treated water by not only removing nitrates but also adsorbing residual contaminants [19]. This two-step approach allows for a more comprehensive treatment strategy, addressing multiple contaminants simultaneously and improving the sustainability of groundwater treatment practices. The environmental implications of nitrate contamination in groundwater are significant, as elevated nitrate levels can lead to adverse health effects and ecological disturbances. The electrocoagulation process offers a viable solution to mitigate these risks by providing an efficient and environmentally friendly method for nitrate removal [20,21].

The central and southern parts of the Harran plain basin have good groundwater potential. While very good groundwater potential is found regionally towards the north, other parts of the basin are generally at moderate levels. In some regions, groundwater potential is almost non-existent and therefore, it is characterized as poor. Unfortunately, the fact that agro-based nitrate pollution is

encountered in the waters in the Harran Plain region, where groundwater potential is characterized as good, negatively affects the quality of the waters here. The point of this study was to look at the quality of groundwater in the Harran plain, which is mostly used for farming, and see how well the electrocoagulation process worked at getting rid of nitrates in water samples that were taken from severely nitrate-contaminated groundwater before and after irrigation. This strategy is anticipated to enhance its applicability in other places exhibiting similar features to the study area.

2. Materials and Methods

2.1. Description of study area

The Harran Plain is situated in the Sanliurfa-Harran irrigation area. The plain, about 30 km in breadth and 50 km in length, is situated in the Southeastern Anatolia Region (36° 43' - 37° 10' N and 38° 47' - 39° 10' E). The region, the largest component of the GAP Project, encompasses 141,855 hectares of irrigable land, a drainage area of 3,700 square kilometers, and the plain area of 1,500 square kilometers. In the area characterized by a semi-arid climate, precipitation is virtually absent from June to September. The long-term annual precipitation is 284.2 mm, the temperature is 18 °C, and the evaporation is 1848 mm. The overall gradient orientation is from north to south, ranging from 0% to 2%. The terrain gradient is nearly level in the vicinity of Harran and Akçakale districts. The level terrain contributes to issues related to agricultural water runoff and drainage complications. The soils are clay-rich, with pH values ranging from 7.5 to 8.0. The minimum permeability is 0.22 m/day, while the maximum permeability is 3.51 m/day. Seventy-seven percent of the land has soil profiles above 150 cm in depth [22].

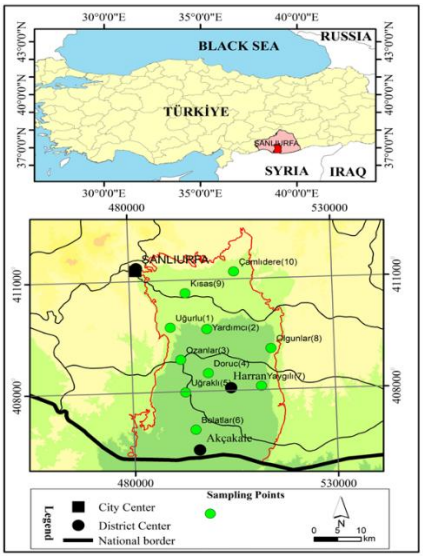

Figure 1. The map of the study area. *Sampling Points: Uğurlu (1), Yardımcı (2), Ozanlar (3), Doruç (4), Uğraklı (5), Bolatlar (6), Yaygılı (7), Olgunlar (8), Kısas (9) and Çamlıdere (10).

2.2. Sample collection

The primary concern to Harran Plain groundwater is the pollutant characteristics transported by agricultural return irrigation flows. Sampling was conducted in the Harran Plain over two intervals: pre-irrigation in March 2023 and post-irrigation in October 2023. Initially, samples were collected from 10 wells at specified ratios (Figure 1). Harran Plain contains two types of aquifers: shallow and deep. The selected ten sampling locations illustrate the shallow aquifer of the plain [23]. Groundwater sampling

was conducted in the shallow aquifer. Water samples collected from the sampling locations were processed in compliance with the laboratory conditions established according to the norms at Harran University. In-situ and laboratory analyses were performed on these samples. This study conducted nitrate analyses in October and March utilizing the ICP-MS technique in accordance with Standard Methods. During sampling, parameters such as groundwater level, temperature, conductivity, pH were measured in-situ. The groundwater level of the wells was determined by a well meter. pH measurements were made with a WTW Multi 340i device and conductivity and temperature measurements were made with a Hach HQ40D device.

2.3. Design of Electrocoagulation Units for Nitrate Removal

Glass with dimensions of 100 x 100 x 250 mm served as the EC reactor in the experimental studies. The study used seven plate electrodes measuring 96 × 180 × 1.5 mm (purity P 99.5%). A batch reactor carried out the EC process to remove nitrate from groundwater using SS electrodes. Figure 2 illustrates the process, while Table 1 displays its characteristics. The minimum distance between the electrodes with monopolar connection was determined to be 10 mm. The Rigol DP832A Programmable 3-Channel DC Power Supply provided current and voltage control. Mixing was carried out with the IKA RH Basic 2 brand magnetic stirrer.

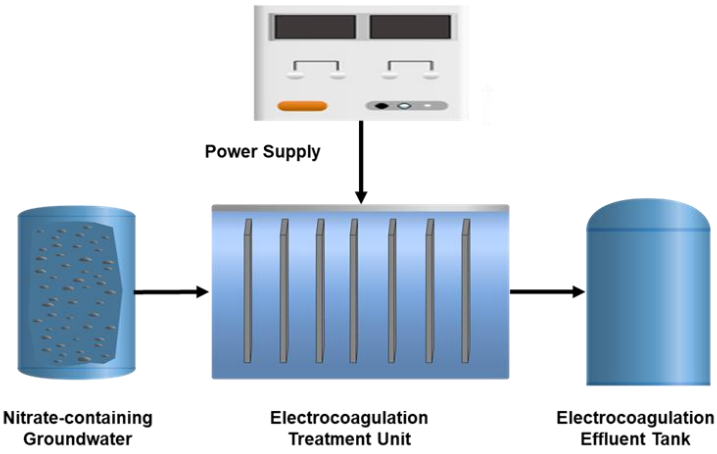

Figure 2. Experimental setup used in the current batch EC process studies.

The pH, conductivity, and temperature of the samples taken at regular intervals during the reactor operation period were measured according to standard methods for examination of water and wastewater. The experiments were carried out in three replicates.

3. Results and Discussion

The Harran Plain saw a rapid level rise from the start of the irrigation period in 1995 until 1998. A rise of about 25 m can cause damage to groundwater quality, such as increased conductivity values due to increased salinity. After 2006, the increase in water level continued (about 15 m), and in 2016, the groundwater levels in the wells reached alarming levels (up to a depth of about 2 m below the ground). According to the data obtained within the scope of this study, this level gradually increased and reached approximately 1.9 meters.

Examining the pre-irrigation and post-irrigation periods reveals that many sampling points have nitrate concentrations exceeding the permitted 50 mg/L. The conductivity values showed little change before and after irrigation periods. Furthermore, the measurements at the same points revealed very

similar results. Examining the pH values revealed similar results in the pre- and post-irrigation periods. This indicates that there is a direct proportional relationship between nitrate and electrical conductivity.

3.1. Nitrate concentrations were obtained in water analyses

The graph in Figure 3 displays the nitrate concentration values pre-irrigation (March) and post-irrigation (October). Fertilizers used in agricultural applications cause nitrate pollution, which belongs to the highest risk class of pollutants. The accumulation of nitrate in the soil is a result of increased agricultural production activities and fertilizer use. Different environmental conditions wash out accumulated nitrate, causing it to move deeper into the soil. Nitrate-reducing bacteria in the soil convert fertilizer to nitrate through nitrification, and because nitrate has a negative charge, it washes away and reaches the groundwater. Even under normal conditions, it is stated that only 50% of nitrogen fertilizers applied to the soil are used by plants, 2-20% is lost through evaporation, 15-25% is combined with organic compounds in clay soil, and the remaining 2-10% is mixed with surface and groundwater [23].

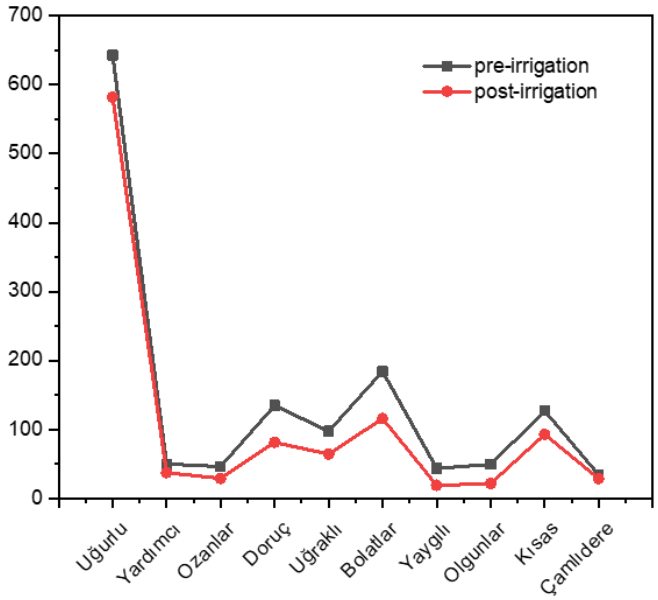

Figure 3. Nitrate values measured in the samples taken from the sampling points in pre- and post-irrigation periods.

In the Harran Plain region, farmers typically plan for cereal cultivation in the autumn season, while they plan for cotton and corn cultivation as a secondary crop between spring and summer. The first planting stages of products grown in dry or irrigated conditions undergo fertilization. Therefore, we apply intensive fertilizer to the soils both during the autumn-winter pre-irrigation period and the spring-summer irrigation period. In this scenario, nitrate leaching from the soils could potentially occur throughout the year. The graph displays very close nitrate values before and after irrigation at all sampling points in the Harran Plain. According to the results of March, which is the pre-irrigation period, the nitrate concentration in the well in Uğurlu town was 642.78 mg/L, which is an alarming level. The nitrate concentration in this well in October was 582.22 mg/L. We observed that the nitrate levels in this case did not significantly change seasonally or before and after irrigation. The region's intensive agricultural activities for many years have led to nitrate pollution in groundwater. However, experts believe that nitrate pollution in the sampling points stems from a multi-year process that began during the irrigation period (1995) in the Harran Plain. It is assumed that the nitrate values in the wells increased

by adding each year and reached today's values, especially as the groundwater levels increased over the years.

3.2. Investigation of nitrate pollution in batch reactor

Excessive use of artificial fertilizers, particularly in intensive agricultural practices, is the primary cause of nitrate levels exceeding the limit values in the groundwater in the study area. Especially in regions with semi-arid-arid climates, the high level of irrigation needs and unconscious irrigation techniques cause nitrate washing in soils and nitrate mixing into groundwater. Various traditional techniques such as adsorption, ion exchange, reverse osmosis, electrochemical, chemical, and biological methods have been developed to remove nitrate from water. However, these have various limitations such as post-treatment re-treatment, less efficiency and high installation costs. Among conventional techniques, the electrocoagulation process is an effective technology for nitrate removal. This is because nitrate anions prefer to stick to the surfaces of metal-hydroxide precipitates that are growing, and the higher the current density, the higher the operational cell potential, which improves the removal efficiency [22].

This study used electrocoagulation, a method that is both effective and easy to apply, for nitrate removal studies. Lacasa et al. [3] carried out nitrate removal studies with EC using Al and Fe electrodes from groundwater. They concluded that EC is an effective process for nitrate removal. Majlesi et al. [24] obtained nitrate removal efficiency of around 96% under optimum time and pH conditions using Al electrodes. The study was based on four different points (Uğurlu, Doruç, Bolatlar, Kısas) where nitrate concentrations were above the limit values as a result of the analyses. EC studies for nitrate removal were carried out on natural groundwater samples taken from four different sampling points in the Harran Plain region of Sanliurfa province.

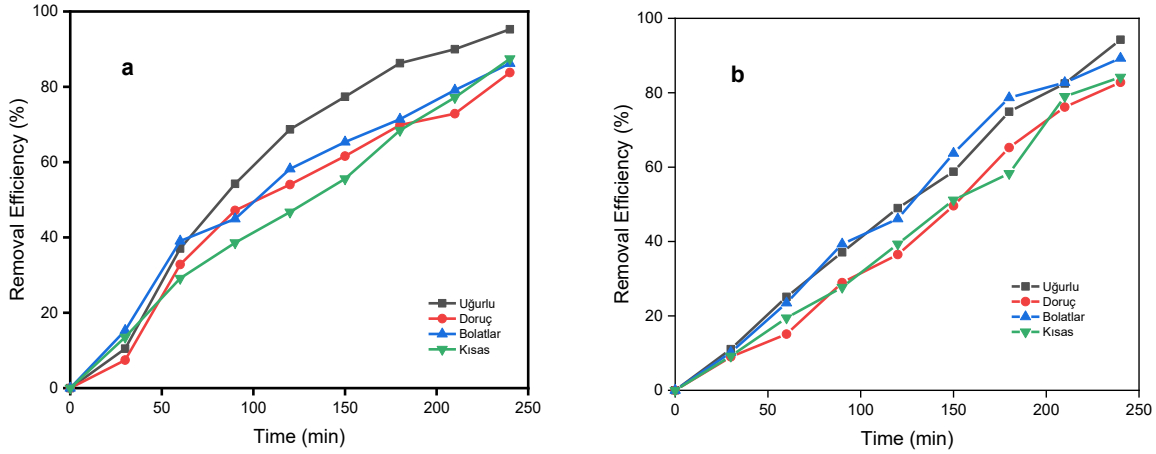

Figure 4. Variations of nitrate removal efficiencies for **(a)** pre-irrigation **(b)** post-irrigation periods during the EC process.

The EC process successfully reduced the nitrate concentration below the maximum pollutant level of 50 mg/L in the pre- and post-irrigation period. Nitrate removal efficiencies for Uğurlu, Doruç, Bolatlar and Kısas in the pre-irrigation period were 95.27%, 83.79%, 86.23% and 87.44%, respectively. In the post-irrigation period, nitrate removal efficiencies for Uğurlu, Doruç, Bolatlar and Kısas are 94.25%, 82.79%, 89.27%, 84.17%, respectively (Figure 4). EC operating conditions and energy consumption are shown in Table 1. According to the results, energy consumption increased as the conductivity decreased. The lowest energy consumption value (0.81 kWh/m^3) corresponded to the highest conductivity (2239 µS/cm).

Table 1. EC operating terms and conditions.

	Electrocoagulation Process							
	Pre-irrigation				Post-irrigation			
Parameter	Uğurlu	Doruç	Bolatlar	Kısas	Uğurlu	Doruç	Bolatlar	Kısas
Electrode material	SS	SS	SS	SS	SS	SS	SS	SS
Current density (mA/cm^2)	2.5	2.5	2.5	2.5	2.5	2.5	2.5	2.5
Temperature (ºC)	18.1	17.8	20.4	18.8	23.1	22.2	24.8	24.6
Initial NO_3^- concentration (mg/L)	642.78	134.76	184.21	126.81	582.22	81.17	115.73	92.91
Final NO_3^- concentration (mg/L)	30.37	21.84	25.36	15.92	33.47	82.79	12.41	14.70
Initial pH	7.31	7.53	7.74	8.33	7.44	8.13	7.32	7.44
Final pH	7.14	7.38	7.45	8.13	7.17	7.76	7.12	7.29
Initial electrical conductivity (µS/cm)	2094	1982	1488	1253	2165	2239	1456	1136
Final electrical conductivity (µS/cm)	1387	1174	768	528	1247	1334	702	486
Operating time (min)	240	240	240	240	240	240	240	240
Nitrate removal (%)	95.27	83.79	86.23	87.44	94.25	82.79	89.27	84.17
Energy efficiency (kWh/m^3)	0.89	0.99	1.02	1.05	0.83	0.81	1.11	1.15

The pH of a solution is one of the most important parameters in the EC process [25]. Especially in this study, pH affected nitrate removal and the performance of the electrochemical process. Throughout the experimental study, water pH was difficult to control due to the instability of the EC process. As shown in Figure 5, both pH and conductivity were measured at certain time intervals. Both decreased as the nitrate removal rate increased. At the end of the study period, pH and conductivity values decreased (Figure 6).

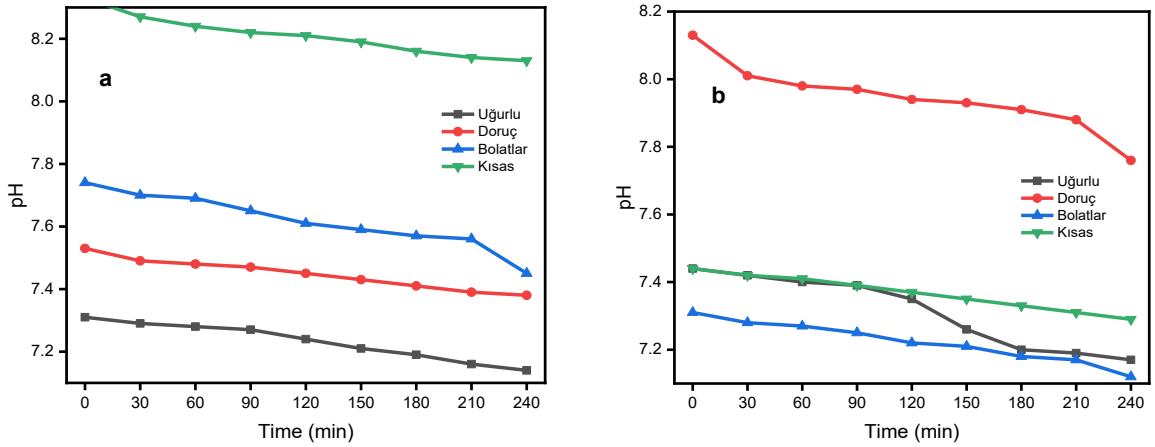

Figure 5. Variation of pH values for **(a)** pre-irrigation **(b)** post-irrigation periods during the EC process.

Operational parameters, including pH and current density, are crucial for optimizing the electrocoagulation process. Research has shown that maintaining a slightly acidic to neutral pH can improve nitrate reduction rates, as the presence of hydrogen ions can facilitate the electrochemical

reactions involved in nitrate reduction [18]. Additionally, higher current densities have been associated with increased removal efficiencies, although they may also lead to higher energy consumption and potential electrode degradation [1,26]. Therefore, a balance must be struck between efficiency and operational costs.

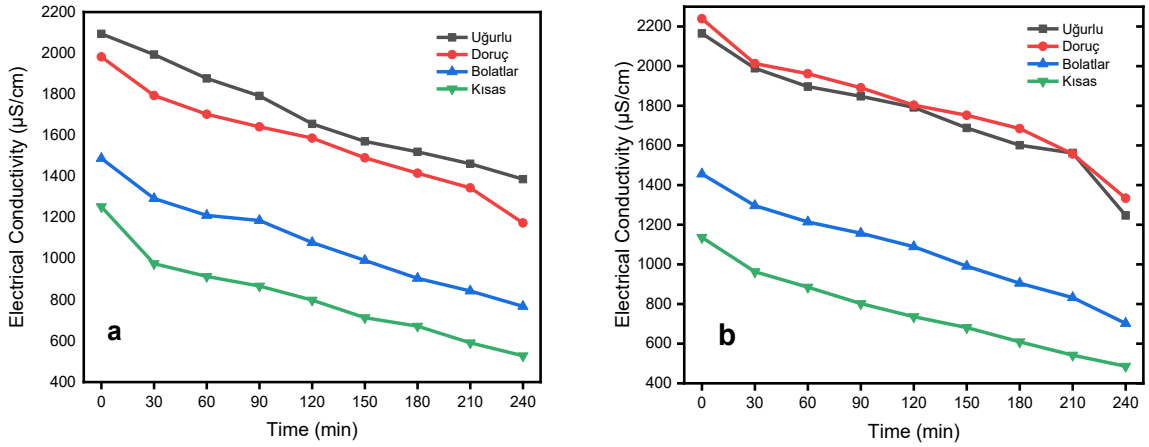

Figure 6. Variation of conductivity values for **(a)** pre-irrigation **(b)** post-irrigation periods during the EC process.

Furthermore, the economic feasibility of electrocoagulation using stainless steel electrodes is supported by its relatively low operational costs compared to traditional methods. The longevity of stainless steel electrodes reduces the frequency of replacements, and the energy consumption can be optimized through careful management of the operational parameters [27]. Studies have indicated that the use of stainless steel in electrocoagulation systems can lead to cost-effective solutions for treating nitrate-laden groundwater, making it an attractive option for municipalities and industries alike [8].

One of the important economic parameters in the EC process is electrical energy consumption. Electric energy consumption is a critical factor in various industrial processes, particularly in wastewater treatment technologies such as electrocoagulation. The energy consumption in electrocoagulation is primarily determined by the current density applied during the treatment process. Higher current densities can enhance the removal efficiency of contaminants but also lead to increased energy costs. For instance, studies have shown that optimizing current density can lead to significant reductions in energy consumption while maintaining effective pollutant removal [28,29]. Specifically, a current density of around 20 mA/cm² has been identified as effective for various applications, balancing energy use and treatment efficiency. The study reports energy consumptions of 0.143 kWh/kg of suspended solids (SS) for aluminum electrodes and 0.0571 kWh/kg SS for iron electrodes under optimized conditions [30]. This information is crucial for understanding the operational costs and energy efficiency of electrocoagulation as a drinking water treatment method.

4. Conclusion

The reactor established within the scope of the present study was operated as a batch. Samples were taken from 10 different sampling points and only 4 points (Uğurlu, Doruç, Bolatlar and Kısas) showed nitrate concentrations above the limit values. Therefore, EC studies were carried out using water samples from only these 4 sampling points. The study was carried out using SS electrodes. The SS values measured at the end of the EC process were < 0.4. In other words, the SS value passing into the water is very low and has no adverse effect on human health. In the pre-irrigation period, nitrate removal efficiencies for Uğurlu, Doruç, Bolatlar and Kısas were 95.27%, 83.79%, 86.23%, 87.44%, respectively.

In the post-irrigation period, nitrate removal efficiencies for Uğurlu, Doruç, Bolatlar and Kısas were 94.25%, 82.79%, 89.27%, 84.17%, respectively. According to the results, energy consumption increased as conductivity decreased. In this study, a cost of $1.06 per m^3 was calculated for SS electrode nitrate removal using current electricity costs for groundwater at 4 points taken from Harran Plain. It was observed that the SS-SS electrode combination used in the studies provided a good efficiency. The system can be developed and designed on a pilot scale in accordance with the needs of the region and on-site treatment can be carried out. It is thought that this method can also be applied to regions with the same characteristics as the arid/semi-arid study region. The laboratory-scale removal process that has been designed and implemented has created the foundation for future pilot-scale applications and portable EC system applications.

Ethical Statement

The author declares that this document does not require ethics committee approval or any special permission. This study does not cause any harm to the environment.

Conflict of Interest

The author declares no conflict of interest.

Author Contribution

B.Y.K. conducted the fieldworks and collected all data and wrote the manuscript.

Generative AI statement

The author declares that no Gen AI was used in the creation of this manuscript.

References

[1] Nasrullah, M., Siddique, M., Zularisam, A., "Effect of high current density in electrocoagulation process for sewage treatment". *Asian Journal of Chemistry*, 26(14), 4281-4285, 2014. Doi: 10.14233/ajchem.2014.16134.

[2] Bharath, M., Krishna, B.M., "Electrocoagulation treatment for landfill leachate using stainless steel electrode". *International Journal of Engineering and Advanced Technology*, *9*(1), 2851-2855, 2019. Doi: 10.35940/ijeat.a9807.109119.

[3] Lacasa, E., Cañizares, P., Sáez, C., Fernández, F., Rodrigo, M., "Removal of nitrates from groundwater by electrocoagulation". *Chemical Engineering Journal*, 171(3), 1012-1017, 2011. Doi: 10.1016/j.cej.2011.04.053.

[4] Dehghani, M., Hoseini, M., Fath-Aabaadi, M., Elhamiyan, Z., Shamsedini, N., Ghanbarian, M., …, Baghani, A., "Optimizing electrocoagulation process for the removal of nitrate from aqueous solution." *Jundishapur Journal of Health Sciences*, 8(1), 2016. Doi: 10.17795/jjhs-31095.

[5] Amarine, M., Lekhlif, B., Mliji, E., Echaabi, J., "Nitrate removal from groundwater in Casablanca region (Morocco) by electrocoagulation". *Groundwater for Sustainable Development*, 11, 100452, 2020. Doi: 10.1016/j.gsd.2020.100452.

[6] Hussein, R., Elmolla, A., Ahmed, A., Mohamed, A., "Effect of spacing of different types of electrodes in the electrocoagulation process". *Journal of Al-Azhar University Engineering Sector*, 17(64), 919-931, 2022. Doi: 10.21608/auej.2022.253825.

[7] Yehya, T., Balla, W., Chafi, M., Audonnet, F., Vial, C., Essadki, A., …, Gourich, B., "Assessment of denitrification using electrocoagulation process". *The Canadian Journal of Chemical Engineering*, 93(2), 241-248, 2014. Doi: 10.1002/cjce.22112.

[8] Apshankar, K., Goel, S., "Nitrate removal from drinking water using direct current or solar powered electrocoagulation". *SN Applied Sciences*, 2(2), 2020. Doi: 10.1007/s42452-020-2069-9.

[9] Sun, J., Garg, S., Xie, J., Zhang, C., Waite, T., "Electrochemical reduction of nitrate with simultaneous ammonia recovery using a flow cathode reactor". *Environmental Science and Technology*, 56(23), 17298-17309, 2022. Doi: 10.1021/acs.est.2c06033.

[10] Sun, J., "A novel integrated flow-electrode capacitive deionization and flow cathode system for nitrate removal and ammonia generation from simulated groundwater". *Environmental Science and Technology*, 57(39), 14726-14736, 2023. Doi: 10.1021/acs.est.3c03922.

[11] Kargı, F., Pamukoglu, M.Y., "Adsorbent supplemented biological treatment of pre-treated landfill leachate by fed-batch operation". *Bioresource Technology*, 94(3), 285-291, 2004. Doi: 10.1016/j.biortech.2004.01.003.

[12] Kargi, F., Pamukoglu, M.Y., "Simultaneous adsorption and biological treatment of pre-treated landfill leachate by fed-batch operation". *Process Biochemistry*, 38(10), 1413-1420, 2003. Doi: 10.1016/S0032-9592(03)00030-X.

[13] Kalaruban, M., Loganathan, P., Kandasamy, J., Naidu, R., Vigneswaran, S., "Enhanced removal of nitrate in an integrated electrochemical-adsorption system". *Separation and Purification Technology*, 189, 260-266, 2017. Doi: 10.1016/j.seppur.2017.08.010.

[14] Emiliani, B., Ariza, Y., Quiñones, D., Plaza, J., "Effect of operating conditions on the treatment of cr (vi) containing wastewater by electrocoagulation with aluminum and stainless steel electrodes". *Ecs Transactions*, 100(1), 95-107, 2021. Doi: 10.1149/10001.0095ecst.

[15] El-hefny, R., Monem, N., "Treatment of groundwater by using the electrocoagulation technique". *Engineering Research Journal - Faculty of Engineering (Shoubra)*, 51(1), 50-55, 2022. Doi: 10.21608/erjsh.2022.224285.

[16] Yengejeh, S., Mansoorian, H., Majidi, G., Yari, A., Khanjani, N., "Efficiency of electrical coagulation process using aluminum electrodes for municipal wastewater treatment: a case study at karaj wastewater treatment plant". *Environmental Health Engineering and Management*, 4(3), 157-162, 2017. Doi: 10.15171/ehem.2017.22.

[17] Mershed, B., "Nitrate removal from water using electrocoagulation with activated carbon". *Journal of Engineering Sciences and Information Technology*, 6(2), 111-135, 2022. Doi: 10.26389/ajsrp.c130821.

[18] Amouei, A., Pouramir, M., Asgharnia, H., Mehdinia, M., Shirmardi, M., Fallah, H., …, Tabarinia, H., "Evaluation of the efficiency of electrocoagulation process in removing cyanide, nitrate, turbidity, and chemical oxygen demand from landfill leachate". *Environmental Health Engineering and Management*, 8(3), 237-244, 2021. Doi: 10.34172/ehem.2021.27.

[19] Abdelshafy, N., Sadik, M., "Environment -friendly processes: electrocoagulation and activated carbon filtration for reuse of textile wastewater". *Egyptian Journal of Chemistry*, 64(8), 3997-4003, 2021. Doi: 10.21608/ejchem.2021.63363.3358.

[20] Al-Marri, S., Alquzweeni, S., Hashim, K., Alkhaddar, R., Kot, P., Alkizwini, R., …, Al-Khafaji, Z., "Ultrasonic-electrocoagulation method for nitrate removal from water". *IOP Conference*

Series Materials Science and Engineering, 888(1), 012073, 2020. Doi: 10.1088/1757-899x/888/1/012073.

[21] Yazici Karabulut, B., Atasoy, A.D., Can, O.T. et al., "Electrocoagulation for nitrate removal in groundwater of intensive agricultural region: a case study of Harran plain, Turkey". *Environmental Earth Sciences*, 80, 190, 2021. Doi: 10.1007/s12665-021-09488-8.

[22] Yazici Karabulut, B., Atasoy, A.D., Yesilnacar, M.I., "Removal of nitrate from aqueous solutions by batch electrocoagulation process using al and fe plate electrodes". *Harran University Journal of Engineering*, 4, 79-88, 2019.

[23] Kahraman, N., Yazici Karabulut, B., Atasoy, A.D., Yeşilnacar, M.I., "Harran Ovası serbest akiferinde yaz ve kış dönemleri nitrat kirliliğinin araştırılması (2014- 2015)". *Harran Üniversitesi Mühendislik Dergisi*, 2, 1-8, 2016.

[24] Majlesi, M., Mohseny, S.M., Sardar, M., Golmohammadi, S., Sheikhmohammadi, A., "Improvement of aqueous nitrate removal by using continuous electrocoagulation/electroflotation unit with vertical monopolar electrodes", *Sustainable Environment Research*, 26, 287-290, 2016.

[25] Bensadok, K., Benammar, S., Lapicque, F., Nezzal, G., "Electrocoagulation of cutting oil emulsions using aluminium plate electrodes". *Journal of Hazardous Materials*, 152, 423-430, 2018. Doi: 10.1016/j.jhazmat.2007.06.121

[26] Mahmood, R., Al-Musawi, N., "Evaluating electrocoagulation process for water treatment efficiency using response surface methodology". *Journal of Engineering*, 26(9), 11-23, 2020. Doi: 10.31026/j.eng.2020.09.02.

[27] Gad, E., "Electrochemical treatment of industrial effluent and its impact on stainless steel corrosion". *International Journal of Electrochemical Science*, 17(12), 221211, 2022. Doi: 10.20964/2022.12.14.

[28] Yazdanbakhsh AR, Kashefasl M, Zareh H, Agaiani E, Sardar M, Sheikhmohammadi A., "Thickening of biological sludge by electro-coagulation-fotation process". *International Journal of Electrochemical Science*, 10(3), 746-756, 2015.

[29] Asaithambi, P., Beyene, D., Aziz, A. R. A., Alemayehu, E., "Removal of pollutants with determination of power consumption from landfill leachate wastewater using an electrocoagulation process: optimization using response surface methodology (RSM)". *Applied Water Science*, *8*, 1-12, 2018.

[30] Ozyonar, F., Karagozoglu, B., "Systematic assessment of electrocoagulation for the treatment of marble processing wastewater". *International Journal of Environmental Science and Technology*, *9*, 637-646, 2012.

Middle East Journal of Science

https://dergipark.org.tr/mejs

MEJS

e-ISSN:2618-6136

Research Article

OPTIMIZED RELAY LENS DESIGN FOR HIGH-RESOLUTION IMAGE TRANSMISSION IN MILITARY TARGET DETECTION SYSTEMS

Burak ÇELİK*[1], Kıvanç DOĞAN [2], Ezgi TAŞKIN [1], Ayhan AKBAL[2], Ahmet ORHAN [2]

[1]Kocaeli University, Electronic and Communication Enginnering, Kocaeli, Turkiye
[2]Fırat University, Electrical and Electronics Enginnering, Elazığ, Türkiye
* Corresponding author; burak.celik@kocaeli.edu.tr

Abstract: *The design and performance analysis of relay lenses that provide high-performance image transmission for target acquisition and tracking in military optical systems. Relay lenses are critical components for clear and lossless image transmission over long distances. In this study, the optical performance of a relay lens system designed and optimized using ZEMAX software is investigated in detail. The analysis focuses on important optical properties such as modulation transfer function (MTF), spot diagrams, Seidel diagram, field curvature and distortion. The results show that the lens has significant potential in military applications for target detection and tracking with high resolution and low aberration.*

Keywords*: Military Optical Systems, Zemax, Relay Lens, Lens Design*

Received:November 29, 2024 *Accepted:January 17, 2025*

1. Introduction

Military optical systems provide high-performance and reliable monitoring for target identification and tracking in critical missions. These systems have become indispensable in modern warfare, where the ability to process and analyze real-time visual data can determine the success or failure of operations. By combining advanced optical technologies with robust design methodologies, military systems aim to deliver precise and effective solutions for a variety of applications. In this context, optical components must ensure exceptional image clarity, resolution, and durability to withstand challenging operational environments. Electro-optical systems, which have critical features such as simultaneous image transmission, stand out in military fields by allowing intelligence, reconnaissance, surveillance, and targeting. These systems empower military personnel to detect, identify, and track targets across long distances, often in complex and dynamic scenarios. Moreover, many modern armies around the world are investing in Augmented Reality (AR) and Virtual Reality (VR) tools to elevate their systems, gain superiority over opposing forces, and prevent losses on the battlefield [1]. In these systems, relay lenses are essential components for transmitting images clearly and without loss over long distances. These lenses ensure the integrity and fidelity of transmitted images, a requirement that is particularly vital in time-sensitive and mission-critical operations. The proper use of relay lenses in technologies such as thermal cameras is of great importance for military security [2]. Thermal imaging systems, for instance, rely heavily on relay lenses to maintain image quality, enabling operators to detect threats even in low-visibility conditions. In systems like laser rangefinders (LRF) and laser target designators (LTD), the use of relay lenses is critical for directing laser beams accurately

toward the target and ensuring precise focusing. These systems demand optical precision to achieve accurate target engagement, particularly in environments where atmospheric conditions and distance pose significant challenges. Laser weapons can be either ground-based or space-based. Ground-based laser weapons use multiple relay mirrors in space to intercept a theater ballistic missile. The relay mirror(s) is alens or group of lenses that transmits a finite object to a distant location with a magnification of unity or bigger values. Also they are used to extend the range of high-energy laser weapons as they compensate the limiting factors due to atmospheric absorption, turbulence and the curvature of the Earth [3]. It is a lens or group of lenses that transmits a finite object to a distant location with a magnification of unity or another value [4-5]. They are used in rifle sights, military infrared imaging systems. The use of relay lenses is quite wide as rifle sights, military imaging systems, biomedical applications [6-9] and image applications [10]. This versatility highlights the importance of designing relay lenses that can meet diverse and demanding operational requirements. In this study, a relay lens was designed and optimized in ZEMAX environment for use in rifle sights. By addressing key performance parameters such as resolution, field curvature, and distortion, this work aims to contribute to the development of high-performance optical solutions tailored for military applications.

This study follows a systematic framework to examine various aspects of the research. In chapter 2: Materials and Methods details the methodologies and processes used in the lens design process at ZEMAX. In chapter 3: Optical Design and Analysis focuses on the design of the lens and their analysis in the design process. In chapter 4: Optimization and Material Selection deals with the refinement of the parameters and criteria for selecting suitable materials. In chapter 5: Figures and Analysis presents the visualization of the obtained data and the related analysis. In chapter 6: Conclusions highlights the main findings of the study. Finally, in chapter 7: Recommendations provides suggestions for future work.

2. Material and Method

ZEMAX is a program that can assist in the modeling, analysis and design of optical systems. The interface to ZEMAX is designed to be easy to use and with a little practice can allow very fast interactive design [11]. During the design process, the determination of the optical parameters, the analysis and the evaluation of the system performance were carried out by means of this software. Hammer and Global optimization methods are used in ZEMAX software to reduce aberration. These methods are very similar and share the same functional basis [12]. During the design process, optimization was performed using the Hammer optimization algorithm in order to minimize the aberrations in the optical system.

Relay lenses are an important group of lenses used to transfer lossless and clearly from a certain distance to another optical plane. These objects usually consist of two or more lens elements. Before starting the relay lens design, basic parameters such as focal length (EFFL) and total length (TOTR) and aperture diameter were determined considering the application where the system will be used. The performance of the design was evaluated by metrics such as modulation transfer function (MTF), spot diagram and distortion analysis. Hammer optimization was applied to improve this performance. The aim was to minimize aberrations and improve image quality. Different material combinations were tried to reduce optical aberrations.

3. Experimental Study

This study focuses on the design and optimization of a relay lens in a ZEMAX environment specifically designed for military applications. Lens system parameters including effective focal length (EFFL), total optical path length (TOTR), aperture, and field of view (FOV) in a ZEMAX environment were determined and analyzed to meet specific system requirements.

3.1. Optical Design and Analysis

In this study, the relay lens designed in ZEMAX environment is optimized for military applications. During the design process, the optical parameters of the lens were carefully determined and analyzed. The requirements of the system were analyzed and parameters such as focal length (EFFL), total optical path (TOTR), aperture and field of view (FOV) were determined. It was aimed to be suitable for use on the weapon and to have a compact structure. Designed in the ZEMAX environment, the relay lens is optimized for military applications. During the design process, the optical parameters of the lens were carefully determined and analyzed. By analyzing the system requirements, parameters such as focal length (EFFL), total optical path (TOTR), aperture and field of view (FOV) were determined. It was aimed to be suitable for use on weapons and to have a compact structure. The EFFL value is approximately 9.5 mm. A short focal length provides a wider field of view. A focal length of 9.5 mm covers a wide area at close range for a compact system. A TOTR value of 20 mm provides a compact design that meets the requirements of portability and lightness. A 3 mm aperture provides sufficient light collection, but a wider aperture may be required in low light conditions. The results obtained in this process determined the focusing ability, image quality and other optical characteristics of the lens. The relay lens obtained in ZEMAX environment is designed to be used in this field. The performance of the optical system is determined by the spot diagram, field curve/distortion diagram and modulation transfer function (MTF)[13]. In this study, the analysis results of the designed lens such as MTF, PSF, Spot Diagram, Image Simulation, Seidel Diagram, Field curvature and distortion are obtained and the Shaded model is presented. MTF evaluation of image displays is often needed to evaluate objective image quality, especially in the application of image quality measurements.

3.2. Optimization and Material Selection

After the lens assembly of the design was completed, different materials were tested for the lenses. The materials were optimized with the help of Hammer optimization to achieve the best image quality and low aberrations. The materials that achieved high image quality, low distortion and eliminated optical aberrations were determined. These optical aberrations are astigmatism, spherical aberrations and comas. The goal of the design is to achieve the best image quality. Hammer analysis aims to find the global minimum of the design. For this reason, materials suitable for the substituted surfaces were obtained as a result of optimization by using the “Materials Catalog” during Hammer analysis.

MATERIALS
LAK8
LAK11
KZFS6
BAF51
F7
KZFS1
N-SK2HT
K5G20
SK14
LAKL12

Figure 1. Materials obtained as a result of Hammer optimization algorithm analysis

4. Design of Relay Lens

In this section, we present a detailed analysis of the optical design and its performance metrics to evaluate its suitability for high-performance image transfer in military optical systems, specifically targeting detection and tracking applications. The analyses provide a comprehensive understanding of the system's imaging quality, aberration control, and overall performance across critical parameters. The evaluation begins with the Modulation Transfer Function (MTF), a crucial metric that illustrates the spatial frequency response and resolution capability of the optical system. Subsequently, the Point Spread Function (PSF) is analyzed to assess the system's energy distribution and imaging fidelity. To further complement these metrics, the Spot Diagram offers insight into the system's aberration characteristics at various field positions. The Seidel Diagram is used to dissect the contributions of primary aberrations, enabling an understanding of the root causes of optical imperfections. Moreover, the Field Curvature and Distortion analysis is undertaken to assess the system's ability to maintain a flat image plane and minimize geometric distortions. Advanced image evaluation is performed through Extended Diffraction Image Analysis, Geometric Image Analysis, and Demo Image Analysis, which collectively provide both diffraction-limited and ray-based perspectives of imaging performance. The Merit Function optimization results are included to highlight the design's adherence to performance goals, while the Optical Path Difference (OPD) Fan Analysis offers a quantitative assessment of wavefront errors across the aperture.

By combining these analyses, we provide a holistic evaluation of the designed optical system, ensuring its robustness and efficiency for demanding military applications. The results highlight the design's capability to deliver precise, high-quality imagery for critical target detection and tracking scenarios.

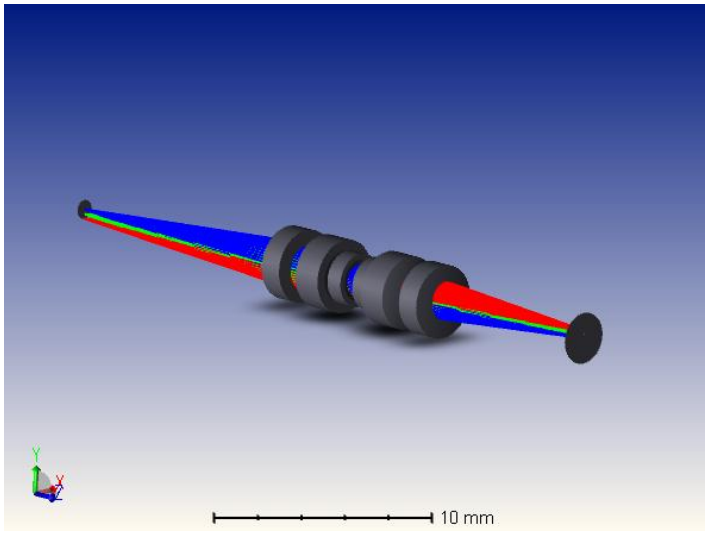

Figure 2. Shaded Model

As a result, Figure 2 provides a detailed visualization of the structural design and shows the arrangement and interaction of optical components within the system.

This model shows the ray tracing simulation of the relay lens system designed in the ZEMAX environment. The shaded model in the figure presents the system's performance in focusing beams of different colors. The uniform focusing of the beams and the minimization of aberrations demonstrate the success of the optimization techniques applied during the design process.

4.1. Modulation Transfer Function

The analysis result in Figure 3 shows the modulation transfer function (MTF) of the lens versus spatial frequencies. Diffraction-limited resolution in the MTF plot has been a fundamental method for determining optical resolution [14]. MTF represents the transmitted contrast. The MTF plot shows how sharply the system transmits structures at spatial frequencies above the Nyquist frequency [15]. Accurate optical resolution is indispensable to ensure that instrumentation and analytical techniques give the required image quality [14]. According to the obtained MTF plot, the MTF values of the lens in the range of 0-150 cycles\mm are quite high (around 0.45). This shows that at low and medium frequencies the optical system achieves high contrast and clear images. Low frequencies usually represent large and distinct details. After 350 cycles\mm, the MTF starts to go completely to zero and at this point contrast transmission is very difficult. However, this drop in high frequencies is always to be expected.

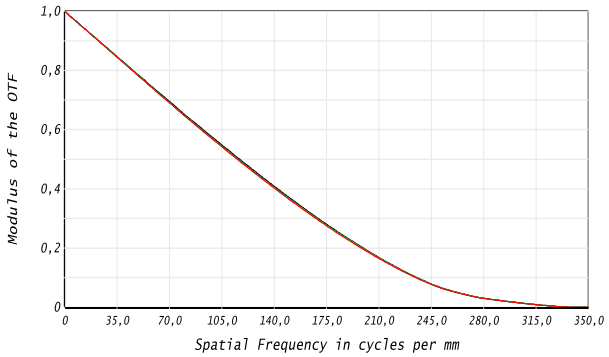

Figure 3. Modulation Transfer Function

As a result, Figure 3 showing the MTF plot, demonstrates the ability of the lens to effectively resolve spatial frequencies and provides a quantitative assessment of imaging performance and contrast accuracy across the field of view.

4.2. Point Spread Function

Point spread function (PSF) analysis shows where the point sources of the optical system are shifted. The contrast detection limit within a PSF is determined by the photon noise and speckle noise in the image [16]. Figure 4 shows the PSF analysis result of the lens system. According to the analysis result of the obtained design, it is revealed that the lens is focused with minimal propagation of point shifts and provides high resolution. This is shown by the fact that the relative irradiance value reaches 1 in the curve.

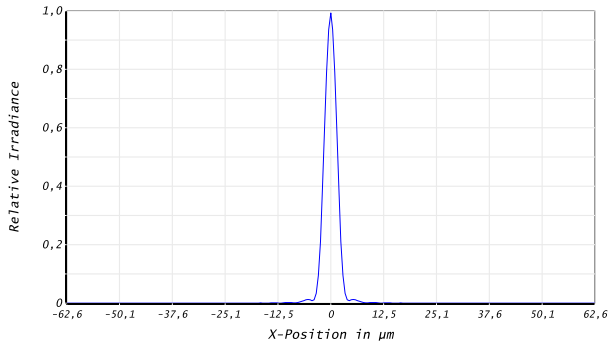

Figure 4. Point Spread Function

As a result, Figure 4 shows the response of an optical system to a point source and shows how a single point of light spreads across the image plane.

4.3. Spot Diagram

The spot diagram shows the focusing ability of the optical system and the aberrations in the image. Figure 5 shows the spot diagrams of the lens system. It has a high focusing ability in the 0.00 (deg), 0.60 (deg) and 1.20 (deg) areas. It indicates the angular areas that the optical system can image. The IMA value indicates the distance of the imaging area at these angles to the point formed on the image plane of the optical system. The results obtained show that the lens successfully focuses the rays coming from different angles to the points specified in the design phase and provides high accuracy with low deviation values. In addition, the small RMS and GEO radius values obtained in the analysis and shown in the graph mean that the optical system works with very good focusing and low aberration. As a result, the RMS radius of the three fields of view is quite smaller than the airy disk radius. This shows that the effect of improving the aberrations is significant.

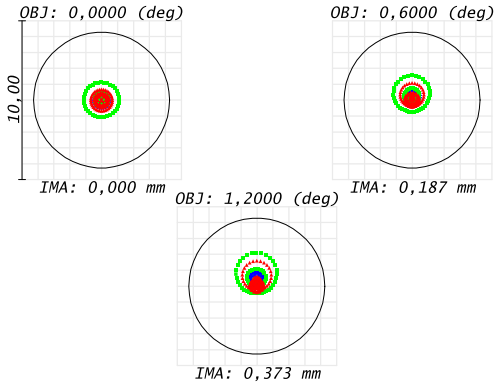

Figure 5. Spot Diagram.

As a result, Figure 5 represents the distribution of light from a point source as it passes through an optical system and shows the size and location of diffraction-limited spots at various points along the image plane.

4.4. Seidel Diagram

Seidel diagram is a diagram that shows the optical aberrations in the designed lenses according to their individual surfaces. According to the diagram obtained in Figure 6, optical aberrations are shown according to individual surfaces. As a result of the optimizations made in the SUM section at the end of the diagram, the optical aberrations transferred from the first surfaces were minimized.

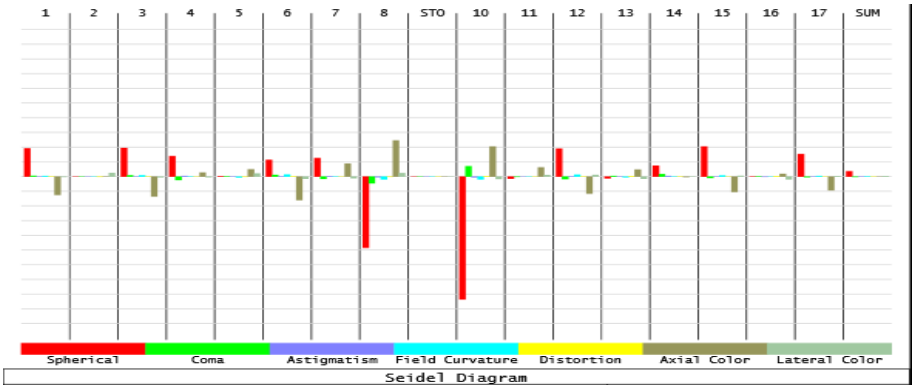

Figure 6. Seidel diagram.

The Seidel diagram in Figure 6 visualizes the primary aberrations (spherical, coma, astigmatism, field curvature and distortion) of an optical system.

4.5. Field Curvature and Distortion

The analysis of field curvature and distortion, presented in Fig. 7, demonstrates the deformation within the design. Significant field curvature and distortion can lead to poor image quality and positional errors for moving targets, while also negatively affecting the seamless mosaicking of component images [17]. The design analyses following the optimizations demonstrate that the relay lens delivers high performance in military optical systems. The maximum distortion was found to be 0.0118%, a notably low value that indicates the design achieves exceptionally high resolution with remarkably low distortion.

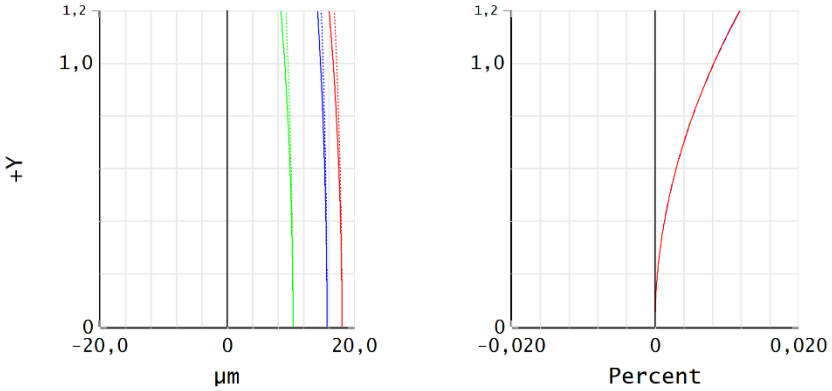

Figure 7. Field Curvature and Distortion.

Field curvature describes the change in focus along the image plane where a flat object appears curved in the image. Distortion refers to the change in shape of an image, often causing straight lines to appear curved.

The Seidel diagram analysis indicates that aberrations in the optical system have been minimized. The PSF cross-sectional image demonstrates the system's high focal point accuracy. The MTF analysis reveals that the system performs well over a wide frequency range, achieving significant modulation transfer values. Furthermore, the spot diagram confirms the optical system's focusing precision and image quality.

4.6. Image Analyses

These analyses are commonly used to identify, measure, and interpret objects, features, patterns, and structures within an image. Fig. 8 presents the extended diffraction image analysis graph, which illustrates how the optical system processes an image through diffraction. In the image, a large "F" character is represented by varying intensity levels, reflecting the frequency and sharpness of the lens system. The details of the character are clearly visible. Diffraction-induced spreading may cause slight blurring at the edges of the image. However, the edges of the character remain clearly visible, which indicates that the diffraction effect is minimal and the details are well-preserved. The color scale on the graph represents the normalized values of light intensity and contrast (0.0–1.0). Along the edges of the character, the intensity ranges between 0.6 and 1.0, indicating high contrast transfer. This demonstrates that the system provides clear imaging, particularly at low and medium spatial frequencies. The simulation was scaled to produce an image with a resolution of 4096 × 4096 pixels, enabling a high-resolution assessment. Diffraction-induced spreading may cause slight blurring at the edges of the image. However, the edges of the character remain clearly visible, indicating that the impact of diffraction is reduced. In the geometric image analysis presented in Fig. 9, it is shown how the optical system is geometrically imaged and that the system is not affected by geometric distortions. The

efficiency value of 100.00% observed in the figure indicates that the system utilizes energy very efficiently, with all energy contributing to the image formation process.

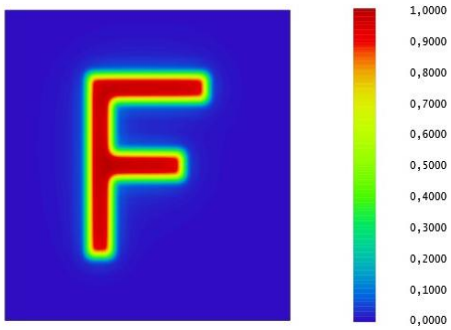

Figure 8. Diffraction Image Analysis

Figure 8 depicts the diffraction-limited performance of the lens system, highlighting its ability to produce high-quality and sharp images.

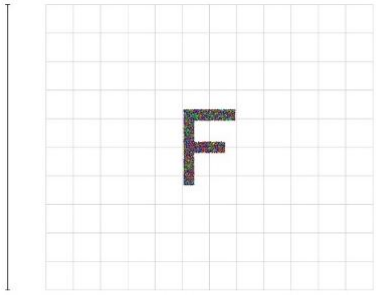

Figure 9. Geometric Image Analysis.

This analysis examines how well the system preserves the geometry of objects, including measurement of distortions, field curvature, and other geometric deviations.

a) Before Optimization b) After Optimization

Figure 9. Demo Image Analysis Before and After Optimization

Demo Image Analysis demonstrates the performance of the optical system through real-world imaging. The demo image analysis shown in Figure 10 is a basic reference for evaluating the performance of the design. By analyzing the clarity of details, sharpness, distortion and deviations in the image, it is understood whether the design meets the targeted criteria.

4.7. Merit Function

The merit function is a numerical parameter used to evaluate the conformity of an optical system to specific performance criteria. It serves as an error metric, indicating how closely the design aligns with the desired optical performance. Typically, it is employed to minimize deviations from target values. As the merit function value approaches zero, the design becomes more ideal and better aligned with the specified parameters.

The merit function value for our design is shown to be 0.0144008. This value demonstrates that the design is very close to meeting the targeted performance criteria and that design errors have been minimized. A low merit function value indicates that the optical system possesses high resolution and achieves the desired optical quality. This result highlights the design's success in terms of optical performance and confirms that it has been optimized to meet the targeted imaging specifications.

Merit function combines various criteria such as deviations and image quality into a single value that guides the optimization process to achieve the best possible design.

4.8. Optical Path Difference

The Optical Path Difference (OPD) Fan plot is used to measure and quantify deviations of light waves from the ideal wavefront in the optical system. In an ideal scenario, a wavefront is a surface where light waves are in phase, meaning their optical paths are identical. In practice, however, this ideality is unattainable due to inherent material properties and design limitations, which result in deviations from the ideal wavefront. Fig. 12 presents the OPD Fan plot for our optical system. The analysis shows that the OPD deviations are confined within ±0.1 waves, highlighting the system's superior optical performance with minimal deviations. For an aberration-free system, the aberration curve should be a straight line coinciding with the x-axis [18]. The OPD Fan plot of our design indicates that the P_x and P_y curves exhibit a generally flat and consistent profile, demonstrating that the aberrations and field curvature are well corrected and maintained at minimal levels. Moreover, the consistent OPD profiles across varying field angles (0°, 0.6°, 1.2°) underscore the system's ability to deliver robust performance over a wide field of view.

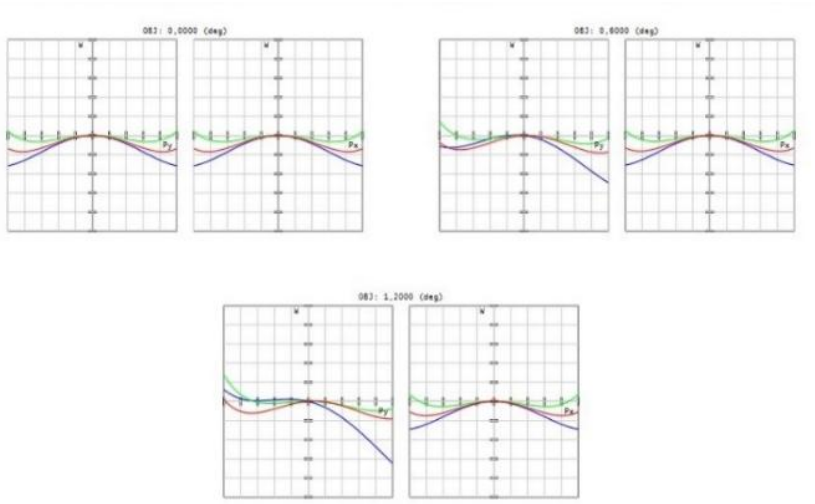

Figure 12. Optical Path Difference Fan Analysis.

Figure 12 evaluates the performance of the system in terms of deviations and determining the changes in optical path lengths and phase differences throughout the optical system.

5. Results and Discussions

As a result, the analyses performed show that the designed optical system meets the targeted performance criteria and the design is successfully optimized. According to the MTF analysis, sufficient contrast transfer is provided, and the PSF analysis confirms that the lens focuses the point shifts with minimal spread, achieving high resolution. In addition, the spot diagram shows that the lens focuses the rays coming from different angles to the points specified in the design phase with low deviation values and provides high accuracy. The Seidel diagram shows that the optical defects on the lens surfaces are minimized.

The maximum distortion value remains at a low level of 0.0118%, confirming that the design achieves high resolution and low distortion. The Extended Diffraction Image Analysis results show that the system preserves high-resolution details and that the diffraction effect is at a minimum level. The geometric image analysis reveals that the optical system operates with high efficiency and without geometric distortions. The effective focal length (EFFL) value of the system in the design is approximately 9.5 mm. In optical systems, the EFFL value directly affects the imaging of the system and the distance between the target and the sight. The effective focal length of 9.5 mm is especially suitable for compact and lightweight optical systems. In portable systems such as rifle sights, this focal length provides a wide personal field of view. This wide field of view offers advantages in terms of rapid target acquisition and aiming. Another parameter in the design is the total optical path (TOTR). The TOTR value of our system is approximately 20 mm. The TOTR value determines the overall dimensions and portability of the optical system. The total length of 20 mm maintains the compactness of this design. Especially in military applications, the lightness and ease of use of the sight are essential. This design meets these features. The aperture value allows the system to collect light and, therefore, affects the image brightness. While the aperture is 3 mm in size, it provides sufficient light collection ability, and at the same time, the system has a positive effect on the depth of field. This provides sharp focus on the target, especially at different distances, which is a critical feature for rifle sights. The high values obtained in the MTF analysis reveal that the design can provide the contrast required for sighting applications. This helps to accurately detect the target by providing clear and sharp images. The low merit function value confirms that the optical system has high resolution and provides the desired optical quality. All these findings emphasize that the designed optical system can be used as a high-performance relay lens for applications such as target acquisition and tracking in military optical systems. According to the optical path difference analysis, the system showed good optical performance with minimal aberrations. The consistent profiles of the OPD values showed that the system has robust performance across a wide field of view.

6. Recommendations

These design parameters and analysis results demonstrate that the system is suitable for weapon-mounted sights requiring precise aiming at short distances. For applications involving longer distances, the focal length would need to be increased. To enhance performance under low-light conditions, the aperture size should be optimized accordingly. While implementing these solutions, the results of the MTF analysis must confirm the adequacy of the design in terms of contrast and resolution. This requirement should also be validated by other analyses.

Ethical statement

Not applicable.

Acknowledgment

The authors have no acknowledgments to declare.

Conflict of interest

The authors must notify any conflicts of interest.

Authors' Contributions

B.C: Conceptualization, Methodology, Investigation, Resources, Software, Data Curation, Writing - Original Draft, Writing - Review & Editing, Visualization.

K. D: Conceptualization, Methodology, Resources, Investigation.

E. T: Conceptualization, Methodology, Resources, Investigation.

A.A: Supervision, Validation, Formal Analysis, Writing - Review & Editing, Project Administration.

A.O: Supervision, Validation, Formal Analysis, Writing - Review & Editing, Project Administration.

All authors read and approved the final manuscript.

Generative AI statement

The author(s) declare that no Gen AI was used in the creation of this manuscript.

References

[1] İçten, T., Bal, G., "Askerî alanda artırılmış ve sanal gerçeklik araçlar: sistemler, zorluklar ve çözümler", *Savunma Bilimleri Dergisi*, *2*(40), 169-199, 2021.

[2] Christofer., Torsten., Martin., Manfred., Lukas., Denis., Nicolas., Dirk., Hans.," Design and testing of cryogenic infrared relay optics*", In Image Sensing Technologies: Materials, Devices, Systems, and Applications., 11388,* 53-65, 2020.

[3] Kaushal, H., Kaddoum, G., "Applications of lasers for tactical military operations", *IEEE Access*, 5, 20736-20753, 2017.

[4] Thöniss, T., Adams, G., Gerhard, C., "Optical System design: Software Tools Cover Envelope Calculations to the Final Engineering Drawings", *Optik and Photonik*, 4(2), 30-33, 2009.

[5] O'Shea, K., Lens design approach to optical relays. The University of Arizona., 2006.

[6] La, M., Park, S. M., Kim, W., Lee, C., Kim, C., Kim, D. S., "Injection molded plastic lens for relay lens system and optical imaging probe*", International Journal of Precision Engineering and Manufacturing*, 16, 1801-1808, 2015.

[7] Ou-Yang, M., Hsieh, Y. F., Lee, C. C., Biopsy diagnosis of oral carcinoma by the combination of morphological and spectral methods based on embedded relay lens microscopic hyperspectral imaging system, *Journal of Medical and Biological Engineering*, 35, 437-447, 2015.

[8] Dobson, S. J., Hopkins, H. H., "A new rod-lens relay system offering improved image quality", *Journal of Physics E: Scientific Instruments*, 22(7), 450, 1989.

[9] Yao-Fang., Mang., Jeng-Ren., Jin-Chern., Nai-Wen., Chia-Ing., Ming-Hsui., Shuen-De., Yung-Jiun., Cheng-Chung., "Development of a novel embedded relay lens microscopic hyperspectral imaging system for cancer diagnosis: use of the mice with oral cancer to be the example" *International Journal of Spectroscopy*, 2012(1), 710803, 2012.

[10] Huang, K. L., "Relay Lens Design for Image Reduction Applications", *In 2018 1st International Cognitive Cities Conference (IC3)*, 172-173, 2018.

[11] ZEMAX Development Corporation, "ZEMAX Optical Design Program User Guide," 2009.

[12] Keshavarz, A., Soltanzadeh, M. J., "Designing the optimal Fresnel lenses by using Zemax software", *Journal of Optoelectronical Nanostructures*, 3(2), 87-96, 2018.

[13] Sun, J., "Design of long focal length terahertz optical system", *Optical Review*, 31(4), 440-445, 2024.

[14] Saetiew, J., Sanjae, J., Meemon, P., "Real-time assessment of spectrometer alignment using modulation transfer function (MTF) measurement", *Optics and Lasers in Engineering*, 175, 108021, 2024.

[15] Chen, T., Catrysse, P. B., El Gamal, A., Wandell, B. A., "How small should pixel size be*?", In Sensors and Camera Systems for Scientific, Industrial, and Digital Photography Applications*, 3965, 451-459, 2000.

[16] Guyon, O., "Limits of adaptive optics for high-contrast imaging", *The Astrophysical Journal*, 629(1), 592, 2005.

[17] Wu, X., Wang, X., Zhang, J., Yuan, Y., Chen, X., "Design of microcamera for field curvature and distortion correction in monocentric multiscale foveated imaging system", *Optics Communications*, 389, 189-196, 2017.

[18] Tang, L., Hu, C., Xie, K., Cheng, C., Liu, Z., "Optimized design of capsule endoscopy lens based on ZEMAX", *In 2011 IEEE International Conference on Information and Automation,* 57-62, 2011.

Middle East Journal of Science

https://dergipark.org.tr/mejs

MEJS

e-ISSN:2618-6136

Research Article

COMPARATIVE FEATURE SELECTION APPROACHES FOR ALZHEIMER'S DISEASE USING GENETIC ALGORITHMS AND PARTICLE SWARM OPTIMIZATION

Simay TÜRKÜSAY [1], ***Murat OTURAKÇI**** [1], ***Esra EKİNCİ*** [1], ***Deniz TÜRSEL ELİİYİ*** [1]

[1]Department of Industrial Engineering, Faculty of Engineering and Architecture, İzmir Bakırçay University, İzmir, Türkiye

*Corresponding author; murat.oturakci@bakircay.edu.tr

Abstract: *Alzheimer's disease (AD) is the most prevalent form of dementia, significantly impairing cognitive abilities such as memory and judgment. The number of dementia cases is expected to rise dramatically in the coming decades, with Alzheimer's disease accounting for 60-80% of these cases. Early detection is crucial for improving patient outcomes, yet diagnosing Alzheimer's at its early stages remains challenging due to various clinical and perceptual obstacles. This study addresses whether Alzheimer's can be detected in advance and the methods that can be used for early diagnosis. Using an Alzheimer's disease dataset sourced from Kaggle including 2,150 samples with 32 independent and 1 dependent variables, various classification algorithms were applied to assess performance. Feature selection techniques, including both classical and metaheuristic methods (Genetic Algorithm and Particle Swarm Optimization), were then applied to the dataset. These methods helped reduce the dataset's dimensionality while maintaining high diagnostic performance. The results showed that both metaheuristic algorithms selected 14 variables, producing the same high performance rate of 95.57% compared to the initial 32 variables. The findings suggest that Alzheimer's disease can be detected more efficiently with fewer variables, reducing analysis time and increasing diagnostic speed. Metaheuristic algorithms, particularly Particle Swarm Optimization, proved to be the most effective, enhancing the performance of 33 classifiers, while the Genetic Algorithm improved the performance of 28 classifiers. This study demonstrates that Alzheimer's can be detected with fewer variables, in less time, and with a higher accuracy rate. As a result, improved patient outcomes through reduced computational complexity and enhanced diagnostic efficiency can potentially be achieved.*

Keywords*: Alzheimer's Disease; Classification, Feature Selection, Genetic Algorithm, Particle Swarm Optimization*

Received:December 23, 2024 *Accepted: April 21, 2025*

1. Introduction

Dementia is a general medical term for a decline in cognitive function severe enough to interfere with daily activities. Alzheimer's disease (AD) is the most common form of dementia, which occurs at least two-thirds of dementia cases that are aged 65 and over [1]. A neurodegenerative condition, Memory, comprehension, language, attention, thinking, and judgment are among the behavioral and cognitive skills that are gradually compromised by Alzheimer's disease [1].

The World Health Organization (WHO) projects that the number of people with dementia, which is already over 55 million, will increase to 75 million by 2030 and 132 million by 2050[2]. According to studies, 60–80% of dementia cases are attributable to Alzheimer's disease, and a new case is diagnosed every three seconds. In Turkey, 5.5% of people 65 and older have Alzheimer's disease, according to the

2022 Turkey Health Survey Report released by the Turkish Statistical Institute (TÜİK). This emphasizes how urgently Turkey, like the rest of the world, must implement effective measures to battle Alzheimer's disease [2].

Clinicians have now been urged to detect Alzheimer's sooner before individuals have developed dementia from the condition. The ability of clinicians to accurately and early detect the underlying pathology and symptoms of Alzheimer's disease is critical to the screening, diagnosis, and treatment of such individuals. Additionally, it helps patients, and their caregivers create future plans and modify their lifestyles in ways that may help them live longer and maintain a higher quality of life. Unfortunately, several challenges can make it challenging to detect early-stage Alzheimer's disease in clinical practice. These include clinicians' time constraints, the challenge of accurately diagnosing Alzheimer's pathology, and patients' and healthcare professionals' propensity to dismiss symptoms as a normal aspect of aging. [3].

This situation prompts two essential questions:

1. Is it possible to reveal the presence or onset of Alzheimer's disease before symptoms appear?
2. If early detection is feasible, what methods or techniques can be employed to identify the disease?

Motivated by these research questions, this study aims to address them by utilizing a previously measured dataset, applying classification algorithms, and implementing feature selection techniques through classical and metaheuristic methods. The main goal is to facilitate the early diagnosis of the disease and enable the immediate initiation of treatment methods.

In this context, various classification algorithms were applied to a pre-measured dataset, and their performance was evaluated. Subsequently, feature selection was performed on the same dataset using classical and metaheuristic algorithms, specifically genetic algorithm and particle swarm optimization. These algorithms are selected as ideal ones for effectively reducing the dimensionality of medical datasets and eliminating overfitting and computational inefficiency [4]. By optimizing the selection of the most informative variables through these algorithms, the most critical predictors of Alzheimer's disease can be utilized for an accurate and efficient medical diagnosis. Based on the results of each algorithm, datasets tailored to the selected variables were created, and classification algorithms were applied to these datasets again. The performance results obtained were then compared with the initial ones. As a result of the comparison, the classifier and feature selection method that yielded the highest performance were identified. The study concluded that the disease identification process could achieve higher performance with fewer variables than those initially examined in the dataset.

This study provides both theoretical and practical contributions to Alzheimer’s disease. Theoretically, it highlights the effectiveness of combining feature selection with machine learning techniques, demonstrating that fewer but more relevant features can significantly improve classification performance. Practically, the research shows that using metaheuristic algorithms like genetic algorithms and particle swarm optimization for feature selection can enhance diagnostic efficiency, reducing computational complexity while maintaining high accuracy. These findings offer valuable insights for developing more efficient early and cost-effective Alzheimer’s disease in clinical settings. The diagnostic process for this critical disease can possibly be streamlined through faster and more reliable predictions as a result.

The study is organized into several key sections, each addressing a specific aspect of the research process. It begins with a Literature Review, where previous studies and relevant research are examined to provide context and highlight existing gaps in the field. This is followed by the Methods and Materials section, which outlines the research design, data collection techniques, and tools used in the analysis. In the Results section, the findings of the study are presented, including any statistical analyses or observations made during the investigation. Finally, the study concludes with a Conclusion section,

summarizing the key insights, discussing the implications of the findings, and suggesting areas for future research.

2. Literature Review

Within the scope of the literature review, notable studies using feature selection for the detection of Alzheimer's disease between 2014 and 2024 are presented. This study outlines the methods utilized and provides an overview of various studies conducted between 2014 and 2024 that demonstrate the applications of these methods.

Anirudha et al. (2014) present a Genetic Algorithm-based Wrapper feature selection Hybrid Prediction Model (GWHPM) for disease prediction, utilizing k-means clustering to remove outliers and a genetic algorithm for optimal feature selection. These features are then used to build classifier models including Decision Tree, Naïve Bayes, k-nearest neighbor, and Support Vector Machine, with comparative results showing that the proposed GWHPM outperforms existing methods. Mirzaei et al. (2018) aim to develop a non-invasive method for early detection of Alzheimer's disease using voice analysis techniques combined with machine learning algorithms. Neelaveni et al. (2020) apply machine learning algorithms using psychological parameters, including age, number of visits, MMSE scores, and education level, to predict Alzheimer's disease, highlighting the importance of early prediction in mitigating disease progression, despite AD typically being diagnosed in later stages. Saputra et al. (2020) classify Alzheimer's disease using different decision tree algorithms with feature selection through the Particle Swarm Optimization (PSO) algorithm, achieving a 93.56% accuracy after applying PSO-based feature selection to the OASIS 2 dataset. Ramaswamy et al. (2021) identify genes contributing to Alzheimer's disease using gene expression data from the human brain in AD patients and older control subjects, applying a two-step gene selection method that combines statistical techniques and heuristic optimization, with classifiers achieving 100% accuracy on the GSE5281 test dataset. Divya et al. (2021) investigate the classification of Alzheimer's disease, mild cognitive impairment (MCI), and normal control (NC) using MRI images from the ADNI dataset, finding that dimensionality reduction improves classification performance, especially with limited high-dimensional data, and achieving accuracy rates of 96.82%, 89.39%, and 90.40% for NC/AD, NC/MCI, and MCI/AD classifications, respectively. Buyrukoğlu (2021) develops a model for early Alzheimer's disease diagnosis using ensemble feature selection methods, with Random Forest achieving the highest performance at 91% across three target classes: Normal (CN), MCI, and AD. Noroozi et al. (2023) analyze feature selection techniques for heart disease prediction using the Cleveland Heart Disease dataset, showing that feature selection enhances some algorithms (e.g., J48) but diminishes others (e.g., MLP, RF), with the SVM-based filtering method achieving the highest accuracy at 85.5%. Hassouneh et al. (2024) investigate the significance of fused texture features derived from 3D MRI and PET images for the early detection of Alzheimer's disease, finding that GLCM texture features from the hippocampus and entorhinal cortex outperform volume and SUVR features, achieving 90% sensitivity in identifying MCI converters with minimal false positives, and highlighting the role of various feature types in improving classification accuracy for early AD diagnosis.

3. Materials and Methods

3.1. Materials

This study examines an anonymous Alzheimer's disease dataset sourced from the Kaggle platform, which contains high-quality data [13]. The dataset used consists of 33 variables (32 independent and 1 dependent) and 2,150 samples. The independent variables include: "Age, Gender, Ethnicity, Education Level (EL), BMI, Smoking, Alcohol Consumption (AC), Physical Activity (PA),

Diet Quality (DQ), Sleep Quality (SQ), Family History Alzheimers (FHA), Cardiovascular Disease (CD), Diabetes, Depression, Head Injury (HI), Hypertension (HT), SystolicBP (SBP), DiastolicBP(DBP), Cholesterol Total (CT), Cholesterol LDL (LDL), Cholesterol HDL (HDL), Cholesterol Triglycerides (TG), MMSE, Functional Assessment (FA), Memory Complaints (MC), Behavioral Problems (BP), ADL, Confusion (CO), Disorientation (DO), Personality Changes (PC), Difficulty Completing Tasks (DCT), Forgetfulness (FF)", while the dependent variable is "Diagnosis." To ensure accurate measurements and proper numerical interpretation by the algorithms, the values of certain variables, initially presented in numerical categories, were modified following the guidelines provided on the dataset's hosting platform. Specifically: For Gender, values were encoded as 0 for Male and 1 for Female. For Ethnicity, values were encoded as 0 for Caucasian, 1 for African American, 2 for Asian, and 3 for Other. For Education Level, values were encoded as 0 for None, 1 for High School, 2 for Bachelor's, and 3 for Higher. Other categorical variables with binary values were encoded as 0 for No and 1 for Yes. A part of the dataset is presented in Table 1 as an example. While analyzing the model, the data was separated into test (30%) and training (70%). This separation was performed randomly to ensure that both sets of evolutions represented the general distribution.

Table 1. Dataset Sample [13]

Age	Gender	Ethnicity	EL	BMI	Smoking	AC	PA	DQ	SQ	FH
73	0	0	2	22,928	0	13,297	6,327	1,347	9,026	0
89	0	0	0	26,828	0	4,543	7,620	0,519	7,151	0
73	0	3	1	17,796	0	19,555	7,845	1,826	9,674	1
74	1	0	1	33,801	1	12,209	8,428	7,436	8,393	0
89	0	0	0	20,717	0	18,454	6,310	0,795	5,597	0
86	1	2	1	30,627	0	4,140	0,211	1,585	7,262	0
68	0	3	2	38,388	1	0,646	9,258	5,897	5,478	0
75	0	0	1	18,776	0	13,724	4,649	8,342	4,213	0
72	1	1	0	27,833	0	12,168	1,531	6,737	5,748	0
87	0	0	0	35,456	1	16,029	6,441	8,086	7,552	0
CD	**Diabetes**	**Depression**	**HI**	**HT**	**SBP**	**DBP**	**CT**	**LDL**	**HDL**	**TG**
0	1	1	0	0	142	72	242,367	56,151	33,683	162,189
0	0	0	0	0	115	64	231,163	193,408	79,028	294,631
0	0	0	0	0	99	116	284,182	153,323	69,772	83,638
0	0	0	0	0	118	115	159,582	65,367	68,457	277,577
0	0	0	0	0	94	117	237,602	92,870	56,874	291,199
0	1	0	0	0	168	62	280,713	198,335	79,081	263,944
0	0	0	1	0	143	88	263,734	52,471	66,533	216,489
0	0	0	0	0	117	63	151,383	69,624	77,347	210,571
0	0	0	0	1	117	119	233,606	144,046	43,076	151,164
1	0	0	0	0	130	78	281,630	130,498	74,291	144,176
MMSE	**FA**	**MC**	**BP**	**ADL**	**CO**	**DO**	**PC**	**DCT**	**FF**	**Diagnosis**
21,464	6,519	0	0	1,726	0	0	0	1	0	0
20,613	7,119	0	0	2,592	0	0	0	0	1	0
7,356	5,895	0	0	7,120	0	1	0	1	0	0
13,991	8,965	0	1	6,481	0	0	0	0	0	0
13,518	6,045	0	0	0,015	0	0	1	1	0	0
27,518	5,510	0	0	9,016	1	0	0	0	0	0
1,964	6,062	0	0	9,236	0	0	0	0	1	0
10,140	3,401	0	0	4,517	1	0	0	0	1	1
25,821	7,396	0	1	0,756	0	0	1	0	0	0
28,388	1,149	0	1	4,554	0	0	0	0	0	0

3.2. Methods

Classification is known as one of the most widely used data mining methods for predicting group memberships. Classification techniques work on the basis of assigning data points to predefined classes or groups. Many classification methods have different strengths depending on the characteristics of the data set [14]. In addition to basic methods such as decision trees and support vector machines, there are also classification methods with complex structures such as neural networks. In this study, 45 classification algorithms were used according to the suitability of the selected data set structure and the diversity of the algorithms allowed for a comparative evaluation of their performances.

BayesNet: The Bayes theorem is the foundation of BayesNet. Thus, a Bayesian network is created by calculating the conditional probability of each node in BayesNet. A directed acyclic graph is the Bayesian Network. All attributes are assumed to be nominal in BayesNet, and any missing values are replaced globally [15].

NaiveBayes: Because of its robustness, elegance, and simplicity, NaiveBayes is frequently employed for categorization. Navie and Bayes are two ways to describe NavieBayes. When the occurrences are independent and the Bayes rule is applied, Navie, which stands for independence, is true to multiply probability. This method assumes that a class's characteristics are independent in practice. When the data set is real, the NavieBayes perform better [15].

NaiveBayesMultinomialTest: One of the most popular text mining techniques is the Naïve Bayes classifier. Multinomial Naïve Bayes, which is essentially an improved version of the original Naïve Bayes classifier, efficiently manipulates the word count by determining the frequency of each word, whereas in the Naïve Bayes classifier, the frequency of the words has little bearing on how the algorithm operates. It is well recognized that a text's frequency has a greater influence on its classification into several groups. Therefore, Multinomial Naïve Bayes is thought to be the best method for text categorization [16].

NaiveBayesUpdateable: This is the NaiveBayes version that can be updated. When buildClassifier, often referred to as incremental update, is invoked with zero training examples, this classifier will utilize a default precision of 0.1 for numeric attributes [15].

LibSVM: A programming library for SVM is called LibSVM. Researchers utilize it for tasks involving regression and classification. WEKA, which includes a set of machine learning algorithms for data mining, also incorporates LibSVM [17]. ***Logistic:*** Regarding binary classification A lot of people utilize logistic regression. A linear and additive summary of a variable's impact on the logged chances of possessing a characteristic on an event is given by the logistic regression coefficients. In this case, the result is determined by one or more independent variables. There are two possible outcomes: 1 for true and 0 for false. It is employed to shed light on data and explain how one dependent binary variable and one or more independent variables relate to one another [18].

MultiLayerPerceptron: Neural networks and artificial intelligence are unqualified definitions of multilayer perceptrons. A feedforward neural network with one or more layers between the input and output layers is called a multilayer perceptron (MLP) [15].

SGD: An effective technique known as incremental gradient descent is stochastic gradient descent or SGD. Additionally, it is regarded as a stochastic approximation method that proceeds in this direction while decreasing exponentially by averaging previous gradients. Consequently, it is an optimization method with a number of advantages; for instance, it offers both optimal runtime and ideal sample complexity needs [19].

SGDText: To determine the model parameters that best fit the expected and actual outputs, machine learning applications frequently employ the optimization process known as stochastic gradient descent. It's a strong yet imprecise method. This model disregards non-string (text) inputs, which is how it differs from the conventional SGD classifier [20].

SimpleLogistic: The goal of the well-liked statistical analysis method SimpleLogistic is to identify the best linear logistic regression model. With basic regression functions, it is comparable to the LogitBoost approach. This algorithm, which relies on the logistic function, simulates the outcome's log odds rather than the actual result. Additionally, SimpleLogistic describes the connection between one or more independent variables and the category dependent variable [19].

SMO: Sequential Minimal Optimization, or SMO, is an improved technique for SVM training that has demonstrated strong performance across a variety of issues. However, due to its implementation challenges and training complexity, SVM's employment was constrained. Because SMO is conceptually straightforward, simple to implement, and generally faster than SVM, it is thus subtly enhanced [19].

VotedPerception: Voted perceptron methods for analyzing tiny samples and exploiting the most significant margin of data [15].

IBK: IBK, or instance-based k-nearest neighbors, is a straightforward technique that expands on the k-nearest neighbors algorithm by lowering the amount of storage space needed. To effectively categorize target points (unknown class) based on their distances from reference points that make up a training sample in which their class is already known, IBK uses similarity computations between instances, similar to those of KNN [19].

KStar: K-star, sometimes known as K*, is a classifier that is instance-based. A similarity function determines the class of a test instance based on the training examples that are similar to it. It employs an entropy-based distance function, which sets it apart from other instance-based learners. Instance-based learners use a database of previously categorized examples to classify an instance [21].

LWL (Locally Weighted Learning): One of the key algorithms in lazy learning is locally weighted learning (LWL). When a new instance needs to be processed, a weighted set of training instances linked to the test instance is determined by calculating the distance between the training and test instances using a distance function. This weighted set is then used to build a new model to process the new instance. In conventional weighted learning methods, the Euclidean distance is typically utilized to calculate the separation between instances [22].

IterativeClassifierOptimizer: Through the use of cross-validation, the ICO method was developed to maximize the number of iterations in each performance. Numerical, nominal, binary, and empty nominal characteristics are among the missing, nominal, and binary classes that this algorithm can handle with ease [23].

AdaBoostM1: Boosting is the process of making any algorithm perform better. Boosting is mostly used to lessen a poor algorithm's flaws. A powerful classifier is built using this algorithm. It was created to enhance the performance of crucial activities by combining numerous different algorithms [24].

AttributeSelectedClassifier: Before being sent to a classifier, attribute selection lowers the dimensionality of the training and test data [25].

Bagging: One of the first and most straightforward integration techniques with the best results was the Bagging algorithm, which Breiman proposed. The fundamental idea is to employ an original training set and a weak classification algorithm. Classifiers are trained using the learning method over several rounds [22].

ClassificationViaRegression: Regression-based classification is taught in this class. One regression model is constructed for each class value once the classes are binarized [26].

CvParameterSelection: Class for selecting parameters for any classifier using cross-validation [27].

FilteredClassifier: This class is used to run an arbitrary classifier on data that has been filtered arbitrarily. Similar to the classifier, the filter's structure is only determined by the training data, and it processes test examples without altering their structure. The instances and/or attributes are resampled with replacement based on the weights before being provided to the filter or the classifier (as

appropriate) if there are unequal instance weights or attribute weights and the filter or the classifier cannot handle them [28].

LogitBoost: A course for carrying out logistic regression with addition. This class can handle multi-class problems and uses a regression strategy as the basic learner for classification [29].

MultiClassClassifier: A metaclassifier that uses 2-class classifiers to handle multi-class datasets. For improved accuracy, this classifier can additionally apply output codes that fix errors. Before being sent to the base classifier, the data will be resampled with replacement based on the weights if the instance weights are not uniform and the base classifier is unable to handle them [30].

MultiClassClassifierUpdateable: A metaclassifier that uses 2-class classifiers to handle multi-class datasets. For improved accuracy, this classifier can additionally apply output codes that fix errors [31].

MultiScheme: Class for choosing a classifier from a number of them based on performance on the training data or cross validation on the training data. Performance is evaluated using mean-squared error (regression) or percent correct (classification) [32].

RandomCommittee: Using distinct random number seed values, a random committee builds several base classifiers. The average of the predictions produced by each base classifier is used to determine the final classification outcome [33].

RandomizableFilteredClassifier: Using data that has been subjected to an arbitrary filter, this technique applied an arbitrary classifier. Like the classifier, the filter's structure only functioned with the training data; test instances are processed by the filter without having their structure changed [34].

RandomSubspace: With feature space subsampling, this method aims to give students diversity. The same training data is used to build each component model, but each one adds diversity to the ensemble by considering a randomly selected subset of features. Generally speaking, the number of features is set at the same level for every committee component. An ensemble uses either weight voting or majority voting to decide on classification [35].

Stacking: Historically, one of the earliest techniques for ensemble learning was stacking. By using a "meta-learner" (high-level model) that accepts the output values of the base models as inputs, it integrates multiple base models (lower-level models) constructed using completely distinct classes of machine learning techniques [36]. ***Vote:*** Class for classifier combination. There are various combinations of categorization probability estimations available [37].

WeightedInstancesHandlerWrapper: The primary benefit of the WIHW model is that training instances are weighted using a wrapper technique. The WIHW algorithm employs the resampling with weights technique if the basis classifier is not implementing the core. By default, the training dataset is transferred to the base classifier, and it has the ability to control instance weights [38].

InputMappedClassifier: A wrapper classifier that resolves conflicting training and test data by creating a mapping between the structure of the incoming test instances and the training data used to generate the classifier. Both incoming nominal attribute values that the classifier has never seen before and model attributes that are absent from the incoming examples are given missing values. It is possible to load an existing classifier from a file or train a new one [39].

DecisionTable: A significant component of the categorization process is the use of algorithms based on decision trees. Their primary benefits are that they are typically very quick to compute and do not rely on assumptions about the distribution of data [40].

JRip: William W. Cohen suggested Repeated Incremental Pruning to Produce Error Reduction (RIPPER) as an improved version of IREP, and this class implements this propositional rule learner [41].

OneR: OneR, which stands for "One Rule," is a straightforward but precise classification algorithm that choose the rule with the lowest overall error as its "one rule" after producing one rule for each predictor

in the data. We must build a frequency table for every predictor against the target before we can develop a rule for it [42].

PART: In 1998, Eibe Frank and Ian H. Witten developed the partition and regression tree (PART) decision tree algorithm, which employs incomplete decision trees to extract rules from a dataset [22].

ZeroR: Most classes in training data are predicted by the ZeroR classifier. It forecasts the mode for nominal class and the mean for numerical values [43].

DecisionStump: One-level decision trees make up a Decision Stump, a type of machine learning model. That is, it is a decision tree with a single internal node (the root) that is directly linked to the leaves, which are the terminal nodes. Only one input feature's value is used by a decision stump to produce a prediction [44].

HoeffdingTree: An method called the Hoeffding Tree is used to create decision trees from data that increases gradually. The Hoeffding Tree implies that the distribution of data does not change over time and operates with massive streams of data. The Hoeffding bound, which calculates the number of samples required to evaluate some valuable information within a required correctness, is the foundation of the Hoeffding Tree [45].

J48: The decision tree is J48's output. The root, intermediate, and leaf nodes of a tree structure are comparable to those of a decision tree. Every node in the tree has a decision, and our outcome is the effect of that decision. A data set's input space is divided into mutually exclusive sections by decision trees, and each section's data points are described by a label, value, or action. The optimum attribute to split the training data section tree that reaches a specific node is determined using the splitting criterion [15].

LMT (Logistic Model Trees): A decision tree induction and logistic regression (LR) model were combined to create the new supervised learning model known as LMT (logistic model tree), which combines the two classification algorithms to benefit from both approaches [19].

RandomForest: A collaborative learning system for regression, classification, and other tasks, random decision forests are run by formatively generating a large number of decision trees during training. For decision trees that are overly appropriate for their instruction set, random decision forests are suitable. The stated training error is an unbiased estimator cross-validated error rate, which is one of Random Forest's key characteristics [18].

RandomTree: A decision tree based on a random subset of qualities is called a random tree. A collection of nodes and their branches is called a decision tree. A decision tree's node denotes an attribute test, and each branch shows the result of that test. A decision tree's leaves represent the ultimate choice made after calculating each attribute as class labels. A classification rule is formed by the route taken from a root to a leaf [33].

RepTree: A quick decision tree learner is the REP Tree (reduced error pruning tree) algorithm. Information gain and variance are used to construct a decision/regression tree, which is then pruned using reduced-error pruning (with back-fitting). For numeric attributes, the method sorts the data only once. The related instances are divided into pieces in order to handle missing values [46].

One of the most common and significant methods in data preprocessing is feature selection, which is now an essential part of the machine learning procedure. In statistics and machine learning, it is sometimes referred to as variable selection, attribute selection, or variable subset selection. It involves finding pertinent traits and eliminating data that is superfluous, redundant, or noisy. This procedure promotes comprehensibility, boosts predictive accuracy, and expedites data mining techniques [47].

As part of the study, feature selection was performed using three types of algorithms. The first was the CfsSubsetEval algorithm, while the other two were meta-heuristic algorithms: the Genetic Algorithm and the Particle Swarm Optimization Algorithm.

CfsSubsetEval: It assesses the value of a subset of features by taking into account each feature's predictive power on its own as well as the level of overlap between them [48]. ***Genetic Algorithms:*** Natural selection is the focus of optimization techniques known as genetic algorithms. GAs were first proposed by John Holland, who used them to explain how natural systems adapt and to create new artificial structures based on the same ideas. This starts with artificial individuals (represented by a "chromosome" population) and mimics the process of natural selection. GA uses genetic operators (e.g., crossover and mutation) to try to enhance the fitters. Furthermore, it aims to develop chromosomes that are stronger than those of their parents in a specific quantitative metric. As a result, GA has been a popular method for data mining feature selection in recent years [49]. ***Particle Swarm Optimization:*** Kennedy and Eberhart introduced PSO, an evolutionary computation method, in 1995. Fish schools and flocks of birds are examples of social behaviors that drive PSO. The fundamental idea behind PSO is that social contact maximizes knowledge in a population where social and personal thinking coexist. The foundation of PSO is the idea that every solution can be thought of as a particle in a swarm. [50]

The workflow of the study, based on the provided information, is shown in Figure 1.

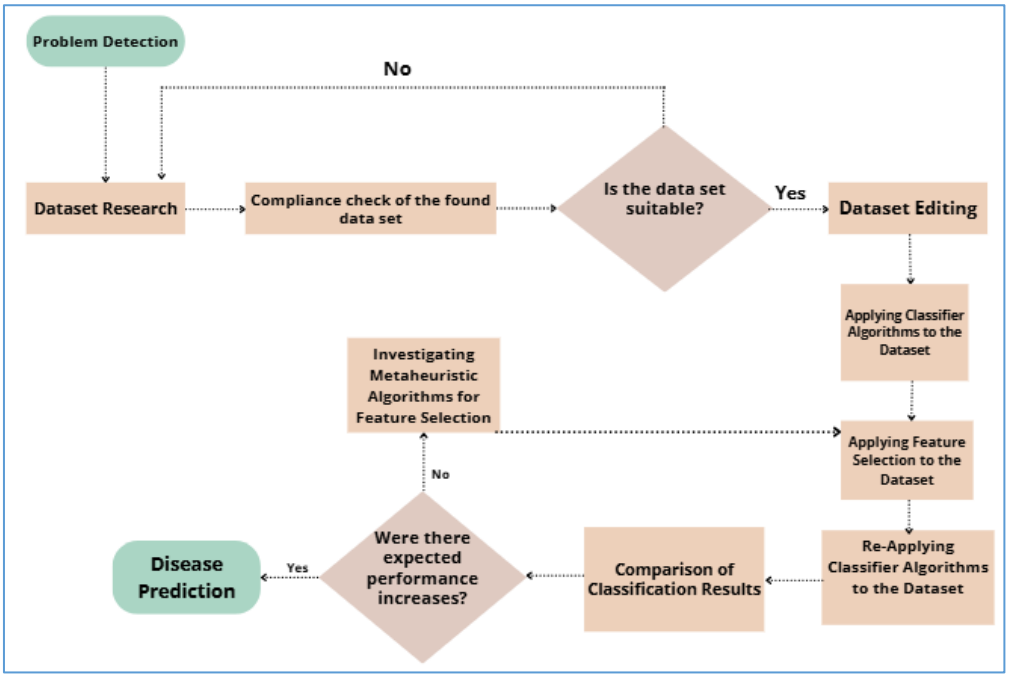

Figure 1. Workflow of the Study

4. Findings and Discussion

As the first step, selected classification algorithms were applied to the dataset, and their performance was evaluated with Weka Software. Subsequently, feature selection was performed on the dataset using CfsSubsetEval, to identify variables that significantly influence the disease. Using the CfsSubsetEval algorithm, 6 out of 32 independent variables were selected. These variables are "Family History Alzheimer's, Hypertension, Functional Assessment, Memory Complaints, Behavioral Problems, ADL." A new dataset was created with 6 independent variables and 1 dependent variable, and classification algorithms were run again. The performance results were compared to the previous (before feature selection) results. According to the performance results obtained, it was found that the CfsSubsetEval feature selection algorithm did not contribute to performance improvement. Results are

provided in Table 2. The models performed consistently across training and test sets during the experiments, indicating no significant overfitting was observed.

Table 2. Comparative Results for Feature Selection

Classifier	Before Feature Selection	After Feature Selection	Classifier	Before Feature Selection	After Feature Selection
	Performance (%)	Performance (%)		Performance (%)	Performance (%)
BayesNet	93.39	84.03	MultiClass Classifier	83.71	81.10
NaiveBayes	84.83	80.40	MultiClass Classifier Updateable	83.38	80.87
Naive Bayes Multinominal Text	64.63	64.63	MultiScheme	64.63	64.63
NaiveBayes Updateable	84.83	80.40	Random Committee	92.41	82.41
LibSVM	64.63	85.38	Randomizable Filtered Classifier	56.95	77.85
Logistic	83.71	81.10	Random SubSpace	88.27	78.82
Multilayer Perceptron	82.41	86.41	Stacking	64.63	64.63
SGD	83.38	80.87	Vote	64.63	64.63
SGD Text	64.63	64.63	Weighted Instances Handler Wrapper	64.63	64.63
Simple Logistic	84.13	81.01	InputMapped Classifier	64.63	64.63
SMO	83.62	81.52	DecisionTable	95.57	87.85
Voted Perceptron	64.63	77.10	JRip	94.74	86.87
IBk	65.28	79.71	OneR	65.33	65.33
KStar	68.86	83.01	PART	90.27	86.73
LWL	69.61	80.40	ZeroR	64.63	64.63
Iterative Classifier Optimizer	94.74	86.87	DecisionStump	69.84	69.84
AdaBoostM1	93.90	85.01	HoeffdingTree	84.83	80.40
Attribute Selected Classifier	93.85	86.92	J48	94.88	86.92
Bagging	95.16	86.45	LMT	93.67	86.78
Classification Via Regression	93.25	87.24	RandomForest	94.69	84.69
CV Parameter Selection	64.63	64.63	RandomTree	80.64	79.85
Filtered Classifier	95.57	87.85	REPTree	94.69	87.01
LogitBoost	94.74	86.55			

As a next step of the study, two metaheuristic algorithms that are suitable for the existing dataset were selected and applied. These algorithms are the Genetic Algorithm and Particle Swarm Optimization algorithm. These algorithms were implemented and executed using the Python programming language. Using the Genetic Algorithm implemented in the Python programming language, 14 out of 32 independent variables were selected. These variables are "Ethnicity, Education Level, Physical Activity, Family History Alzheimer's, Diabetes, Cholesterol Total, Cholesterol Triglycerides, MMSE, Functional Assessment, Memory Complaints, Behavioral Problems, ADL, Personality Changes, Difficulty

Completing Tasks". A new dataset was created with 14 independent variables and 1 dependent variable, and classification algorithms were run again. Results are presented in Table 3. The models performed consistently across training and test sets during the experiments, indicating no significant overfitting was observed.

Using the Particle Swarm Optimization implemented in the Python programming language, 14 out of 32 independent variables were selected. These variables are "Ethnicity, Education Level, BMI, Diet Quality, Family History Alzheimer's, Cardiovascular Disease, Diabetes, Cholesterol LDL, MMSE, Functional Assessment, Memory Complaints, Behavioral Problems, ADL, Forgetfulness". The classification algorithms were rerun using a fresh dataset that contained one dependent variable and fourteen independent variables. Results are presented in Table 3.

According to the obtained performance results, the highest performance rate of 95.57%, achieved before feature selection, remained unchanged after feature selection using the Genetic Algorithm and Particle Swarm Optimization, continuing to be the highest performance rate. This suggests that not all 32 variables in the Alzheimer's disease dataset are necessary, and only 14 of them may be sufficient to diagnose the disease. As a result, the time required for diagnosis is reduced, and the analysis speed is increased.

When comparing the Genetic Algorithm and Particle Swarm Optimization, both being meta-heuristic algorithms, it is necessary to make comparisons based on other performance rates since they provided the highest and identical performance rates. The Genetic Algorithm improved the performance of a total of 28 classifier algorithms, while the Particle Swarm Optimization algorithm improved the performance of a total of 33 classifier algorithms. Therefore, the algorithm that had the most significant impact on the dataset's performance is the Particle Swarm Optimization algorithm.

After applying Genetic Algorithms (GA) for feature selection, many classifiers show noticeable improvements in performance. For instance, the "RandomCommittee" classifier increases its accuracy from 92.41% (before feature selection) to 94.18% with GA, while "RandomForest" jumps from 94.69% to 95.39%. Similarly, "J48" also improves, reaching 95.11% after GA, compared to 94.88% before. These improvements suggest that Genetic Algorithms are particularly effective in enhancing the performance of more complex models, such as ensemble classifiers (e.g., Bagging, RandomForest), by optimizing the feature set.

On the other hand, Particle Swarm Optimization (PSO) generally shows similar or slightly better results compared to GA. In many cases, classifiers like "J48" and "Bagging" show no significant difference in performance with PSO, remaining close to their high pre-selection accuracy levels. However, classifiers like "RandomTree" and "KStar" perform slightly better with PSO than with GA, indicating that PSO may offer more suitable feature selection for certain models.

Table 3. Comparative Results of Genetic Algorithm and Particle Swarm Optimization Performances

Classifier	**Genetic Algorithm**	**Particle Swarm Optimization**	**Classifier**	**Genetic Algorithm**	**Particle Swarm Optimization**
	Performance (%)	**Performance (%)**		**Performance (%)**	**Performance (%)**
BayesNet	93.85	93.90	MultiClass Classifier	84.03	83.94
NaiveBayes	85.34	84.96	MultiClass Classifier Updateable	83.43	84.13
Naive Bayes Multinominal Text	64.63	64.63	MultiScheme	64.63	64.63
NaiveBayes Updateable	85.34	84.96	Random Committee	94.18	93.81
LibSVM	64.77	71.19	Randomizable Filtered Classifier	65.05	67.89

Table 3. Continued.

Classifier	Genetic Algorithm	Particle Swarm Optimization	Classifier	Genetic Algorithm	Particle Swarm Optimization
	Performance (%)	Performance (%)		Performance (%)	Performance (%)
Logistic	84.03	83.94	Random SubSpace	88.69	87.48
Multilayer Perceptron	85.57	84.69	Stacking	64.63	64.63
SGD	83.43	84.13	Vote	64.63	64.63
SGD Text	64.63	64.63	Weighted Instances Handler Wrapper	64.63	64.63
Simple Logistic	83.99	84.36	InputMapped Classifier	64.63	64.63
SMO	83.89	83.66	DecisionTable	95.57	95.57
Voted Perceptron	64.63	70.03	JRip	94.88	94.83
IBk	73.89	71.47	OneR	65.33	65.33
KStar	80.78	77.66	PART	92.55	91.67
LWL	70.03	69.93	ZeroR	64.63	64.63
Iterative Classifier Optimizer	94.74	94.74	DecisionStump	69.84	69.84
AdaBoostM1	93.90	93.90	HoeffdingTree	85.34	84.96
Attribute Selected Classifier	93.85	93.85	J48	95.11	95.16
Bagging	95.16	95.20	LMT	94.18	93.99
Classification Via Regression	94.64	94.32	RandomForest	95.39	95.20
CV Parameter Selection	64.63	64.63	RandomTree	85.24	86.83
Filtered Classifier	95.57	95.57	REPTree	94.88	94.83
LogitBoost	94.74	94.74			

Table 4 summarizes the impact of the feature selection methods on our highest performing classifiers.

Table 4. Highest performance classifiers and the impact of feature selection methods on their performance.

Classifier	Performance Before Feature Selection (%)	CfsSubsetEval (%)	Genetic Algorithm (%)	Particle Swarm Optimization (%)
FilteredClassifier	95.57	87.85	95.57	95.57
Bagging	95.16	86.45	95.20	95.20
RandomForest	94.69	84.69	95.39	95.20
J48	94.88	86.92	95.11	95.16
DecisionTable	95.57	87.85	95.57	95.57
JRip	94.74	86.87	94.88	94.83
RandomTree	80.64	79.85	85.24	86.83
KStar	68.86	83.01	80.78	77.66
MultilayerPerceptron	82.41	86.41	85.57	84.69

As can be seen from Table 4, the classifiers *FilteredClassifier*, *DecisionTable*, and *Bagging* achieved performances of over 95% after feature selection, using both GA and PSO. These classifiers maintained their performance even after reducing the number of features from 32 to 14. Though *CfsSubsetEval* resulted in a performance decrease for most of the classifiers in Table 4, coupling it with GA and PSO maintained or slightly improved performance. For example, the table clearly reveals that *RandomForest* improved from 94.69% to 95.39% with GA, and to 95.20% with PSO. *RandomTree* also showed a significant improvement with PSO, increasing its performance from 80.64% to 86.83%.

Rabie El Kharoua's Alzheimer's Disease dataset has been employed in several articles. Suñé (2025) [52] used classical machine learning techniques such as K-Nearest Neighbors (KNN), Logistic Regression, Support Vector Machines, Neural Networks, Decision Trees, and Random Forest, reporting the highest accuracy of 93.49% with the Decision Tree classifier. In another recent study, Patel et al. (2025) [53] experimented with several classifiers, including Logistic Regression, SVM, Decision Tree, Random Forest, and ANN. After testing across six different feature selection scenarios, they achieved the best result of 95% accuracy with Random Forest using selected numerical and categorical features. Sendhil et al. (2025) [54] compared SVM, GBM, Logistic Regression, KNN, and Random Forest using the same dataset, with Random Forest again performing best at 92% accuracy. Jevin & Umamageswari (2024) [55] applied a deep learning approach using a ABO-2layer CNN and achieved 94.56% accuracy, emphasizing the importance of hybrid deep learning models in medical prediction tasks. Airlangga (2024) [56] evaluated three deep learning architectures—MLP, CNN, and LSTM—on the dataset derived from the same source and found CNN to outperform others with an 88.65% average accuracy. Compared to these studies, our approach achieved a maximum accuracy of 95.57% using only 14 features selected via metaheuristic algorithms (Genetic Algorithm and Particle Swarm Optimization). This not only surpasses most prior studies in predictive accuracy but also demonstrates greater efficiency by reducing model complexity and dimensionality.

The findings of this study could be translated into clinical practice by streamlining diagnostic workflows in hospitals using a reduced feature set. By identifying the most relevant features, the diagnostic process could become faster, more cost-effective, and less resource-intensive, as fewer tests or measurements would be required.

Overall, both GA and PSO contribute to improved classification performance, but PSO seems to give a slight edge in some cases, particularly for classifiers that initially have lower performance. Overall, the best results are achieved with Bagging and FilteredClassifier, both reaching near 95% accuracy, with Particle Swarm Optimization providing the slight edge in enhancing their performance even further. In this case, it has been demonstrated that better results are achieved by selecting only the relevant features, as the classifiers perform more efficiently with the optimized feature sets. Since the best results were obtained with PSO, the selected and unselected features are visualized and presented below. Figure 2 illustrates a visual of the features selected in the PSO algorithm that gave the best result after applying Filtered Classifier with 14 features. Selected features have been illustrated with green and unselected features have been illustrated with blue color.

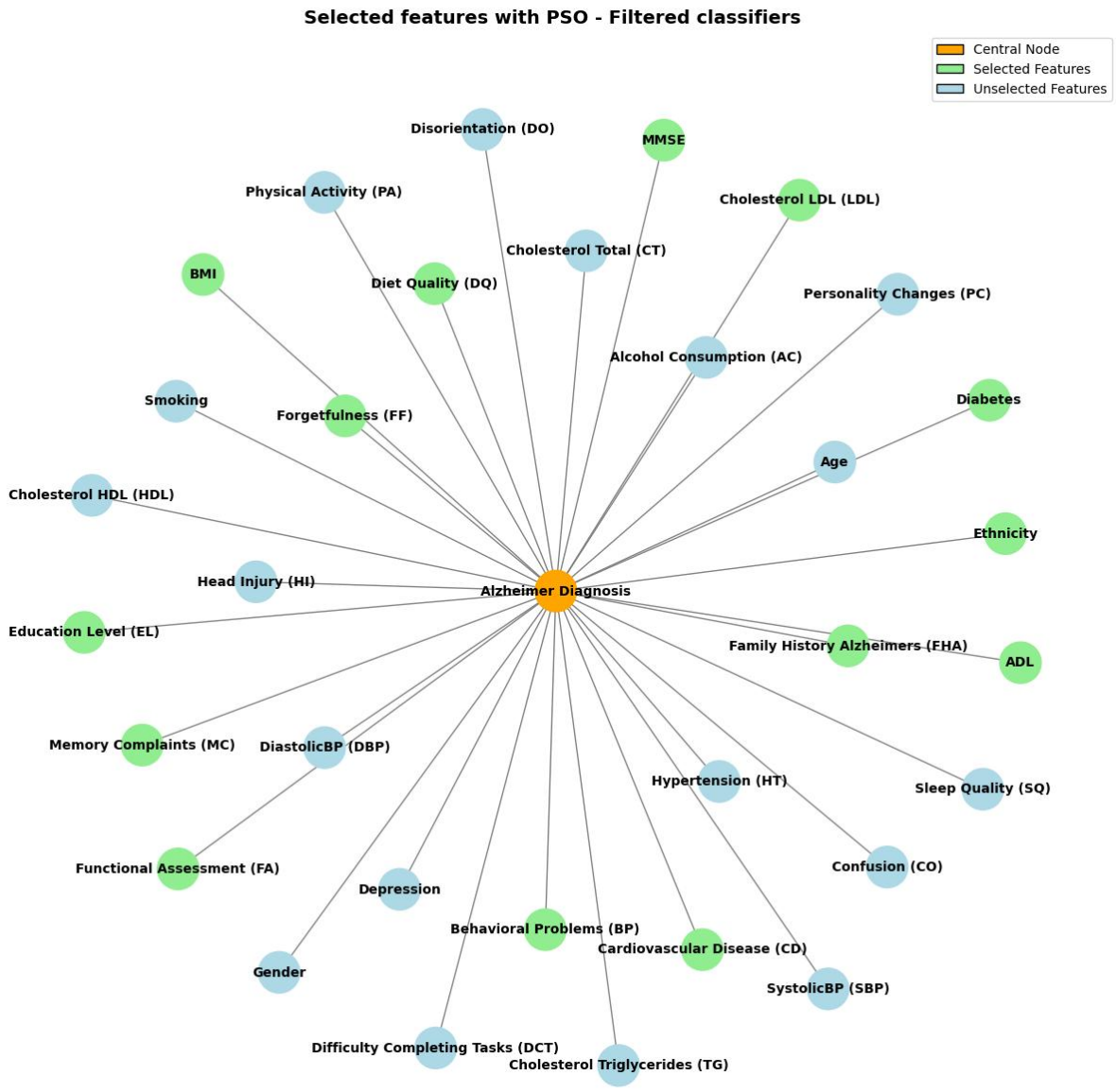

Figure 2. Selected features with best performance in diagnosis.

5. Conclusion

The aim of the study was to reduce the identification and data analysis time by selecting the minimum number of variables required for the diagnosis of Alzheimer's disease, which, if not detected early, can negatively impact individuals' life trajectories and ultimately lead to death in the final stage. This approach also aims to enable the disease to be identified at the earliest possible stage.

In this study, a dataset containing 32 independent and 1 dependent variable, previously measured, was utilized. Then to reduce the number of variables in the dataset, to perform a performance comparison, the dataset was first run with 45 classifier algorithms, and performance results were obtained. Subsequently, CfsSubsetEval, was selected for feature selection and applied to the dataset. As a result of this application, a new dataset was created with 6 independent and 1 dependent variable, and this dataset was again run with 45 classifier algorithms.

Due to a significant drop in performance, it was decided to perform feature selection using meta-heuristic algorithms, considering previous studies. The Genetic Algorithms and Particle Swarm

Optimization algorithms were used to perform feature selection on the dataset in Python programming language. Although they are different from each other, both algorithms selected 14 independent and 1 dependent variable. Based on the selection of both algorithms, datasets were created and each was run again with 45 classifier algorithms. Finally, the results were compared. The highest performance rate before feature selection was 95.57%. After feature selection, both the Genetic Algorithms and Particle Swarm Optimization produced the same highest rate of 95.57%. This indicates that to achieve the highest performance, 14 variables, not 32, are sufficient. Since both algorithms produced the same rate, it is important to consider the increases in performance in other classifier algorithms. The Genetic Algorithms resulted in a performance increase in 28 classifiers, while Particle Swarm Optimization resulted in a performance increase in 33 classifiers. Therefore, it can be said that the best result for the dataset was provided by Particle Swarm Optimization. This study demonstrates that the disease can be detected more quickly and accurately with fewer variables, as the highest performance is achieved with 14 variables instead of 32.

Based on the results of our study, there could be several recommendations for future work and limitations to consider. Future research can focus on testing the proposed approach on larger and more diverse datasets to ensure generalizability and robustness across different populations. For this reason, future studies are planned to compare the results obtained with the ready-made dataset by collecting a real-world dataset. Additionally, exploring other metaheuristic algorithms, such as Ant Colony Optimization or Simulated Annealing, could provide a further insight into the effectiveness of alternative feature selection methods. Despite its promising findings, this study is limited by its reliance on a single dataset, which may not fully capture the variability present in real-world scenarios. Addressing this limitation in future research will help strengthen the applicability and reliability of the proposed methods in clinical practice. Finally, investigating the impact of feature selection on real-time clinical applications, such as integrating these methods into diagnostic tools or wearable devices, would also provide an invaluable future research direction.

Ethical statement

The data is sourced from an open-access database, so there is no need for an ethics committee's evaluation.

Acknowledgment

We are grateful to the anonymous referees for substantial suggestions that improved the quality of our study.

Conflict of interest

The authors declare no competing interests.

Authors' Contributions

S. Turkusay: Software, Formal analysis, Data curation, Writing-original draft. M. Oturakci, E. Ekinci, D. T. Eliiyi: Supervision, Conceptualization, Methodology, Writing - review & editing.

Generative AI statement

The author(s) declare that no Gen AI was used in the creation of this manuscript.

References

[1] Kumar, A., Sidhu, J., Goyal, A., Tsao, J. W., "Alzheimer disease", *StatPearls*, StatPearls Publishing, 2023.

[2] T.C. Sağlık Bakanlığı, "Dünya Alzheimer Günü", 21 Eylül 2024 [Online]. Available: https://hsgm.saglik.gov.tr/tr/haberler-16/21-eylul-2024-dunya-alzheimer-gunu.html

[3] Porsteinsson, A. P., Isaacson, R. S., Knox, S., Sabbagh, M. N., Rubino, I., "Diagnosis of early Alzheimer's disease: clinical practice in 2021", *The journal of prevention of Alzheimer's disease*, 8, 371-386, 2021.

[4] Ding, Y., Zhou, K., Bi, W., "Feature selection based on hybridization of genetic algorithm and competitive swarm optimizer", *Soft Computing*, 24, 11663–11672, 2020.

[5] Anirudha, R. C., Kannan, R., Patil, N., "Genetic algorithm-based wrapper feature selection on hybrid prediction model for analysis of high-dimensional data", *Proceeding of 9th International Conference on Industrial and Information Systems (ICIIS)*, IEEE, pp. 1–6, 2014.

[6] Mirzaei, S., et al., "Two-stage feature selection of voice parameters for early Alzheimer's disease prediction", *IRBM*, 39(6), 430–435, 2018.

[7] Neelaveni, J., Devasana, M. S. G., "Alzheimer disease prediction using machine learning algorithms", *Proceeding of 6th International Conference on Advanced Computing and Communication Systems (ICACCS)*, IEEE, pp. 101–104, 2020.

[8] Saputra, R. A., et al., "Detecting Alzheimer's disease by the decision tree methods based on particle swarm optimization", *Journal of Physics: Conference Series*, IOP Publishing, 012025, 2020.

[9] Ramaswamy, R., Kandhasamy, P., Palaniswamy, S., "Feature selection for Alzheimer's gene expression data using modified binary particle swarm optimization", *IETE Journal of Research*, 69(1), 9–20, 2023.

[10] Divya, R., Shantha Selva Kumari, R., Alzheimer's Disease Neuroimaging Initiative, "Genetic algorithm with logistic regression feature selection for Alzheimer's disease classification", *Neural Computing and Applications*, 33(14), 8435–8444, 2021.

[11] Buyrukoğlu, S., "Early detection of Alzheimer's disease using data mining: Comparison of ensemble feature selection approaches", *Konya Journal of Engineering Sciences*, 9(1), 50–61, 2021.

[12] Noroozi, Z., Orooji, A., Erfannia, L., "Analyzing the impact of feature selection methods on machine learning algorithms for heart disease prediction", *Scientific Reports*, 13(1), 22588, 2023.

[13] Hassouneh, A., et al., "Feature importance analysis and machine learning for Alzheimer's disease early detection: Feature fusion of the hippocampus, entorhinal cortex, and standardized uptake value ratio", *Digital Biomarkers*, 8(1), 59–74, 2024.

[14] Kaggle, "Alzheimer's Disease Dataset" [Online]. Available: https://www.kaggle.com/datasets/rabieelkharoua/alzheimers-disease-dataset?select=alzheimers_disease_data.csv

[15] Soofi, Aized Amin, Awan, Arshad, "Classification techniques in machine learning: applications and issues", *Journal of Basic & Applied Sciences*, 13, 459–465, 2017.

[16] Sahoo, G., Kumar, Yugal, "Analysis of parametric & non parametric classifiers for classification technique using WEKA", *International Journal of Information Technology and Computer Science (IJITCS)*, 4(7), 43, 2012.

[17] Surya, P. P., Seetha, L. V., Subbulakshmi, B., "Analysis of user emotions and opinion using multinomial naive Bayes classifier", *Proceeding of 3rd International Conference on Electronics, Communication and Aerospace Technology (ICECA)*, IEEE, pp. 410–415, 2019.

[18] Abdiansah, A., Wardoyo, R., "Time complexity analysis of support vector machines (SVM) in LibSVM", *International Journal of Computer Applications*, 128(3), 28–34, 2015.

[19] Bharati, S., Rahman, M. A., Podder, P., "Breast cancer prediction applying different classification algorithms with comparative analysis using WEKA", *Proceeding of 4th International Conference on Electrical Engineering and Information & Communication Technology (iCEEiCT)*, IEEE, pp. 581–584, 2018.

[20] Alaoui, S. S., Farhaoui, Y., Aksasse, B., "Classification algorithms in data mining", *International Journal of Tomography & Simulations*, 31(4), 34–44, 2018.

[21] Stupka, R. J., et al., "Exploring attribute selection and classification methods for predicting heart disease", *Proceeding of International Conference on Computational Science and Computational Intelligence (CSCI)*, IEEE, pp. 701–706, 2022.

[22] Mahmood, D. Y., Hussein, M. A., "Intrusion detection system based on K-star classifier and feature set reduction", *IOSR Journal of Computer Engineering (IOSR-JCE)*, 15(5), 107–112, 2013.

[23] Dou, Y., Meng, W., "Comparative analysis of WEKA-based classification algorithms on medical diagnosis datasets", *Technology and Health Care*, 31(S1), 397–408, 2023.

[24] Khosravi, K., et al., "Predictive modeling of selected trace elements in groundwater using hybrid algorithms of iterative classifier optimizer", *Journal of Contaminant Hydrology*, 242, 103849, 2021.

[25] Thilagaraj, T., Sengottaiyan, N., "Implementation of classification algorithms in educational data using WEKA tool", *International Journal of Computer Sciences and Engineering*, 7(5), 1254–1257, 2019.

[26] WEKA SourceForge, "AttributeSelectedClassifier" [Online]. Available: https://weka.sourceforge.io/doc.dev/weka/classifiers/meta/AttributeSelectedClassifier.html

[27] WEKA SourceForge, "ClassificationViaRegression" [Online]. Available: https://weka.sourceforge.io/doc.dev/weka/classifiers/meta/ClassificationViaRegression.html

[28] WEKA SourceForge, "CVParameterSelection" [Online]. Available: https://weka.sourceforge.io/doc.dev/weka/classifiers/meta/CVParameterSelection.html

[29] WEKA SourceForge, "FilteredClassifier" [Online]. Available: https://weka.sourceforge.io/doc.dev/weka/classifiers/meta/FilteredClassifier.html

[30] WEKA SourceForge, "LogitBoost" [Online]. Available: https://weka.sourceforge.io/doc.dev/weka/classifiers/meta/LogitBoost.html

[31] WEKA SourceForge, "MultiClassClassifier" [Online]. Available: https://weka.sourceforge.io/doc.dev/weka/classifiers/meta/MultiClassClassifier.html

[32] WEKA SourceForge, "MultiClassClassifierUpdateable" [Online]. Available: https://weka.sourceforge.io/doc.dev/weka/classifiers/meta/MultiClassClassifierUpdateable.html

[33] WEKA SourceForge, "MultiScheme" [Online]. Available: https://weka.sourceforge.io/doc.dev/weka/classifiers/meta/MultiScheme.html

[34] Niranjan, A., et al., "ERCR TV: Ensemble of random committee and random tree for efficient anomaly classification using voting", *Proceeding of 3rd International Conference for Convergence in Technology (I2CT)*, IEEE, pp. 1–5, 2018.

[35] Asaju, L. B., et al., "Intrusion detection system on a computer network using an ensemble of randomizable filtered classifier, K-nearest neighbor algorithm", *FUW Trends in Science & Technology Journal*, 2(1), 550–553, 2017.

[36] Lasota, T., Łuczak, T., Trawiński, B., "Investigation of random subspace and random forest methods applied to property valuation data", in: *Computational Collective Intelligence. Technologies and Applications* (Ed. N.T. Nguyen et al.), Berlin, Springer Berlin Heidelberg, 2011, ch.3, pp. 142–151.

[37] Baskin, I. I., Marcou, G., Horvath, D., Varnek, A., "Cross-Validation and the Variable Selection Bias", in: *Tutorials in Chemoinformatics* (Ed. A. Varnek), Chichester, John Wiley & Sons, 2017, ch.10, pp. 163–173.

[38] WEKA SourceForge, "Vote" [Online]. Available: https://weka.sourceforge.io/doc.dev/weka/classifiers/meta/Vote.html

[39] Kargar, K., Safari, M. J. S., Khosravi, K., "Weighted instances handler wrapper and rotation forest-based hybrid algorithms for sediment transport modeling", *Journal of Hydrology*, 598, 126452, 2021.

[40] WEKA SourceForge, "InputMappedClassifier" [Online]. Available: https://weka.sourceforge.io/doc.dev/weka/classifiers/misc/InputMappedClassifier.html

[41] Jankovic, R., "Classifying cultural heritage images by using decision tree classifiers in WEKA", Proceeding of 1st International Workshop on Visual Pattern Extraction and Recognition for Cultural Heritage Understanding Co-located with 15th Italian Research Conference on Digital Libraries (IRCDL 2019), Pisa, Italy, pp. 119–127, 2019.

[42] WEKA SourceForge, "JRip" [Online]. Available: https://weka.sourceforge.io/doc.dev/weka/classifiers/rules/JRip.html

[43] Nasa, C., Suman, S., "Evaluation of different classification techniques for web data", *International Journal of Computer Applications*, 52(9), 34–40, 2012.

[44] Aher, S. B., Lobo, L. M. R. J., "Data mining in educational system using WEKA", *Proceeding of International Conference on Emerging Technology Trends (ICETT)*, Foundation of Computer Science, pp. 20–25, 2011.

[45] Kawelah, W., Abdala, A., "A comparative study on machine learning tools using WEKA and RapidMiner with classifier algorithms C4.5 and decision stump for network intrusion detection", *European Academic Research*, 7(2), 852–861, 2019.

[46] Lavanya, K., et al., "Handwritten digit recognition using Hoeffding tree, decision tree and random forests—a comparative approach", *Proceeding of International Conference on Computational Intelligence in Data Science (ICCIDS)*, IEEE, pp. 1–6, 2017.

[47] Rajalakshmi, A., Vinodhini, R., Bibi, K. F., "Data discretization technique using WEKA tool", *International Journal of Science, Engineering and Computer Technology*, 6(8), 293, 2016.

[48] Kumar, V., Minz, S., "Feature selection", *SmartCR*, 4(3), 211–229, 2014.

[49] Velmurugan, T., Anuradha, C., "Performance evaluation of feature selection algorithms in educational data mining", *Performance Evaluation*, 5(2), 92–106, 2016.

[50] Rostami, M., Berahmand, K., Forouzanadeh, S., "A novel community detection-based genetic algorithm for feature selection", *Journal of Big Data*, 8(1), 2, 2021.

[51] Xue, B., Zhang, M., Browne, W. N., "Particle swarm optimization for feature selection in classification: A multi-objective approach", *IEEE Transactions on Cybernetics*, 43(6), 1656–1671, 2012.

[52] Suñé, F. G., "Machine learning techniques for Alzheimer prediction", Master's thesis, Universitat de Barcelona, 2025.

[53] Patel, P., Patel, K., Thakkar, K., Goel, P., Valani, P., Vadhavana, V., "Alzheimer's disease detection using various machine learning algorithms", *Proceeding of 6th International Conference on Mobile Computing and Sustainable Informatics (ICMCSI-2025)*, IEEE, pp. 1048–1054, 2025.

[54] Sendhil, R., Patibandha, N., Shah, P., Mandal, A., "Comparative Evaluation of Machine Learning Techniques for Early Alzheimer's Detection: Challenges and Insights", *Proceeding of International Conference on Multi-Agent Systems for Collaborative Intelligence (ICMSCI)*, IEEE, pp. 1050–1058, 2025.

[55] Jevin, J. A., Umamageswari, A., "Alzheimer's Disease Prediction using an Artificial Butterfly Optimizer with a Two-Layer CNN Approach", *Proceeding of 4th International Conference on Mobile Networks and Wireless Communications (ICMNWC)*, IEEE, pp. 1–6, December 2024.

[56] Airlangga, G., "Advancing Alzheimer's Diagnosis: A Comparative Analysis of Deep Learning Architectures on Multidimensional Health Data", *Jurnal Informatika Ekonomi Bisnis*, pp. 810–814, 2024.

Middle East Journal of Science

https://dergipark.org.tr/mejs

MEJS

e-ISSN:2618-6136

Research Article

THE EFFECT OF DIFFERENT INSULATION MATERIAL ON THERMAL COMFORT IN A BUILDING WITH NOZZLES COOLING SYSTEM

***Ali Çağlar KASIMOĞLU*[1], *Celal KISTAK**[*1], *Haydar EREN*[1]

[1]Fırat University Faculty of Engineering Mechanical Engineering, 23119 Elazığ/Türkiye
[*] Corresponding author; ckistak@firat.edu.tr

Abstract: *A global analysis of energy consumption reveals a downward trend in capacity, while energy demand continues to increase in response to population growth. In this context, the significance of efficient energy utilization, particularly the reduction of heat losses in buildings, has grown considerably. Insulating buildings is a strategy that has the potential to minimize heat loss during winter months and overheating during summer months. This, in turn, can reduce the energy needed for heating and cooling systems, including air conditioners. The present study investigates the impact of insulation on thermal performance using a small, single-story wooden building model. The experimental design involved the insulation of the model's exterior walls with three distinct types of materials during the summer months. The experimenters recorded indoor and outdoor temperatures and calculated total heat loss (or gain) to assess the effects of insulation material on thermal comfort. The experiments were repeated with different building orientations, while radiation intensity and wind speed were also measured for a comprehensive analysis.*

Keywords: *Energy, Insulation, Thermal Performance, Heat Transfer*

Received: January 17, 2025 *Accepted: May 24, 2025*

1. Introduction

Energy is among the fundamental necessities of modern societies, playing a critical role in economic growth and societal well-being. Factors such as population growth, industrialization, and urbanization have collectively led to a substantial increase in energy demand, thereby exerting significant pressure on available resources [1]. The judicious utilization of energy resources is imperative not only to curtail expenditures but also to mitigate environmental degradation. Among the various strategies employed to address this issue, energy efficiency has emerged as a potent instrument for achieving the delicate balance between economic growth and sustainability objectives [2]. In this regard, thermal insulation in buildings emerges as a pivotal application for energy conservation, reduction of heat loss, and enhancement of thermal comfort for occupants [3].

Over the years, extensive research has been conducted to evaluate the influence of insulation material types and thicknesses on energy efficiency and thermal performance. For example, Arif [4] investigated the energy savings potential of various insulation thicknesses in the Elazığ region, identifying optimal configurations for reducing energy consumption. Similarly, Semiha and Emre [5] applied a life-cycle cost analysis approach, concluding that expanded polystyrene (EPS) combined with coal offered the most cost-effective insulation solution. Erdem and Volkan [6] extended the analysis to three different cities in Turkey, determining optimal insulation thicknesses based on regional climatic conditions and economic considerations. Hüseyin et al. [7] focused on the Yalova region and found that

a minimum insulation thickness of 2 cm is required to achieve satisfactory energy efficiency. Further studies have explored the long-term benefits of insulation materials, such as energy savings and reduced payback periods, across various regions and climates [8]-[13].

These investigations have demonstrated that selecting the appropriate insulation material can significantly influence a building's operational energy efficiency, particularly in regions with extreme climatic conditions. Advanced insulation materials, such as aerogels and phase-change materials (PCMs), have shown superior performance in regulating heat flow compared to conventional insulation options. Their ability to adapt to temperature fluctuations enhances indoor thermal stability while reducing energy consumption for heating and cooling purposes.

Beyond energy efficiency, sustainable insulation solutions contribute to environmental conservation by lowering greenhouse gas emissions associated with excessive energy use. Erzen et al. [14] emphasized the importance of integrating bio-based insulation materials, such as hemp and cellulose fibers, as viable alternatives to synthetic insulations. These materials not only provide effective thermal resistance but also support circular economy principles by utilizing renewable and biodegradable resources. Additionally, insulation materials with high resistance to moisture and microbial growth, such as extruded polystyrene (XPS), have been recognized for their long-term durability and reduced maintenance costs.

In addition to material selection, optimizing insulation thickness is a crucial factor in maximizing energy efficiency. Various studies have employed computational modeling and life-cycle cost analyses to determine the ideal insulation thickness required for different climatic zones, ensuring that energy savings offset initial investment costs. Recent advancements in smart insulation technologies, such as thermally adaptive coatings and dynamic insulation systems, have further expanded possibilities for improving thermal performance by responding dynamically to environmental conditions.

These findings highlight the necessity of a holistic approach to insulation design that incorporates material properties, optimal thickness, climate adaptability, and economic feasibility. Future research should focus on hybrid insulation systems that combine multiple materials to achieve enhanced thermal resistance and energy conservation. Additionally, integrating insulation solutions with renewable energy technologies, such as photovoltaic panels and geothermal heating, presents a promising avenue for advancing net-zero energy buildings. By leveraging these innovations, the construction industry can move toward a more sustainable, energy-efficient future, reducing both operational costs and environmental impact.

2. Material and Methods

To analyze the thermal performance under various experimental conditions, a one-story, one-room, one-roof building model was constructed using medium-density fibreboard (MDF) material. Thermocouples were installed on a side wall of the building, on the roof, and on the floor at strategic locations to provide accurate temperature measurements. In addition, a nozzle bundle of 25 nozzles was integrated into another wall of the building. Indoor temperatures were monitored using these thermocouples, air was introduced into the room through the nozzle bundles, and hot air was exhausted using an aspirator to provide effective air circulation throughout the building. The experiments were carried out on the terrace of the Mechanical Engineering Department of the Faculty of Engineering of Fırat University.Schematic illustration of experimental setup given in Fig.1.

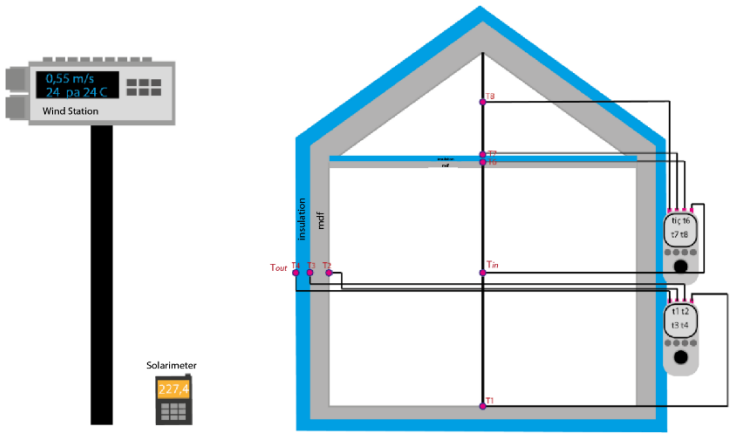

Fig.1 Schematic View of Experimental Setup

The exterior surfaces of the building and the roof cavity were covered with different types of thermal insulation materials (**Figs.1-2**). The experimental design includes a total of 36 tests covering all aspects of the building. Temperature measurements were taken simultaneously with two four-channel thermometers and recorded digitally. Instantaneous solar radiation was measured automatically with a radiation meter, while outside temperature, wind speed and direction were measured with a wind station.

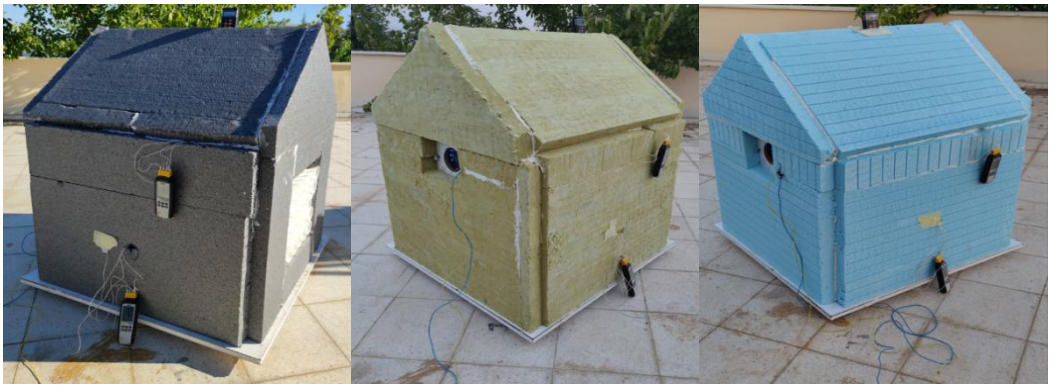

a) b) c)

Fig.2 Picture of a building covered with a) EPS b) Stone-wool c) XPS thermal insulation material

The measurements were obtained during two distinct time periods: from 8:00 a.m. to 4:00 p.m. (daytime) and from 9:00 p.m. to 5:00 a.m. (nighttime). The collected data were then meticulously arranged into graphs to facilitate analysis and visualization. The effect of radiation was significant during the daytime hours and was taken into account in the calculations, while at night the effect of radiation was either completely negligible or absent. This comprehensive experimental setup aims to analyze in detail the effects of insulation materials on energy savings and thermal comfort.

2.1. Calculations

The following equations were used to make the necessary calculations in the experiment. Heat loss from side walls and roof:

$$q_{rad} + \frac{T_{out} - T_4}{\frac{1}{h_{out}}} = \frac{T_4 - T_3}{\frac{l_i}{k_{iy}}} = \frac{T_3 - T_2}{\frac{l_l}{k_l}} = \frac{T_2 - T_{in}}{\frac{1}{h_{in}}} \quad (1)$$

$$F = 0.5\, Re^{2/3} \tag{6}$$

$$q_{side} = q_{rad} + \frac{T_{out} - T_4}{\frac{1}{h_{out}}} \tag{2}$$

$$q_{fl} = \frac{T_1 - T_{\text{in}}}{\frac{1}{h_{\text{in}}}} \tag{3}$$

$$q_{rf} = \frac{T_7 - T_6}{\frac{l_s}{k_s}} \tag{4}$$

Nusselt calculation for circle nozzle [15]:

$$\frac{Nu}{P_r} = K \times G \times F \tag{5}$$

$$K = [1 + (\frac{H/D}{0.6/A_r^{1/2}})^6]^{-0.05} \tag{7}$$

$$G = 2Ar^{1/2}\, \frac{1 - 2.2Ar^{1/2}}{1 + 0.2\left(\frac{H}{D-6}\right)Ar^{1/2}} \tag{8}$$

Heat loss from nozzle Wall:

$$Nu = \frac{h\, d}{k} \tag{9}$$

$$q_n = h\,(T_{out} - T_{\text{in}}) \tag{10}$$

$$q_{nw} = \frac{q_{side}\, A_f + q_n \sum A_n}{A} \tag{11}$$

Calculation of the radiation intensity falling on the side surfaces

The heat flux values measured by the solar meter for the horizontal plane were calculated for the vertical plane. The geometric factor R_b is defined as the ratio of the instantaneous direct radiation (I_b) falling on the inclined surface to the instantaneous direct radiation (I_b) falling on the horizontal surface, for the northern hemisphere this value is found from the following expression [16].

$$R_b = \frac{\cos(\varphi - \beta) \times \cos\delta \times \cos\omega + \sin(\varphi - \beta) \times \sin\delta}{\cos\varphi \times \cos\delta \times \cos\omega + \sin\varphi \times \sin\delta} \tag{12}$$

Here:

φ = Latitude angle

β = Inclination angle of the surface in horizontal position

ω = Clock angle

δ = Declination angle

Latitude angle =38.7° for Elazığ province.

The hour angle converts local solar time (*LST*) into the number of degrees the sun moves across the sky. Since the Earth rotates 15° per hour, each hour of solar noon corresponds to 15° of angular movement of the sun across the sky and is calculated by the formula.

$$\omega = 15° \times (LST - 12) \quad (13)$$

3. Results And Discussions

The side wall where the thermocouples were placed (Fig. 1) was oriented north-south-east-west, and the effect of orientation was taken into account in the heat transfer calculations. Graphs were plotted at one-hour intervals between 08:00 and 16:00 for daytime hours and between 21:00 and 05:00 for nighttime hours. Since the effect of radiation is high during daytime hours, it is taken into account in the calculations. In addition, the instantaneous wind speed was measured during the experimental hours and recorded in a table.

Figs. 3a-d show the heat flux vs. time graphs during the daytime hours for the side-wall-ceiling-floor-nozzle wall covered with EPS 4 cm insulation material. Fig. 4 shows the radiation intensity-time graph. Then the instantaneous wind speed table is given. Fig. 5 and Table. 2 show the results for the night time.

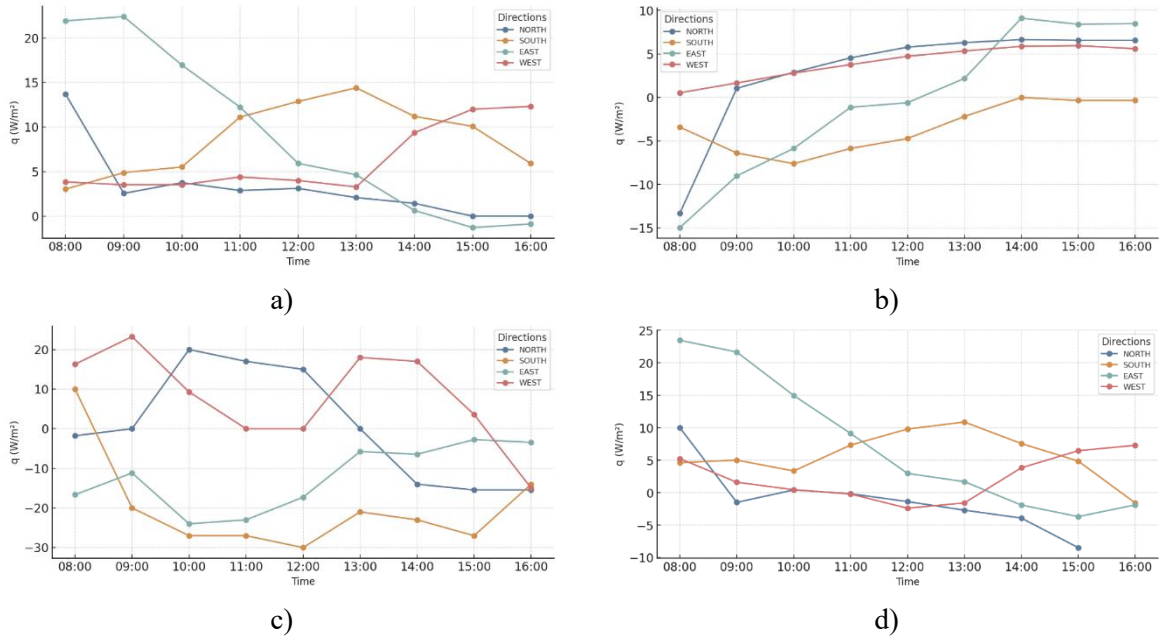

Fig. 3 Variation of heat flux with time for EPS 4 cm a) daytime-side Wall b) daytime - ceiling c) daytime-floor d) day-nozzle

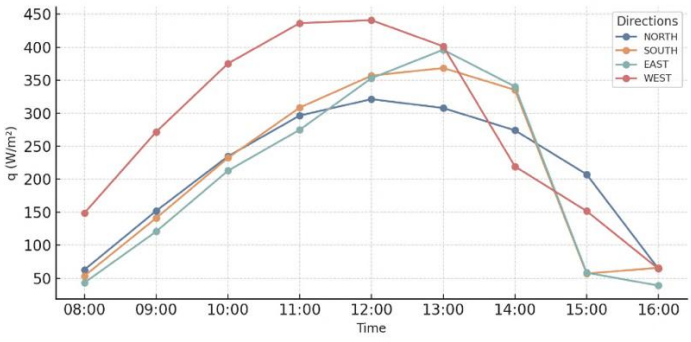

Fig. 4 Variation of the radiation intensity incident on the vertical surface with respect to time for EPS 4 cm

Table 1. EPS 4 cm instantaneous daytime wind speed values (*m/s*)

Time	North	South	East	West
08.00	0,7	0	0	0,7
09.00	0,7	0,7	0,7	1
10.00	1	1	1,7	2
11.00	0,7	2,7	2,7	2
12.00	3,7	2,7	2	2,7
13.00	2,7	5,1	3,1	1
14.00	1	4,8	1,7	3,7
15.00	2	2,7	1,7	4,8
16.00	2	3,7	2	3,1

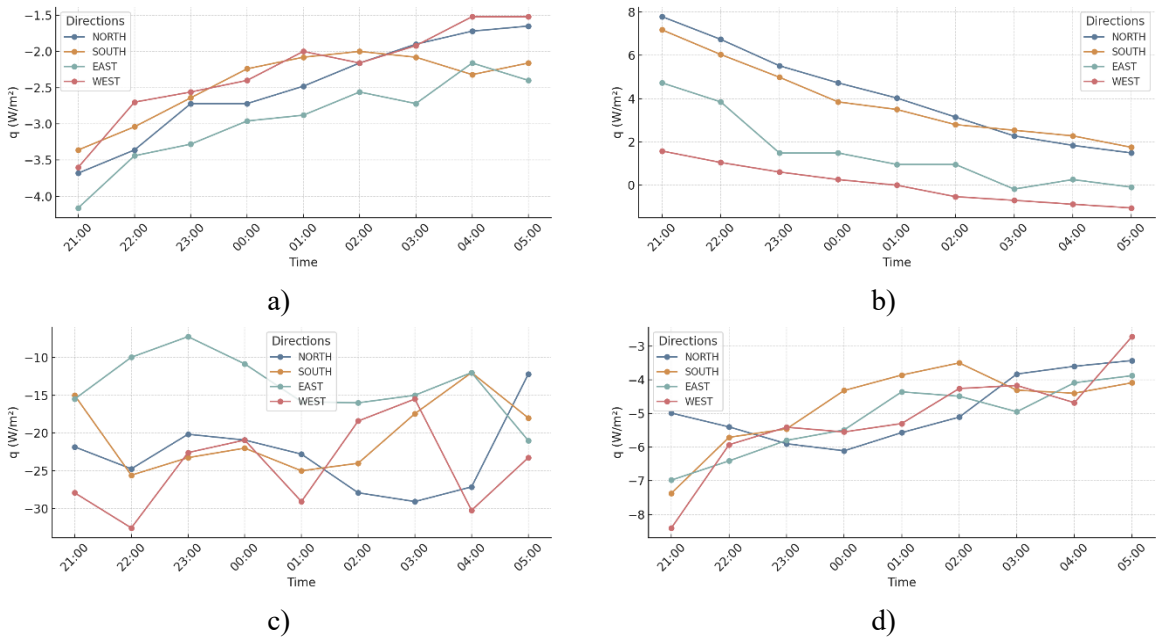

Fig. 5 Variation of heat flux with time for EPS 4 cm **a)** night-side wall **b)** night-ceiling **c)** night-flooring **d)** night-nozzle

Table 2. EPS 4 cm instantaneous wind speed values at night (*m/sec*)

Time	North	South	East	West
21.00	2	0	0,7	0
22.00	0	0,7	0,7	0,7
23.00	0,7	0,7	0,7	0
00.00	0,7	0	0,7	0
01.00	0	0	0	0
02.00	0,7	0,7	0	0
03.00	0,7	0	0,7	0
04.00	0	0	0	0,7
05.00	0,7	0,7	0,7	0,7

Fig. 3a. shows the heat transfer (q) through the side wall during daytime hours for EPS 4 cm. On the east-facing wall, q is higher in the morning and decreases later in the day, while on the west-facing surface, on the contrary, it is lower in the morning and increases in the afternoon. On the south-facing surface, q increases until noon and then decreases. On the north-facing surface, q is larger in the morning and decreases later in the day. This trend is similar for other insulation materials.

Fig. 4a. shows the heat transfer through the side wall at night for EPS 4 cm. As can be seen from the figure, the east and north facing surfaces cool down faster at night while the south and west facing surfaces cool down later.

When the heat transfer through the ceiling for EPS 4 cm during daytime hours is analyzed (Fig. 3b), it is seen that q increases from the morning hours in all directions of the building and reaches maximum values between 14-16 hours.

Fig. 4b shows the heat transfer through the ceiling at night for EPS 4 cm. Contrary to the daytime hours, q decreases gradually until the morning and reaches minimum values between 05-08 hours.

As illustrated in Fig. 3c, the heat transfer through the floor during daytime hours for EPS with a thickness of 4 cm is depicted. In all directions, q shows an approximately horizontal trend. However, in the experiments conducted on the south side of the building, this trend was temporarily disrupted due to the sudden appearance of a wind after 11:00 a.m. (see Table 2). This was followed by the closure of the air and the decrease in radiation intensity (a similar situation occurred on the north side after 12:00 p.m.). The horizontal trend in q, with the exception of sudden changes in conditions, is consistent for all insulation thicknesses and types, extending even during nocturnal periods (Fig. 5c).

Fig. 3d shows the heat transfer through the nozzled wall during daytime hours. As can be seen from the figure, the nozzled system was not very effective during daytime hours. It is seen that the nozzled system is effective after 17-20 hours and rapidly decreases the indoor temperature (Fig. 5c). This effect continues until 07-08 am the next day. After 08:00 am, the indoor environment starts to warm up again and the temperature increases rapidly.

The maximum indoor temperatures of the day are recorded between 15:00 and 16:00. In order to forestall the precipitous rise in indoor temperature during daylight hours, it is advisable to maintain the closure of windows (and, by extension, the nozzles) from 8:00 a.m. onward until the evening hours.

Fig. 4 shows the variation of radiation intensity with respect to time for EPS 4 cm. Table 3.1 shows the instantaneous wind speed during the daytime hours on the days when the EPS 4 cm experiments were conducted. Table. 2 shows the wind speeds at night on the same days.

As illustrated in Figure 6a, a comparison was conducted of 4 cm-thick insulation materials during daytime hours with the side wall facing east. As depicted in the figure, the lowest q is obtained in XPS during the early morning hours. At noon, there is no significant difference in q between the insulation materials.

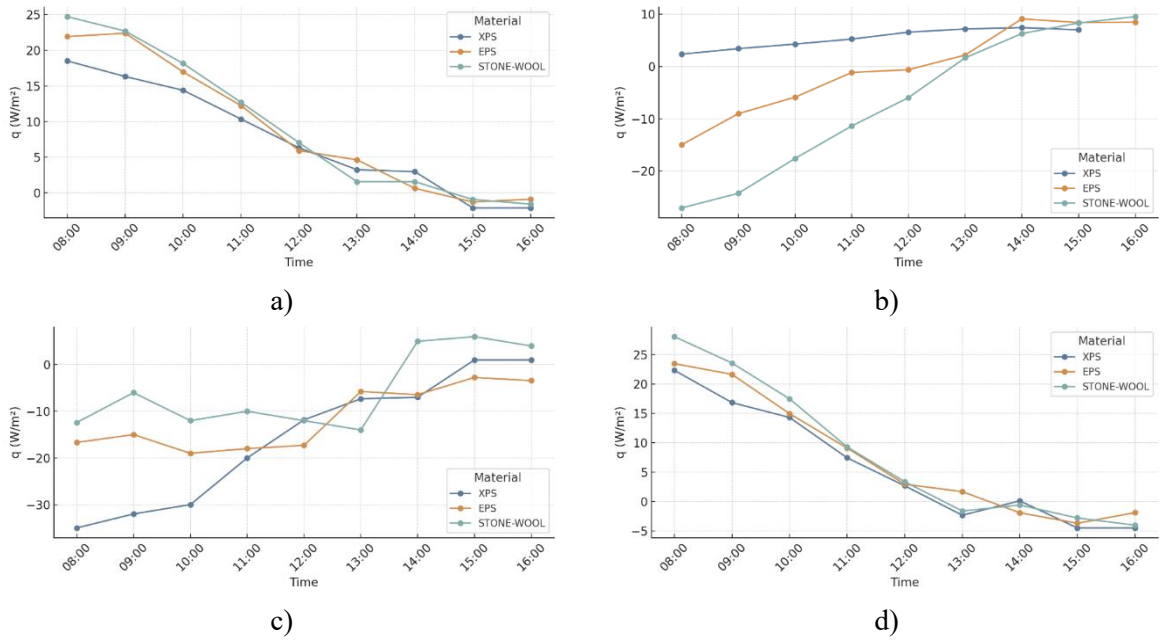

Fig. 6 Comparison of 4 cm thick insulation materials a) daytime-side wall b) day-ceiling c) daytime-flooring d) day-nozzle

Fig. 6b shows the values found for the ceiling at the same thickness during daytime hours. In this figure, in contrast to the previous one, XPS was the highest in the morning hours. However, the results are significantly affected by the fact that both the radiation intensity decreases and the wind speed is much higher on the test days with other insulation materials (Fig. 4, Table 1). Figs. 6c-d show the heat transfer from the floor and nozzled wall respectively under the same conditions. In both figures, it is seen that the lowest values of q are obtained for XPS in the morning hours. Figs 7a-d graphs plotted at night time.

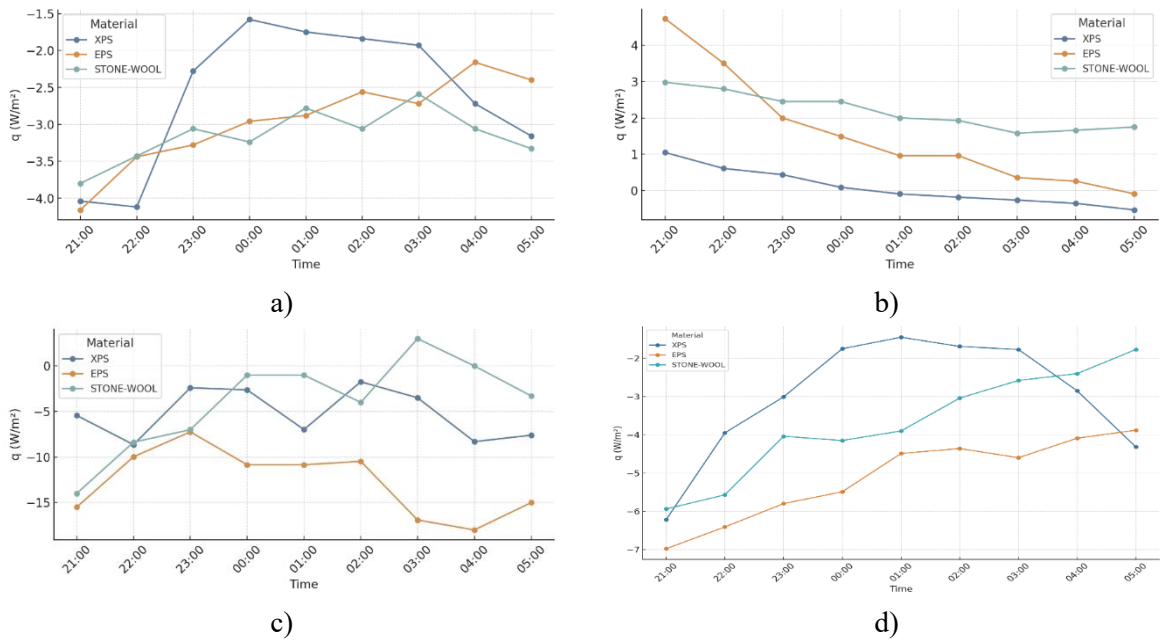

Fig. 7 Comparison of 4 cm thick insulation materials a) night-side wall b) night-ceiling c) night-flooring d) night-nozzle

The figures presented above illustrate the heat transfer from each wall of the building individually. However, due to the variability in weather conditions on the test days and at the time of the experiment, it was not feasible to calculate the total heat transfer from the building on the same day. The following figures are given to compare the inside-outside temperature differences for the north-facing nozzle (exterior wall direction east). Figs. 8a-b show the variation of 4 cm thick insulation materials with respect to each other during daytime and nighttime, respectively.

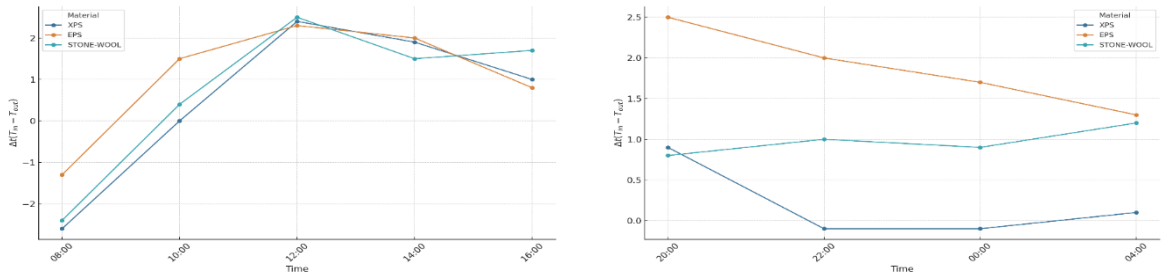

a) b)

Fig. 8 Comparison of temperature differences for insulation materials with 4 cm insulation thickness a) daytime - north facing nozzle direction b) night - north facing nozzle direction

As illustrated in **Fig. 8a-b,** the XPS-nozzle system demonstrates optimal cooling during the early morning and nighttime hours.

3.1. Uncertainty Analysis

In this study, the uncertainties in the measured values are evaluated using the Kline and McClintock [17] methodology. This method offers a structured and reliable approach for quantifying measurement uncertainties, ensuring the accuracy and credibility of the experimental results.
With uncertainty analysis, the error rate is obtained by *Eq.14* .

$$W_R = [(\frac{\partial R}{\partial X_1} W_1)2 + (\frac{\partial R}{\partial X_2} W_2)2 + (\frac{\partial R}{\partial X_3} W_3)2 + ... + (\frac{\partial R}{\partial X_n} W_n)2] \quad (14)$$

In a measurement with *n* independent variables.

R: dimension to be measured

$X_1, X_2, X_3, ……, X_n$: are the variables affecting the measurement

$W_1, W_2, W_3, …, W_n$: is the error rate due to the independent variable

W_R, is the total uncertainty ratio.

In the experimental study, measurements were obtained by means of digital thermometers. In the experimental setup, the results were affected by errors due to thermometer and temperature measurement. Akpınar [18] stated some of the error amounts in his article as follows. According to these values, the error rate resulting from the study was calculated as shown below.

a. Error due to digital thermometers = ±0.1 °C
b. Error due to thermocouples = ±0.25-0.5 °C
c. Error due to points and fasteners = ±0.1 °C
d. Error in measuring the center temperature = ±0.25°C
e. The average error that can be made in measuring ambient temperature = ±0.25°C

$$W_R = [(a)^2 + (b)^2 + (c)^2 + (d)^2 + (e)^2]^{½} = [(1)^2 + (0.5)^2 + (0.1)^2 + (0.25)^2 + (0.25)^2]^{½} = \pm 1.176°C$$

4. Conclusions

The present study evaluated the thermal performance and energy efficiency of three distinct insulation materials—expanded polystyrene (EPS), extruded polystyrene (XPS), and stone wool—in a single-story wooden building model. The findings yielded significant insights into the effectiveness of these materials in enhancing indoor thermal comfort and reducing energy consumption. The findings demonstrated distinct advantages for each material depending on the building orientation and environmental conditions.

Table 3. Comparison of the lowest indoor temperatures of all insulation materials during night hours

T_{in}	West	East	South	North
Eps	**25,2**	25,3	25,5	**22,3**
Xps	24,5	27,6	25,2	25,8
Stone-Wool	25,3	**21,9**	**23,1**	25,5

XPS insulation consistently outperformed other materials in reducing heat transfer during both daytime and nighttime. It achieved the lowest recorded indoor temperature in the west orientation (24.5°C) and performed efficiently across other directions, showcasing its effectiveness as a thermal barrier, especially in regions with significant diurnal temperature variations. Stone wool excelled in specific orientations, achieving the lowest overall indoor temperature in the east direction (21.9°C) and demonstrating its suitability for targeted applications. EPS insulation, while slightly less effective overall, achieved the lowest temperatures in the north (22.3°C) and west (25.2°C) directions, indicating its potential for these orientations.

The integration of a nozzle cooling system has demonstrated effectiveness in reducing indoor temperatures during nighttime, thereby enhancing thermal comfort. However, its limited influence during the daytime suggests the need for optimization. Potential improvements include coupling the system with advanced ventilation controls, automated shading mechanisms, or complementary passive and active cooling strategies. Furthermore, external environmental variables such as solar radiation intensity, wind speed, and ambient temperature fluctuations play a crucial role in heat transfer dynamics. These factors must be carefully considered when designing and assessing insulation performance to ensure optimal energy efficiency and indoor climate stability.

These findings highlight the necessity of selecting insulation materials based on a combination of building orientation, local climatic conditions, and operational requirements. For instance, extruded polystyrene (XPS) is particularly suitable for regions that demand a robust thermal barrier across various orientations due to its low thermal conductivity and moisture resistance. Conversely, stone wool may offer superior performance for eastern and southern-facing walls, where solar exposure patterns necessitate materials with high thermal mass and fire resistance. Additionally, operational strategies such as maintaining windows and nozzles closed during peak daytime heat can further improve indoor thermal stability while minimizing energy consumption.

Beyond the immediate implications for building design, this study reinforces the broader significance of insulation in reducing energy demands and advancing sustainability objectives. By effectively lowering heating and cooling loads, strategic insulation deployment contributes to environmental conservation efforts and enhances overall building performance. Future research should focus on evaluating the long-term durability and thermal resistance of various insulation materials under real-world conditions, conducting comprehensive lifecycle cost analyses, and exploring the integration of renewable energy systems, such as solar photovoltaic panels and geothermal heating, into holistic building solutions.

Combining cutting-edge insulation technologies with renewable energy sources presents a promising pathway toward achieving energy-efficient, resilient, and self-sustaining built environments. In conclusion, this study underscores the pivotal role of strategic insulation design in enhancing thermal comfort, reducing energy consumption, and promoting environmental sustainability. It offers valuable insights for researchers, architects, and policymakers seeking to develop innovative solutions that align with global energy efficiency and climate resilience goals.

Ethical statement

The author declares that this document does not require ethics committee approval or any special permission.

Acknowledgment

This work was supported by FUBAP under Grant No. MF.22.25 The authors gratefully acknowledge the financial support provided for this research.

Conflict of interest

The author declares no conflict of interest.

Authors' Contributions

A.Ç.K: Methodology, Conceptualization, Investigation

C. K: Investigation, Writing - Original draft preparation, Investigation

H. E: Conceptualization, Methodology, Supervising

Generative AI statement

The author(s) declare that no Gen AI was used in the creation of this manuscript.

References

[1] Ministry of Energy and Natural Resources, "Energy statistics and projections" [Online]. Available: https://enerji.gov.tr/. Accessed: Feb. 16, 2023.

[2] Ministry of Energy and Natural Resources, "Turkey's electricity energy demand projection report," Report No. 114176, 2023.

[3] Çankaya, B., "Yıllık Enerji Tüketimi 1.000 Tep Üzeri Bir Sanayi İşletmesinin Enerji Etüdü," MSc. thesis, Necmettin Erbakan Üniversitesi, Fen Bilimleri Enstitüsü, Konya, Türkiye, 2022.

[4] Yalçın, A., "Elazığ İlinde Kullanılan Farklı Duvar Tipleri İçin Optimum Yalıtım Kalınlığının Belirlenmesi ve Ekonomi Analizi," MSc. thesis, Fırat Üniversitesi, Fen Bilimleri Enstitüsü, Elazığ, Türkiye, 2012.

[5] Öztuna, S., Dereli, E., "Edirne İlinde Optimum Duvar Yalıtım Kalınlığının Enerji Tasarrufuna Etkisi," *Trakya Univ J Sci*, 10(2), 139-147, 2009.

[6] Tuğan, V., Işık, E., "Tunceli, Hakkâri ve Kars İllerinin Optimum Isı Yalıtım Kalınlığının Hesaplanması," *J. Pure Appl. Sci*., 3(2), 50-57, 2017.

[7] Ülgüner, H., Değirmenci, A., Üstüntürk, A., Keleşoğlu, A., Ünver, Ü., "Binalarda Yalıtım Malzemelerinin Performans Analizi," *Uludağ Üniversitesi Mühendislik Fakültesi Dergisi*, 23(2), 367-381, 2018. DOI: 10.17482/Uumfd.356648.

[8] Kotan, T., Fırat, İ., Kaya, M., Ulusu, İ., "Binalarda Kullanılan Farklı Isı Yalıtım Malzemelerinin Isı İletkenlik Katsayılarının Erzincan İli Şartlarında Termokupl ve Termal Kamera ile İncelenmesi," *Uludağ Üniversitesi Mühendislik Fakültesi Dergisi*, 23(2), 367–382, 2018. DOI: 10.17482/uumfd.356648.

[9] Dumrul, M., Uçar, A., "Bir Konutun Dış Duvarları İçin Isıtma ve Soğutma Yüklerine Göre Optimum Yalıtım Kalınlığının Tespiti ve Enerji Tasarrufu Analizi," *Avrupa Bilim ve Teknoloji Dergisi,* 16, 740-749, 2019.

[10] Ögetürk, İ., "Binalarda Isı Yalıtım Malzemelerinin Enerji Verimliliği Üzerine Etkisinin Araştırılması," MSc. thesis, Batman Üniversitesi, Fen Bilimleri Enstitüsü, Batman, Türkiye, 2019.

[11] Tunç, D., Özel, M., "Kars İlindeki Binalar İçin Isıtma Yükü ve Optimum Yalıtım Kalınlığının Belirlenmesi," *Fırat Üniv. Müh. Bil. Dergisi*, 30(1), 251-257, 2018.

[12] Bıyıkoğlu, A., Aydın, N., "Türkiye'de Konut Tipi Binaların Isıtma Yükü Altında Ömür Maliyet Analizi Yöntemi ile Optimum Yalıtım Kalınlıklarının Belirlenmesi," *Politeknik Dergisi*, 22(4), 901-911, 2019. DOI: 10.2339/Politeknik.435773.

[13] Bayer, G., "Binalarda Uygulanan Isı Yalıtım Sistemleri ve Örnek Bir Projede Isı Yalıtım Maliyet Analizi," MSc. thesis, Sakarya Üniversitesi, Fen Bilimleri Enstitüsü, Sakarya, Türkiye, 2006.

[14] Erzen, B., Karataş, M., Orhan, R., Aydoğmuş, E., "Innovative Insulation Materials: A Comprehensive Review of Current Trends, Challenges, and Future Directions in Sustainable Building Technologies," *Polymer-Plastics Technol. Mater*., 1–24, 2025.

[15] Bergman, T. L., Lavine, A. S., Incropera, F. P., DeWitt, D. P., Fundamentals of Heat and Mass Transfer, 8th ed., Hoboken, NJ, USA: Wiley, 2018.

[16] Yiğit, A., Arslanoğlu, N., "Investigation of Optimum PV Panel Angle, Efficiency, and Power Output Depending on Instantaneous Radiation Intensity and Environmental Factors," *Uludağ Univ. J. Fac. Eng*., 26(1), 301–314, 2021. DOI: 10.17482/uumfd.824582.

[17] Kline, S. J., McClintock, F. A., "Describing Uncertainties in Single-Sample Experiments," Mech. Eng., 75, 3–8, 1953.

[18] Akpınar, E.K., Deneysel Çalışmalardaki Hata Analizine Bir Örnek: Kurutma Deneylerindeki Hata Analizi, *Mühendis ve Makina Dergisi*, 46(540), 41-48.

Middle East Journal of Science

https://dergipark.org.tr/mejs

MEJS

e-ISSN:2618-6136

Case Study

46,XY,t(1;2;12;6;16)(q42;q23;q22;q13;q13) REPORT OF A CASE WITH SEX DIFFERENTIATION DISORDER (DSD) WITH COMPLEX CHROMOSOMAL REARRANGEMENT

***Diclehan ORAL*[1] *Gülbahar GÜZEL ERDAL*[1]* *İlyas YÜCEL* [1] *Mahmut BALKAN* [1] *Füsun DÜZCAN* [2]

[1]Dicle University, Faculty of Medicine, Department of Medical Biology and Genetics, Diyarbakır, Turkey
[2]Izmir Tınaztepe University,Department of Medical Genetics, İzmir, Turkey
* Corresponding author; gulbaharguzel@yahoo.com

Abstract: *In this study, we present a case of a 7-month-and-26-day-old patient with a novel karyotype associated with a 46,XY disorder of sexual development. This complex chromosomal rearrangements, described as 46,XY,t(1;2;12;6;16)(q42;q23;q22;q13;q13), was confirmed by FISH analysis and has not been previously reported in the literature. The patient exhibited ambiguous genitalia and faced urinary obstruction. No pathogenic variants were detected in genes associated with disorders of sex development in the Next-Generation Sequencing (panel, suggesting that structural rearrangements may disrupt genes critical for sexual and neurological development. Laparoscopic-assisted urogenital mobilisation successfully improved urinary function and genital appearance. This case demonstrates that the pathogenesis of disorders of sex development may involve structural chromosomal abnormalities in addition to gene-level mutations and highlights the importance of genomic rearrangements in disorders of sexual development. The findings emphasise the need for a multidisciplinary approach to the diagnosis and management of complex cases of disorders of sex development. Chromosomal abnormalities should be considered even in the presence of normal sex development genes. This rare karyotype provides new insights into the genetic basis of disorders of sex development, as similar cases have not been documented. We believe that reporting such unique cases will contribute to the understanding of the molecular mechanisms of disorders of sex development and the development of clinical strategies. In summary, we emphasize that structural chromosomal alterations can contribute to disorders of sex development independently of gene mutations and the value of genetic, clinical, and surgical collaboration in patient evaluation. This case expands knowledge of the etiology of disorders of sex development and supports further research on structural genomic alterations.*

Key words: *DSD, ambiguous genitalia, complex chromosomal rearrangement.*

Received:April 22, 2025 *Accepted:June 21, 2025*

1. Introduction

Ambiguous genitalia, a key feature of disorders of sex development (DSD), occurs in approximately 1 in 4,500 births and arises from disruptions in chromosomal, gonadal, or hormonal pathways governing sexual differentiation [1]. These disorders result from genetic mutations (e.g., in SRY and NR5A1), enzyme deficiencies (e.g., 21-hydroxylase), or complex chromosomal rearrangements that disrupt testicular or ovarian development [2]. During critical embryological stages (weeks 6-20 of gestation), abnormal androgen production, receptor dysfunction, or anti-Müllerian

hormone defects can lead to discordance between genetic sex and phenotypic genital development [3]. The resulting spectrum includes undervirilized males, masculinized females, or truly ambiguous anatomy, often requiring multidisciplinary diagnostic approaches.

Complex chromosomal rearrangements (CCRs), though rare, can disrupt multiple phases of sexual development by altering dosage-sensitive genes or regulatory elements. These structural anomalies may affect gonadal formation (weeks 6-8), steroidogenesis (weeks 8-12), or late genital maturation (weeks 12+), frequently presenting with ambiguous genitalia alongside other congenital anomalies [4]. Phenotypic variability depends on the affected genomic regions—for instance, rearrangements near SOX9 may cause 46,XY DSD, while DAX1 duplications can lead to 46,XY gonadal dysgenesis [5]. Given this complexity, advanced cytogenetics (karyotyping, FISH, microarray) and hormone profiling are essential for accurate classification and management.

2. Materials and Methods

Karyotype analysis was requested from a 7-month and 26-day-old patient admitted to Dicle University Faculty of Medicine Paediatric Endocrinology Clinic in March 2024 due to ambiguous genitalia. The study was approved by the Medical Ethics Committee. Dicle University Faculty of Medicine Ethics Committee (Ethics approval code:125).

2.1. Pedigree Analysis

The pedigree analysis revealed no consanguineous relationship between the progenitor's presentation, the infant's growth parameters (69 cm length, 7.65 kg weight) were appropriate for chronological age, with both measurements plotting within normal percentile ranges. On physical examination, a bilateral labial mass could not be palpated. In the pelvic ultrasonography examination, the left testicle was observed in the middle part of the inguinal canal, and its dimensions were measured as 10x6.5x14 mm. The right testicle could not be visualised along the inguinal canal. Cerebral ultrasonography showed that the ventricular system of the brain was symmetrical and aligned. Ventricular width was found to be within normal limits. The corpus callosum was visualised in sagittal sections, and its structural integrity was preserved. Echocardiography showed normal anatomical structures of the heart. The dimensions of the cardiac cavities, wall thickness of the ventricles and atria, valvular structures, and positions of the great vessels were within normal limits. Cardiac functions (ejection fraction, cardiac output) were measured normally.

According to the hearing test results, the baby's bilateral hearing was found to be within normal limits. Audiological evaluation showed that both ears responded to normal auditory stimuli. Hearing loss or pathological findings in auditory pathways were not detected.

2.2. Biochemical analyses

Biochemical analyses revealed normal thyroid function (TSH: 2.186 mIU/L, reference: 0.79-5.85; FT4: 1.06 ng/dL, reference: 0.64-1.71) and adequate cortisol levels (12.9 µg/dL, reference: 6.7-22.6). Gonadotropin levels were at the lower reference limit (FSH: 1.82 IU/L, reference: 1.27-19.26; LH: 0.75 IU/L, reference: 1.24-8.62), with markedly suppressed androgen production evidenced by undetectable testosterone (<0.01 ng/dL, reference: 1.75-7.81) and subnormal DHEA levels (<15 µg/L, reference: 80-160). Additional markers showed serum AFP (75 ng/mL) within the expected range for gestational age and undetectable hCG (0.38 mIU/mL, reference: <5).

2.3. Cytogenetic analysis

Cytogenetic analysis was performed using the standard lymphocyte culture technique, and a complex chromosomal rearrangement was detected: The specific chromosomal configuration is defined as 46,XY,t(1;2;12;6;16)(q42;q23;q22;q13;q13). A total of 50 metaphase cells were examined, and the results were confirmed. This novel karyotype demonstrates a unique pattern of balanced translocations involving five distinct chromosomal regions (Figure 1), representing an exceptionally rare cytogenetic finding in disorders of sex development.

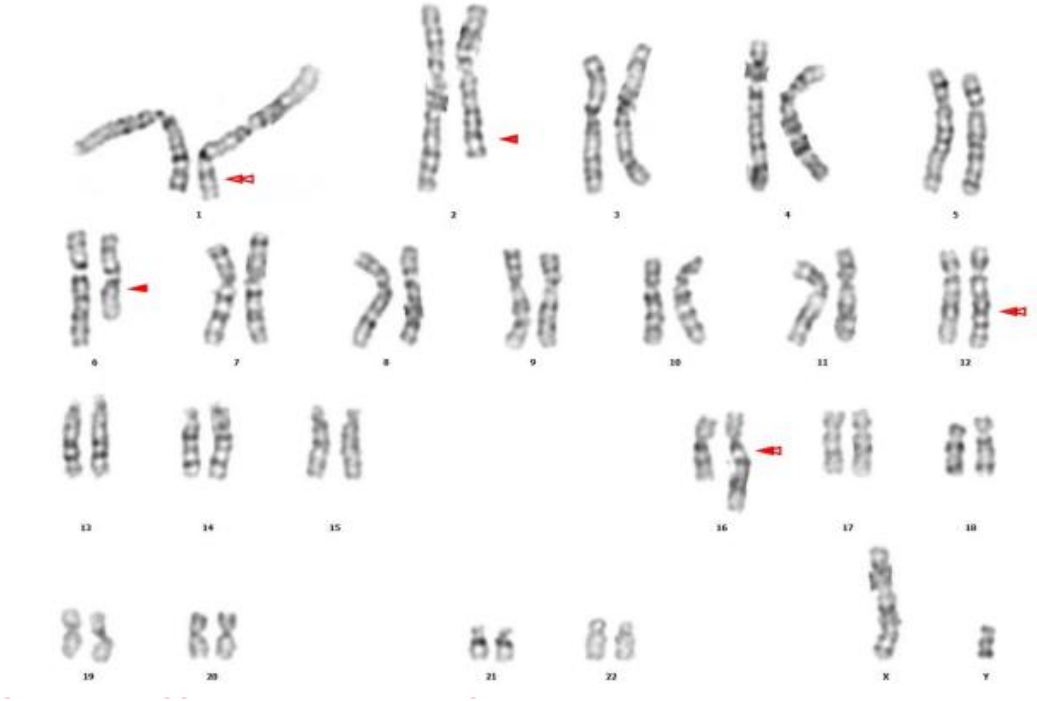

Figure 1. The karyotype of the patient was 46, XY, t(1;2;12;6;16)(q42;q23;q22;q13;q13). In detail, the chromosome 1 segment distal to 1q42 was assigned to the 2q23 region on chromosome 2; the chromosome 2 segment distal to 2q23 was assigned to the 12q22 region on chromosome 12; the chromosome 12 segment distal to 12q22 was assigned to the 6q13 region on chromosome 6; The chromosome 6 segment distal to 6q13 translocated to the 16q13 region on chromosome 16; and the chromosome 16 segment distal to 16q13 translocated to the 1q42 region on chromosome 1.

To confirm these complex chromosomal rearrangements, fluorescence in situ hybridisation (FISH) analysis was performed on metaphase plates obtained from cells cultured from the patient's peripheral blood sample using the CytoCell® TeloMark kit. A total of 50 different probes, including 41 subtelomeric-specific probes, three centromeric probes, and six locus-specific probes, were used in this analysis, and the presence of translocations was confirmed (Figure 2).

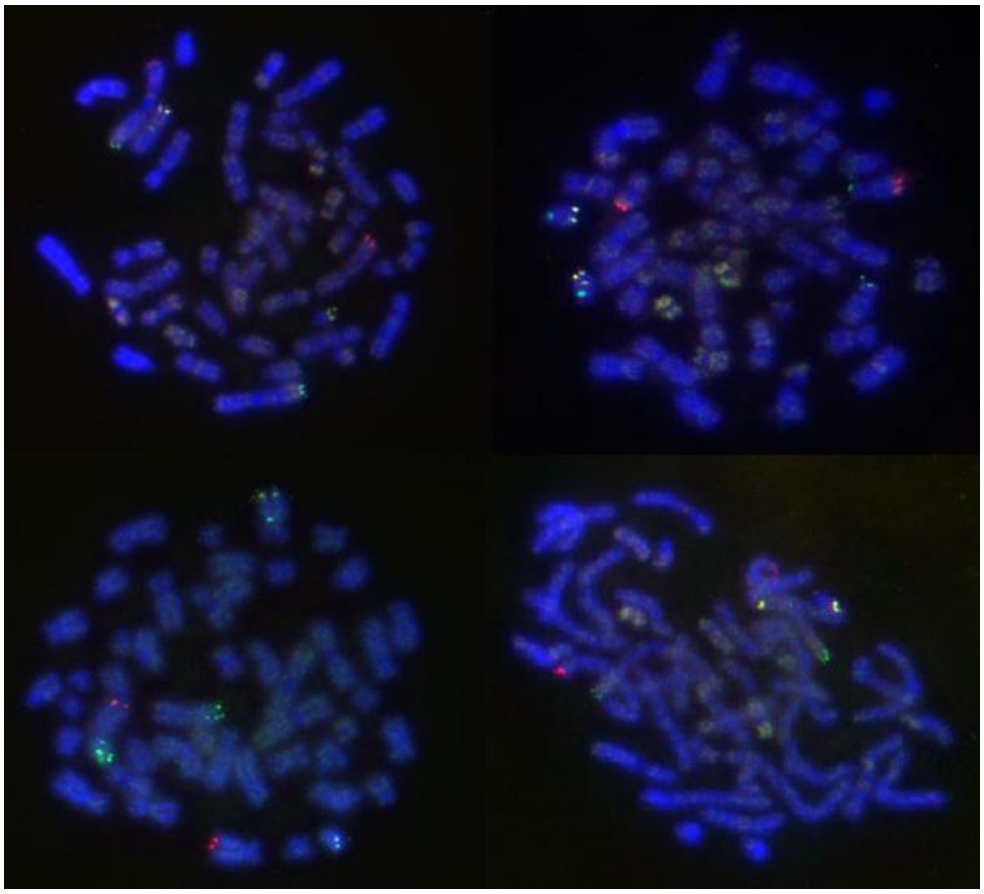

Figure 2. Patient's 46,XY,t(1;2;12;6;16)(q42;q23;q22;q13;q13) karyotype confirmed by FISH.

2.4. Genomic DNA Extraction and Quantification

Genomic DNA was extracted from peripheral blood samples using the QIAamp DNA Blood Kit (QIAGEN, Hilden, Germany) on an automated QIAcube HT platform, according to the manufacturer's protocol. DNA concentration and purity were assessed fluorometrically using the Qubit™ 4.0 system with the dsDNA High Sensitivity Assay Kit (Invitrogen, Waltham, MA, USA), ensuring optimal quality for downstream sequencing applications.

2.5. Next-Generation Sequencing and Variant Analysis

A targeted next-generation sequencing panel encompassing all known DSD-associated genes was performed, with comprehensive coverage of exonic regions and flanking ±10 bp intronic sequences. Sequencing was aligned to the GRCh37/hg19 reference genome, achieving a mean read depth of 20× and 99.65% coverage of the target regions. The list of 65 DSD genes was compiled from online databases such as OMIM (http://www.omim.org) and PubMed (http://www.ncbi.nlm.nih.gov/pubmed), as well as a comprehensive review of the current literature. The genes included in the panel are as follows: *ANOS1, AMH, AMHR2, AR, ARX, ATP6V0A4, ATRX, BCOR, CDKN1C, CHD7, CTU2, CUL4B, CYB5A, CYP11A1, CYP11B1, CYP17A1, CYP19A1, DHCR7, DHH, FEZF1, FGF8, FRAS1, FSHB, GATA4, GLI2, HOXA13, HSD17B3, HSD3B2, INPP5E, LHCGR, MAMLD1, MAP3K1, MYRF, NR0B1, NR2F2, NR3C1, NR5A1, NSMF, PAX6, PAX8, PBX1, POR, RPL10, RSPO1, SAMD9, SEMA3E, SGPL1, SOX10, SOX9, SRY, STAR, TCF12, TOE1, TWIST2, WT1, TTC21B, TTC8, UBR1, WDPCP, WDR11, WDR35, ZMYND10, AAAS, POMC, MCM4.*

2.6. Genetic Analysis Findings

Comprehensive genomic evaluation revealed no pathogenic or likely pathogenic variants in known DSD-associated genes that could explain the patient's phenotype. To investigate the origin of the observed complex translocation, we performed conventional karyotyping of first-degree relatives. Parental analysis demonstrated normal chromosomal constitutions in both progenitors (mother: 46,XX; father: 46,XY), while the sibling (46,XY) similarly showed no evidence of the translocation (Figures 3-5). This familial cytogenetic pattern confirms the de novo occurrence of the complex chromosomal rearrangement in the proband.

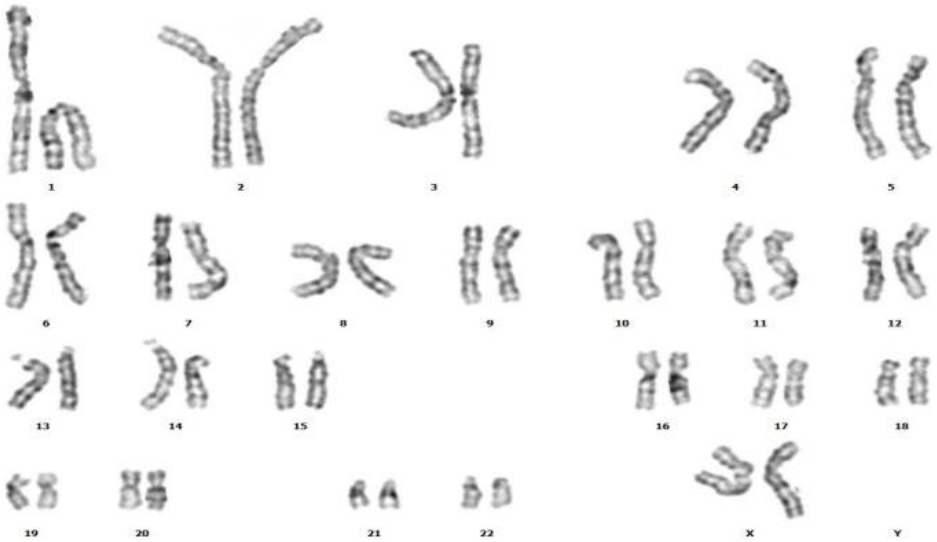

Figure 3. Karyotype analysis of the patient's mother was performed using the standard GTG banding (Giemsa-Trypsin-Giemsa) method. As a result of the analysis, a normal female karyotype with a chromosomal structure of 46,XX was detected.

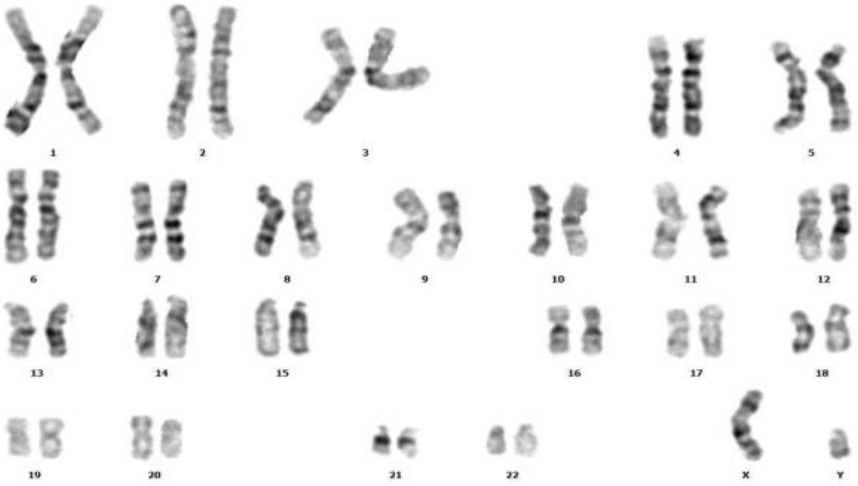

Figure 4. Karyotype analysis of the patient's father was performed using the standard GTG banding (Giemsa-Trypsin-Giemsa) method. As a result of the analysis, a normal male karyotype with 46,XY chromosomal structure was detected.

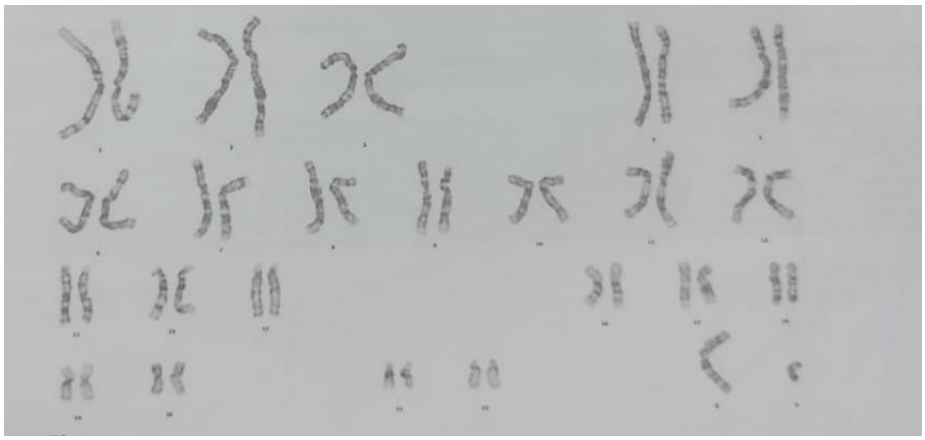

Figure 5. Karyotype analysis of the patient's brother was performed using the standard GTG banding (Giemsa-Trypsin-Giemsa) method. The analysis revealed a normal male karyotype with a 46,XY chromosomal structure.

The patient underwent laparoscopic-assisted total urogenital mobilisation to correct ambiguous genitalia and improve urinary function. After this procedure, both urinary functions and cosmetic results were significantly improved (Figure 6).

Figure 6. The patient underwent laparoscopic-assisted total urogenital mobilisation surgery at 8 months of age. This surgery involves repositioning and mobilisation of the urogenital system (urinary and reproductive organs). The images taken 1 year after the surgery showed that the healing process of the genital organs was successfully completed, and the normal anatomical structure was restored. This indicates that the surgical intervention was successful and the patient's recovery process is progressing favourably.

3. Results and Discussion

Our 7 months and 26 days old patient with chromosome 46,XY presented with complaints of ambiguous genitals and difficulty urinating. Investigation and management of a child with 46,XY genetic male sex and ambiguous genitalia is quite difficult. History and clinical examination stand out as the most basic and effective methods of diagnosing DSD cases [**6**]**.** The patient's history, physical

findings, and clinical symptoms should be carefully assessed. However, additional diagnostic methods may be required to make a definitive diagnosis. At this point, karyotype analysis is of great importance as it clearly shows the chromosomal structure and identifies abnormalities in the sex chromosomes (e.g., 46,XX; 46,XY or mosaic structures) [**6**]**.** Although translocations are rare in DSBs, the dosage of affected genes in the translocated chromosome influences the phenotype of the translocation. Karyotype analysis showed that the karyotype of our patient with DSB was 46,XY,t(1;2;12;6;16)(q42;q23;q22;q22;q13;q13). The diagnosis was confirmed by FISH. Such CCRs are structural chromosomal abnormalities that are extremely rare in the population and are usually characterised by the involvement of two or more chromosomes containing at least two breakpoints; in their simplest form, such rearrangements involve three breakpoints, while more complex cases may involve eight or more breakpoints. This wide variation results in CCRs showing a great genetic and clinical diversity [**7**]**.** The substantial prevalence of CCRs (approximately 23%) among individuals with multiple congenital anomalies and/or intellectual disability underscores their diagnostic relevance in clinical genetics. Notably, the observation that >50% of de novo CCRs are associated with abnormal phenotypes strongly implicates unbalanced chromosomal rearrangements as a frequent contributor to developmental pathology [**7-10**]**.** In our case, de novo CCRs were reflected in the phenotype as an undetermined sex anomaly.

The patient with a 46,XY karyotype shows a complex multiple translocation in the form of t(1;2;12;6;16)(q42;q23;q22;q13;q13). When the clinical significance of these translocations is compared with the data in the literature, it is seen that they are particularly associated with neurological, psychiatric, and developmental disorders. Cytogenetic disruptions at 1q42 represent a recognized genetic risk architecture for neuropsychiatric disorders, with balanced translocations in this locus demonstrating phenotypic penetrance across cognitive and behavioral domains [**11-15**]**.** Clinical findings of Robinow syndrome were found in two patients with a 1q42 deletion. These findings include phenotypic features, including short stature, hypertelorism, short limbs, and hypoplastic genital organs [1**6**]**.** The 2q23.1 microdeletion syndrome has been documented in 18 reported cases, with a consistent phenotypic spectrum encompassing intellectual disability, severe speech impairment, epilepsy, and behavioral abnormalities. Additional clinical hallmarks include microcephaly, subtle craniofacial dysmorphism, brachydactyly, postnatal growth restriction, and a wide-based ataxic gait, suggesting a distinct neurodevelopmental disorder associated with this genomic region [**17**]**.** Balanced translocations of chromosome 6 have been reported to be associated with reproductive failure [**18**]**.** This indicates that the translocation may lead to problems in meiotic segregation as a consequence of the rearrangement of genetic material. Chromosome 16q translocations have been linked to various physical and developmental disorders, including postnatal growth retardation, marked psychomotor retardation, dysmorphic facial features, flexion contractions of joints, foot deformities, congenital heart defects, ambiguous genitalia, hypospadias, small penis, bifid scrotum, undescended testes, intestinal malformations, and anorectal abnormalities [**19-20**]**.** Such findings suggest that the translocations observed in our patient may have clinical significance in terms of neurological, psychiatric, and developmental disorders. Additional clinical correlation studies and functional genomic analyses are needed to determine the exact phenotypic consequences of these complex translocations.

Sexual development in 46,XY individuals is controlled by a critical network of regulatory genes that orchestrate gonadal differentiation and genital morphogenesis. Disruption of these genes, through deletions, pathogenic variants, or dysregulation, can result in a wide range of phenotypes, from isolated hypospadias to complete sex reversal. Because of this genetic complexity, we used next-generation sequencing (NGS) to analyze a comprehensive panel of DSD genes, including the central SRY locus, to elucidate potential molecular etiologies in this case. The analysis revealed no pathogenic or significant mutations in the genes included in the panel. This finding suggests that the genetic causes of the patient's abnormalities of sex development should be further investigated.

4. Conclusion

Taken together, these findings suggest that 46,XY DSD is a phenotypically and genetically heterogeneous disorder that requires systematic genomic characterization combined with long- term multidisciplinary follow-up to improve prognostic accuracy and personalized interventions. While radiologic imaging, hormonal analysis and genetic testing are indispensable tools in the diagnosis of DSD, providing critical information about the underlying pathology, the phenotypic variability associated with chromosomal rearrangements further emphasizes the importance of comprehensive clinical and genetic evaluation. By integrating these diagnostic modalities, clinicians can optimize patient care and provide informed guidance to families, ultimately improving outcomes for individuals with this complex disorder.

Ethical statement:

The study was approved by the Medical Ethics Committee. Dicle University Faculty of Medicine Ethics Committee. (Ethics approval code: 125 / Date: 06.02.2020)

Acknowledgements:

No acknowledgements were declared.

Conflict of interest:

The authors declare no conflicts of interest.

Authors' Contributions:

All authors collaboratively reviewed and analyzed the clinical findings and karyotype results of the case.

Generative AI statement

The author(s) declare that no Gen AI was used in the creation of this manuscript.

References

[1] Losa, A., Da Silva Cardoso, J., Leite, S., Barros, A.C., Guedes, A., Rodrigues, C., Borges, T., Oliva-Teles, N., Soares, A.R., Mota, C., "Ambiguous genitalia: an unexpected diagnosis in a newborn", *Cureus*,15(10),2023. Doi: 10.7759/cureus.46328.

[2] Ferdinands, D.S., De Silva, S., Hewage, A.S., Atapattu N., "Variants in SRY and NR5A1 Genes in Sri Lankan children with 46, XY disorders of sex development: insights into mutation spectrum and diagnostic potential", *Egyptian Journal of Medical Human Genetics*, 26(90),2025. Doi: 10.1186/s43042-025-00725-4.

[3] Lee, P.A., Nordenström, A., Houk, C.P., Ahmed, S.F., Auchus, R., Baratz, A., Dalke, K., Liao, L.M., Lin-Su, K., Looijenga, L.H. 3rd, Mazur, T., Meyer-Bahlburg, H.F., Mouriquand, P., Quigley, C.A., Sandberg, D.E., Vilain, E., Witchel, S., Global DSD Update Consortium. "Global disorders of sex development update since 2006: perceptions, approach and care", *Hormone Research in Pediatrics*, 85(3),158-80,2016. Doi: 10.1159/000442975.

[4] Cools, M., Birgit Köhler., "Disorders of sex development", in: *Brook's Clinical Pediatric Endocrinology (*Ed. M. T. Dattani and C. G. D. Brook), NJ, John Wiley & Sons, 2019, ch 4., pp. 105-131, 2019. https://doi.org/10.1002/9781119152712.ch4

[5] Bozkaya, Ö.G. "Pediatrik Genetik", *Dokuz Eylül Üniversitesi Tıp Dergisi*, 22(3),171-9,2008.

[6] Richards, S., Aziz, N., Bale, S., Bick, D., Das, S., Gastier-Foster, J., Grody, W. W., Hegde, M., Lyon, E., Spector, E., Voelkerding, K., Rehm, H. L., & ACMG Laboratory Quality Assurance Committee, "Standards and guidelines for the interpretation of sequence variants: a joint consensus recommendation of the american college of medical genetics and genomics and the association for molecular pathology", *Genetics in medicine : official journal of the American College of Medical Genetics*, 17(5), 405–424, 2015. Doi: 10.1038/gim.2015.30

[7] Ahmed, S.F., Alimusina, M., Batista, R.L., Domenice, S., Lisboa Gomes, N., McGowan, R., Patjamontri, S., Mendonca, B.B. "The Use of Genetics for Reaching a Diagnosis in XY DSD", *Sexual Development,* 16 (2-3), 207-224, 2022. Doi: 10.1159/000524881.

[8] De Gregori, M., Ciccone, R., Magini, P., Pramparo, T., Gimelli, S., Messa, J., Novara, F., Vetro, A., Rossi, E., Maraschio, P., Bonaglia, M. C., Anichini, C., Ferrero, G. B., Silengo, M., Fazzi, E., Zatterale, A., Fischetto, R., Previderé, C., Belli, S., Turci, A., … Zuffardi, O. "Cryptic deletions are a common finding in "balanced" reciprocal and complex chromosome rearrangements: a study of 59 patients", *Journal of medical genetics*, 44(12), 750–762, 2007. Doi:10.1136/jmg.2007.052787

[9] Tupler, R., Maraschio, P., Gerardo, A., Mainieri, R., Lanzi, G., Tiepolo, L. "A complex chromosome rearrangement with 10 breakpoints: tentative assignment of the locus for Williams syndrome to 4q33--- q35.1",*Journal of medical genetics*, 29(4):253-5,1992. Doi: 10.1136/jmg.29.4.253.

[10] Ruiz, C., Grubs, R. E., Jewett, T., Cox-Jones, K., Abruzzese, E., Pettenati, M. J., Rao, P. N. "Prenatally diagnosed de novo apparently balanced complex chromosome rearrangements: two new cases and review of the literature". *American journal of medical genetics*, 64(3), 478–484,1996. Doi: 10.1002/(SICI)1096-8628(19960823)64:3<478::AID-AJMG6>3.0.CO;2-L.

[11] Madan, K., Nieuwint, A.W., van Bever, Y., "Recombination in a balanced complex translocation of a mother leading to a balanced reciprocal translocation in the child. Review of 60 cases of balanced complex translocations", *Human Genetics*, 99(6):806-15, 1997. Doi: 10.1007/s004390050453.

[12] Xu, F., Wei, F., Grommisch, B., Zhang, H. Z., Li, P.," Concomitant 1q42. 13-q44 Duplication and 14q32. 33 Deletion: A Case Report and Review of Literature". *North American Journal of Medicine and Science*, 10(2), 2017. Doi: 10.7156/najms.2017.1002056.

[13] Luo, A., Cheng, D., Yuan, S., Li, H., Du, J., Zhang, Y., Yang, C., Lin, G., Zhang, W., Tan, Y.Q., "Maternal interchromosomal insertional translocation leading to 1q43-q44 deletion and duplication in two siblings". *Molecular Cytogenetics*, 4,11-24, 2018. Doi: 10.1186/s13039-018-0371-7.

[14] Blackwood, D.H., Fordyce, A., Walker, M.T., St Clair, D.M., Porteous, D.J., Muir W.J. "Schizophrenia and affective disorders--cosegregation with a translocation at chromosome 1q42 that directly disrupts brain-expressed genes: clinical and P300 findings in a family". *The American Journal of Human Genetics*, 69(2),428-33, 2001. Doi: 10.1086/321969.

[15] Deutsch, S. I., Burket, J. A, Rosse, R. B, Schwartz, B. L. "Genetic variation of chromosome 1q42: etiologic mechanism of congenital disorders of neuronal migration and synaptogenesis", *Current Psychiatry Reviews*, 5(4), 236-249, 2009.

[16] Silipigni, R., Monfrini, E., Baccarin, M., Giangiobbe, S., Lalatta, F., Guerneri, S., Bedeschi, M.F., "Familial Duplication/Deletion of 1q42.13q43 as Meiotic Consequence of an Intrachromosomal

Insertion in Chromosome 1." *Cytogenetic and Genome Research*, 153(2):73-80, 2017. Doi: 10.1159/000485226.

[17] Mazzeu, J.F., Krepischi-Santos, A.C., Rosenberg, C., Szuhai, K., Knijnenburg, J., Weiss, J.M., Kerkis, I., Mustacchi, Z., Colin, G., Mombach, R., Pavanello Rde, C., Otto, P.A., Vianna-Morgante, A.M., "Chromosome abnormalities in two patients with features of autosomal dominant Robinow syndrome". *American Journal of Human Genetics*, 1(15),1790-5, 2007.Doi: 10.1002/ajmg.a.31661.

[18] Talkowski, M. E., Mullegama, S. V., Rosenfeld, J. A., van Bon, B. W., Shen, Y., Repnikova, E. A., Gastier-Foster, J., Thrush, D. L., Kathiresan, S., Ruderfer, D. M., Chiang, C., Hanscom, C., Ernst, C., Lindgren, A. M., Morton, C. C., An, Y., Astbury, C., Brueton, L. A., Lichtenbelt, K. D., Ades, L. C., … Elsea, S. H., "Assessment of 2q23.1 microdeletion syndrome implicates MBD5 as a single causal locus of intellectual disability, epilepsy, and autism spectrum disorder", *American Journal of Human Genetics*, 89(4),551-63, 2011. Doi: 10.1016/j.ajhg.2011.09.011.

[19] Yang, X., Zhang, H., Yu, Y., Zhu, H., Hu, X., Jiang, Y., Wang, R., Liu, R., "Clinical Features of Chromosome 6 Translocation in Male Carriers: A Report of 10 Cases and Review of the Literature" *Medical science monitor : international medical journal of experimental and clinical research*, 24, 4162–4168, 2018. Doi:10.12659/MSM.

[20] Laus, A. C., Baratela, W. A., Laureano, L. A., Santos, S. A., Huber, J., Ramos, E. S., Rebelo, C. C., Squire, J. A., Martelli, L. "Karyotype/phenotype correlation in partial trisomies of the long arm of chromosome 16: case report and review of literatüre", *American journal of medical genetics. Part A*, 158A(4), 821–827, 2012. Doi:10.1002/ajmg.a.32988

Middle East Journal of Science

https://dergipark.org.tr/mejs **MEJS**

e-ISSN:2618-6136

Review

DEEP LEARNING: EVOLUTION, INNOVATIONS, AND APPLICATIONS IN THE LAST DECADE

Mihriban GÜNAY*[1], Özal YILDIRIM[2], Yakup DEMİR[3]

[1]Munzur University, Department of Electrical and Electronics Engineering, Tunceli, Türkiye
[2] Fırat University, Department of Software Engineering, Elazığ, Türkiye
[3]Fırat University, Department of Electrical and Electronics Engineering, Elazığ, Türkiye
*Corresponding Author: mihribangunay@munzur.edu.tr

Abstract: *Deep learning has become a popular method in the last ten years with its superior performance in many fields, especially in health. Although it is a sub-branch of machine learning, one of the most important reasons for researchers to use this method is that it automates the difficult processes of feature extraction stages in traditional machine learning methods. With the advancement of technology every year, it has become easier to create large data sets or to access large data sets that have been used before on the web. Researchers who want to work on large data sets use deep learning methods effectively because of their advantages instead of using traditional machine learning methods. The foundations of deep learning were laid with the deep belief networks method, which was first developed in 2006. Later, with the significant success of the Convolutional Neural Network (CNN) method developed in 2012 in image classification, deep learning methods have been used in many applications in other disciplines. The success of the deep reinforcement learning algorithm that defeated Alpha Go champion Lee Sedol in 2016, the remarkable success of the contentious generating networks in creating their own unique images, the success of the Siamese networks with the ability to learn from little data in signature verification and facial recognition systems, the success of the artificial intelligence chat bot ChatGPT, which was launched in the last months of 2022, attracted attention in a short time, and the ability of DALL-E, a similar language model, to create images from texts, shows that deep learning is in constant innovation and development. This study aims to give an idea to researchers who will work in this field in the future by talking about the basic concepts of deep learning and the innovative and popular approaches used.*

Keywords*: Deep learning, deep networks, machine learning, artificial intelligence.*

Received: February 16, 2025 *Accepted: May 26,2025*

1. Introduction

Deep learning, a sub-branch of machine learning, is a popular method that automates the feature extraction stages in machine learning and combines them with classification. Deep learning tries to learn the features extracted from data by using the deep neural network architecture, which is inspired by the basic working logic of the feed-forward artificial neural network architecture. In order to get efficient results in deep learning, the amount of data must be large. Creating a large amount of dataset has become possible with the widespread use of the internet since 2000. This has been a preliminary step for deep learning.

The concept of deep learning was first introduced in 2006 with the deep belief network introduced by Hinton et al. [1]. After this development in 2006, studies and research on deep learning have spread rapidly worldwide. Many world-famous companies have closely followed the developments in deep

learning and have made certain initiatives. Famous companies such as Google, Facebook and Microsoft have invested in deep learning and applied deep learning to various areas. Later, Microsoft and Google achieved great success by significantly reducing the error rate in speech recognition studies using deep neural networks [2].

There are two important years in the literature that affected the rise of deep learning: 2012 and 2016. In 2012, the high performance of AlexNet, a deep neural network model designed by Alex Krizhevsky, in classifying images in the ImageNet large-scale visual recognition (ILSVRC) competition [3] accelerated deep learning studies. In 2016, deep learning research took a big leap forward when the AlphaGo program developed by Google Deepmind defeated human champion Lee Sedol in the Go competition [4]. As a result of the high performance achieved in the Go competition, deep learning managed to attract the attention of many researchers. The increasing interest of researchers in deep learning and their efforts to apply deep learning to different fields contributed to the popularity and development of the method.

In the last five years, deep learning methods have been used mostly in the health field. In the health field, it has been used mostly in cancer detection [5], [6], heart disease detection [7], [8] and brain tumor classification [9], [10], [11]. Since 2020, it has played a vital role in the preliminary detection of the novel coronavirus (Covid-19) disease [12], [13]. Deep learning has been used in many academic studies outside the health field. These are: natural language processing [14], object recognition [15], gaming [16], finance [17], etc. Today, researchers prefer deep learning methods instead of traditional machine learning methods in many fields. There are three main reasons for this. These are: the widespread use of GPUs in education with the development of technology, the increase in the amount of data, and the elimination of the need for feature engineering for feature extraction stages.

This study aims to provide a comprehensive overview of the evolution of deep learning in the last decade, highlighting its foundational concepts, model innovations, and wide-ranging applications. By presenting key architectural developments such as CNNs, LSTMs, GANs, and transformers, as well as emerging areas like geometric deep learning and explainable AI, this study serves as a valuable reference for researchers aiming to explore or apply deep learning techniques. The remainder of this paper is organized as follows: Section 2 discusses the technical foundations and major architectures in deep learning. Section 3 presents the ethical and societal implications of deep learning technologies. Section 4 includes a discussion of current limitations and emerging research trends. Finally, Section 5 concludes the study by summarizing the contributions and emphasizing the future potential of deep learning.

2. Deep Learning

Deep learning is a fast and effective method that minimizes human intervention as much as possible by using a multilayered nonlinear network structure. The roots of deep learning date back to the beginning of the artificial neural network era, which developed with the emergence of the backpropagation algorithm. Research on artificial neural networks began in the 1940s. In 1943, McCulloch and Pitts analyzed the operating characteristics of neurons in the brain and proposed a model called McCulloch-Pitts (MP) [18]. This proposed model made significant contributions to the development of artificial neural networks. Later, Hubel and Wiesel's study on multilayer perceptrons by examining the animal cerebral cortex [19] created an important idea for the use of layered architecture in artificial neural networks in the following years.

The backpropagation algorithm, which had the greatest impact on the beginning of the artificial neural network era, was developed in the 1960s and 1970s and was first applied to neural networks in 1981. A classical neural network consists of an input, an output, and at least one intermediate layer called the hidden layer. Unlike classical neural networks, the number of hidden layers is high in the neural network structure used in deep learning. The deep neural network architecture is given in

Figure 1. Since the number of hidden layers adds depth to the network, the neural network structure used in deep learning is called a deep neural network. Deep learning is more complex models than classical machine learning methods due to the higher number of hidden layers. These complex models used in deep learning can increase classification accuracy and reduce errors in regression problems, provided that there are sufficiently large data sets. The purpose of deep learning is to ensure that all feature extraction stages from low-level features of a raw data to high-level features are performed automatically.

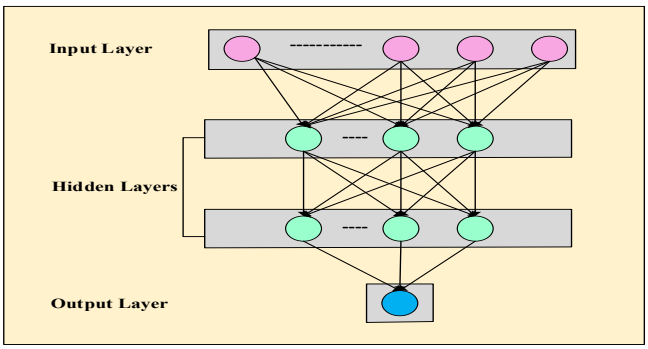

Figure 1. Deep neural network architecture.

2.1. Convolutional Neural Networks (CNN)

Convolutional neural networks (CNN) are feedforward artificial neural networks inspired by biological neural networks and using convolution in at least one of their layers. The concept of CNN was first proposed by Fukushima in 1980 [20]. Later, in 1989, Lecun et al. [21] proposed the first multilayer CNN architecture called ConvNet, which was based on Fukushima's neocognitron. Lecun proposed supervised training for ConvNet using the backpropagation algorithm, compared to the unsupervised reinforcement learning algorithm used by Fukushima. The backpropagation algorithm greatly contributed to the development of the first CNN. Studies continued to develop CNN until 1998, and in 1998, a CNN architecture called LeNet was introduced [22]. This CNN architecture basically consists of convolution layers, pooling layers, and fully connected layers. Figure 2 shows a block representation of the basic CNN architecture. There are two new layers that distinguish CNN from a typical neural network. These layers are: convolution layer and pooling layer. This architecture is specifically designed to recognize two-dimensional data such as images and videos. In CNN, images can be used directly as input to the network. This feature eliminates the complex feature extraction and data reconstruction process in traditional image recognition algorithms.

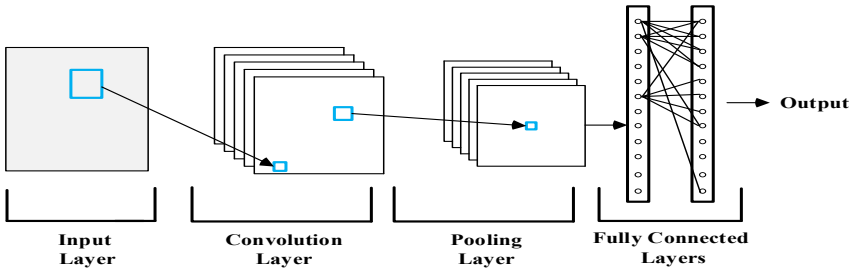

Figure 2. A basic CNN architecture.

In 1998, Lecun used the LeNet architecture in character classification on the MNIST dataset consisting of handwritten digits [22]. Until 2000, CNNs were not used much in other computer vision areas except for

character recognition studies. In 2006, with the increase in the computational power of Graphics Processing Units (GPUs), it became possible to train larger networks. With this development, the LeNet architecture was developed by different researchers and many new CNN models were created. The AlexNet architecture, which has a deeper structure designed after the LeNet architecture, broke new ground in image classification studies by classifying approximately 1.2 million images consisting of 1000 classes with high performance in the ImageNet (ILSVRC) competition held in 2012 [3]. In the literature, CNN architectures such as ZFNet [23], VGGNet [10], GoogleNet [24] and ResNet [11], which are deeper networks compared to AlexNet, have been proposed to improve the performance of AlexNet. These architectures differ from each other in terms of the number of layers. The ResNet model was the champion of the ILSVRC competition held in 2015. ResNet is an architecture that is 20 times deeper than AlexNet. Scientists who analyze the high performances achieved by CNN architectures have focused on designing new loss functions to improve both the performance and the current architectures. In recent years, CNN-based architectures have been successfully applied in the field of health, especially in the preliminary detection and classification of diseases [12], [13], [25], and outside the field of health, mostly in face recognition [26], [27], hyperspectral image classification [28], [29] , object detection and object tracking [30], [31], motion recognition [32] , and remote sensing [33], [34] .

2.2. Long Short-Term Memory (LSTM)

Recurrent neural networks (RNN) are one of the groundbreaking neural network architectures in the field of deep learning in recent years. RNN was first introduced by Rumelhart in 1986 [35]. RNN is a type of traditional feed-forward neural networks. The term “recurrent” in this neural network indicates that the same task is performed repeatedly for each element in the input sequence, and the output of each of these tasks plays a role in the overall prediction by the RNN. RNN is generally preferred in cases where the output depends on a series of inputs. Unlike traditional feed-forward neural networks, RNNs have memory. These neural networks use internal memory to process inputs given in the form of a series. In other deep learning methods other than RNN, computations on time series data have lower performance. For this reason, RNN is mostly preferred in studies involving time series data such as text, audio, video and activity classification [36]. The most commonly used RNN is LSTM. LSTM was introduced by Hochreiter and Schmidhuber in 1997 [37]. LSTM is the most popular RNN architecture to date, designed to solve the vanishing gradient problem of RNNs. RNNs cannot remember data for a long time due to the vanishing gradient problem. LSTMs use a more complex repetition function that allows remembering long-term dependencies than a normal RNN. LSTM has a strong ability to learn and predict sequential data. A basic LSTM architecture is shown in Figure 3. Unlike RNN, LSTM has four neural network layers. There is a forget gate, an output gate, and an update gate in the LSTM architecture given in Figure 3, which is shown with a forget gate (sigmoid function). In the first step, the forget gate decides which data is needed or not using the sigmoid function. In the second step, it is decided which data will be stored in the cell state and the vector of new candidate data is calculated. In the second step, the sigmoid function determines which data will be updated, while the tanh function creates a vector of new candidate data. In the third step, the cell status is updated. In the last step, the output is determined by the sigmoid function.

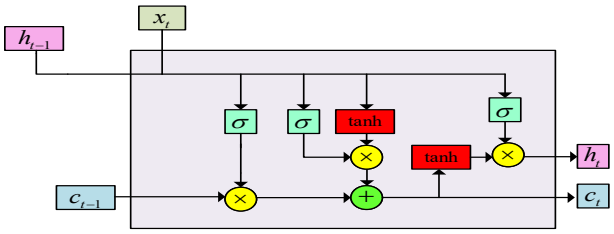

Figure 3. Basic LSTM architecture.

In recent years, LSTMs have been mostly used in human action recognition [38], sentiment analysis [39], [40], stock market price prediction [41], traffic flow prediction [42], weather prediction [43] and lithium-ion battery state of charge prediction [44].

2.3. Generative Deep Learning Architectures

Generative deep learning architectures are models that can generate new content from data such as images, text, audio, or video. DALL-E, deep fake, and Generative Adversarial Networks (GANs) are generative deep learning architectures that use different techniques to generate images from text or modify existing images.

DALL-E is a neural network developed by OpenAI that can generate images from text titles for a wide range of concepts that can be expressed in natural language [45]. DALL-E can create realistic and diverse images for a wide range of concepts, objects, scenes, and transformations. It can also control the features, viewpoints, and perspectives of the images [46].

Deep fake is a term that refers to synthetic media created using deep learning to replace the face or voice of a person in an existing image or video [47]. Deep fake can be used for a variety of purposes, such as entertainment, satire, or malicious intent. For example, deep fake can be used to create realistic videos of celebrities or politicians saying or doing things they never do. Deepfake can also be used to change the faces of actors in movies or to create realistic voice imitations [48]. GANs are deep learning-based generative network models proposed by Goodfellow in 2014 [49]. GAN architecture consists of two types of networks called generators and discriminators. GAN architecture was created by taking inspiration from a two-player game. In GAN, two players correspond to the generator and discriminator, respectively. A block representation of a basic GAN architecture is given in Figure 4. In GAN architecture, each network has a separate task in this game played between the generator network and the discriminator network. The task of the generator network is to create synthetic data similar to the data in the dataset and to ensure that the discriminator cannot distinguish synthetic data from real data. The task of the discriminator network is to determine whether a data is synthetic data or real data. GAN is easily trained by updating the generator and discriminator alternately using the backpropagation algorithm.

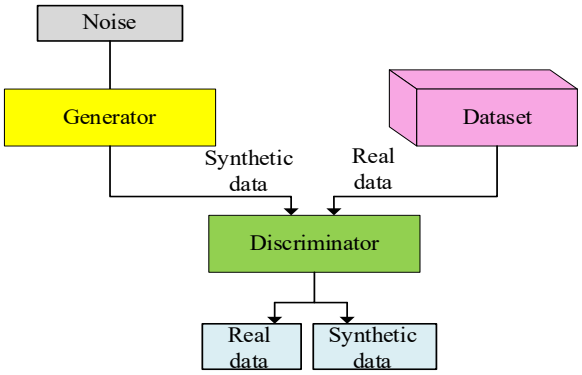

Figure 4. Block representation of a basic GAN architecture.

Since 2014, GAN has been developing and has attracted great attention in recent years, especially in the field of computer vision, in the fields of self-generating original images [46], [47], generating high-resolution images from low-resolution images [46], and image-to-image translation studies that transfer images to another specific area [50], and has managed to become one of the most successful generative models. In the last five years, GAN has been successfully applied to various areas outside the field of computer vision, such as speech and language processing [51], [52], malware detection [53],

and chess game [54]. Figure 5 shows real face images taken from the dataset named CelebaA and the fake face images successfully created by GAN after processing these face images.

Figure 5. Real face images taken from different sources. (a) Real face images from the CelebaA dataset, (b), (c) and (d) fake face images created by MMAs in different periods [55].

2.4. Deep Reinforcement Learning

Reinforcement learning was introduced in 1898 by Thorndike in an experimental study where he used a trial and error procedure to determine cat behavior [56]. Reinforcement learning [57] is a process that interacts with the environment and automatically learns to make the most appropriate decisions to reach the goal through trial and error. In the reinforcement learning architecture, the structure called the agent interacts with the environment and receives rewards or punishments as a result. Deep reinforcement learning is the use of deep models in reinforcement learning. For this reason, the agent structure in deep reinforcement learning consists of deep models, unlike reinforcement learning. A block representation of the basic deep reinforcement learning architecture is shown in Figure 6. In this architecture, the agent processes the state information it receives from the environment through a deep neural network and produces an appropriate action. The environment evaluates the action taken by the agent and provides it with reward feedback, which determines the new observed state of the system. The agent tries to optimize its interaction with its environment by updating the neural network parameters to maximize the rewards. Thanks to the advantages of deep neural networks in deep reinforcement learning, the learning process of complex and high-dimensional data is automatic, fast and efficient.

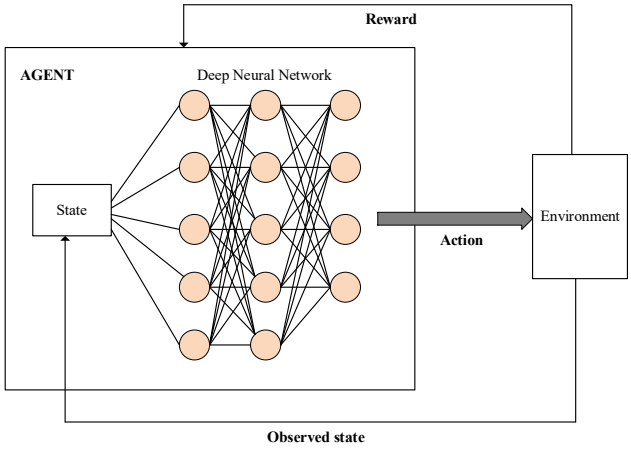

Figure 6. Block representation of the basic deep reinforcement learning architecture.

Deep reinforcement learning has begun to attract the attention of researchers as a result of its outstanding successes in computer games. Deep reinforcement learning outperformed a professional player in the classic Atari game in 2015, and this work has attracted great attention in the scientific world [27]. The AlphaGo program, developed by the Google DeepMind team using the deep reinforcement learning method, showed superhuman success by defeating the world Go champion Lee Sedol in 2016 and achieved global success [58]. Released in late 2022, ChatGPT, which uses both supervised and deep reinforcement learning and has attracted attention in a short time, is a powerful artificial intelligence chatbot developed by OpenAI that can generate images from text [59]. ChatGPT is a member of OpenAI's Generative Pre-trained Transformer (GPT) model series. GPT models are large language models based on the transformer architecture developed by Google. The transformative architecture is an architecture that can track the position, order, and hierarchy of all words in a sentence using attention mechanisms and can store large amounts of contextual information and produce grammatically and semantically meaningful texts. ChatGPT is a technology that pushes the boundaries of language models and raises new research questions. ChatGPT has inspired researchers to understand how language models can be better trained, evaluated, optimized, explained, and secured [60]. ChatGPT was built on the GPT-3.5 model in 2022 and transitioned to the GPT-4 model in 2023. While GPT-3.5 has 175 billion parameters, GPT-4 has 1 trillion parameters. This means that ChatGPT can process more data and produce more natural and diverse texts [61]. ChatGPT allows users to guide and optimize a conversation according to their desired length, format, style, level of detail, and language. In each chat phase, previous requests and responses are considered as a context and ChatGPT produces text in accordance with this context [29]. ChatGPT started as a chatbot and has been used in various applications in different fields over time. ChatGPT can be used in sectors such as education, health, entertainment, business, art, music, gaming, software development [62]. In recent years, deep reinforcement learning has been used in many interesting areas such as the online game Dota 2 [31], poker game [63], chess game [17], robotics [64], self-driving cars [65], chemical reaction optimization [66], recommendation systems [67].

2.5. Siamese Neural Networks

Another remarkable model used in the field of deep learning is Siamese networks. Siamese networks were first proposed by Bromley and LeCun in the 1990s for the signature verification problem [68]. Siamese Neural Networks are an architecture formed by combining subnetworks with the same parameters and weights [69]. The basic structure of the network is the combination of twin networks fed by two different inputs with an energy function. In order to find similarities in the input data, feature vectors are compared in the subnetworks. A block representation of a basic Siamese network architecture is given in Figure 7. In the Siamese network, two different input data are passed through neural networks with the same structure that share the same weights and parameters, resulting in two feature vectors. The difference between the feature vectors is found by means of a function, and the similarity rate between the two input data is found. According to the similarity rate, how similar the two input data are to each other is interpreted.

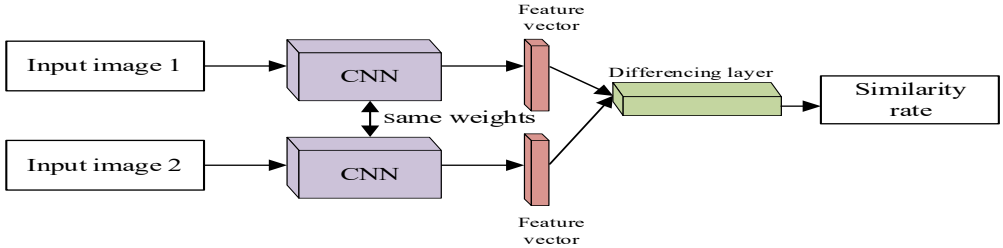

Figure 7. Block representation of the basic Siamese network architecture.

This architecture requires more training time than CNN architectures such as ResNet and AlexNet. However, it has the ability to learn with a smaller training set [70]. Siamese networks are now commonly used in tasks such as finding similarities and relationships between two similar objects and in verification systems. The ability to learn from small data has made Siamese networks popular, especially in signature verification [71] and face recognition [72] . Siamese networks are also used in areas such as classification [73], prediction and signal processing [74].

2.6. Capsule Networks

In the late 1990s, Geoffrey Hinton and his colleagues proposed capsule neural networks, which model the tree structure of data and the relationship between segmentation and recognition. Capsule networks are a member of OpenAI's GPT model series. The paper proposed an architecture in which a group of neurons called capsules encode the features and probabilities of an entity and are transferred to the next level capsules with an algorithm called dynamic routing. This architecture, unlike CNNs, can learn how parts of objects in images fit together as a whole and how they change from different perspectives [75]. A block representation of the basic capsule network architecture is given in Figure 8. In the convolution layer, as in CNNs, filters or kernels are used to create feature maps from the input data. In image processing tasks, convolution operations are applied on the input images to create feature maps in this layer. This layer helps detect specific features (edges, corners, etc.) in images. The primary capsule layer works on the outputs of the convolution layer. In this layer, the outputs of the convolution layer are converted into groups called capsules. Each capsule represents a particular feature. This layer helps in converting lower level features into higher level representations. The digit capsule layer takes the outputs of the primary capsule layer and is used to perform object recognition or classification tasks. In this layer, a mechanism called routing by agreement is used to model the relationships between capsules belonging to different classes. Each digit capsule represents a class and encodes the features of objects belonging to that class. This layer is usually terminated with an activation function such as softmax for classification, so that the probability of each capsule belonging to a particular class is calculated.

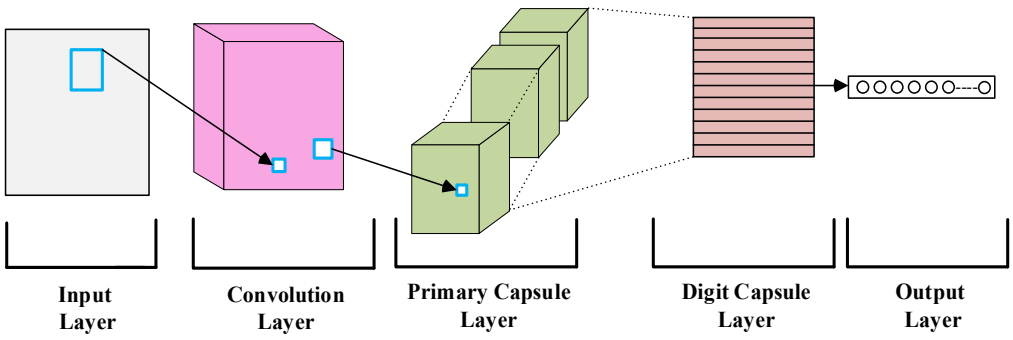

Figure 8. Block representation of the basic capsule network architecture.

Capsule networks have been used in various fields such as hyperspectral image processing, medical image processing, face image processing, text classification, object detection, image segmentation, few-sample learning [76]. In these fields, capsule networks have provided advantages such as higher accuracy, lower complexity, less data requirement, better noise tolerance, better transformation and scale change resistance compared to CNNs. It is expected that capsule networks will be used in more fields and applications in the future. Capsule networks are related and comparable to other AI models such as CNNs and transformers. Capsule networks can bring forth new problems,

opportunities, and solutions in AI research. Capsule networks can contribute to the development and widespread use of AI [77].

2.7. Geometric Deep Learning

Geometric deep learning is a research field that generalizes deep learning methods to model and exploit the underlying geometric structures of data [78]. Geometric deep learning attempts to explain different aspects of data using concepts such as grid, group, graph, geodesic, and indicator. In the 2000s, with the explosion of deep learning, geometric deep learning has also developed in various methods [79]. Geometric deep learning has become popular by achieving significant results in many application areas such as computer vision, natural language processing, chemistry, biology, and social network analysis [80]. Applications of geometric deep learning can be seen wherever the geometric structure of data is important or useful. For example, in computer vision, geometric deep learning has been used in many areas such as image classification, object recognition, face recognition, image synthesis, image retrieval, image shifting, image segmentation, video analysis, 3D image processing, computed tomography, medical imaging, and biometric recognition [79]. In natural language processing, geometric deep learning has been used in areas such as word embeddings, text classification, text summarization, text generation, machine translation, sentiment analysis, question-answer systems, dialogue systems, and information extraction [81]. In chemistry, geometric deep learning has been used for modeling and prediction of molecular structures, properties, interactions, and reactions [82]. In biology, geometric deep learning has been used for protein structure, function, folding, binding, interaction, and evolution [83]. In social network analysis, geometric deep learning has been used to analyze the structure, dynamics, communities, propagation, influence, and security of social networks [84]. The future of geometric deep learning seems bright from both theoretical and applied perspectives. Figure 9 summarizes the variety and applications of different data structures such as grids, groups, graph structures, and geodesics used in geometric deep learning.

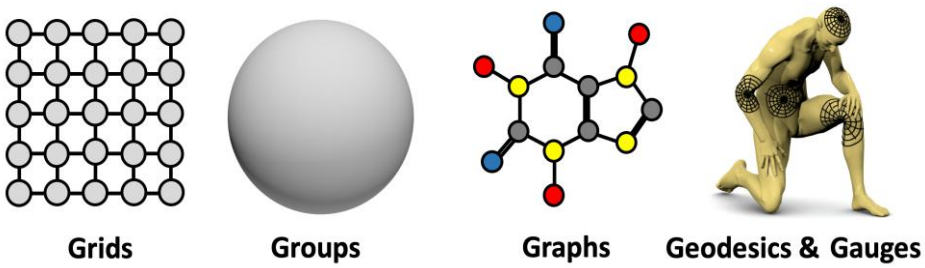

Figure 9. 5G of Geometric Deep Learning: grids with spherical symmetry, groups and homogeneous spaces, graphs, geodesics on manifolds, and metrics and indicators [78].

Geometric deep learning offers an opportunity to better understand the fundamental mathematical principles and physical realities of deep learning. Geometric deep learning provides a means to improve the performance, robustness, efficiency, interpretability, and expressiveness of deep learning models.

2.8. Vision Transformers

Vision transformers are a model that uses a transformer-like model for image processing tasks. Vision transformers have gained popularity in recent years due to their performance equal to or better than that of CNN in many computer vision tasks such as image classification [85]. The evolution of vision transformers dates back to a history as old as transformers themselves.

Transformers emerged in the 2017 paper titled “Attention is all you need” [86]. Transformers are a deep learning model that adopts a self-attention mechanism that weights the importance of each piece of input data differently. Transformers have become the preferred model for natural language processing problems in recent years, replacing CNN models such as LSTM [87].

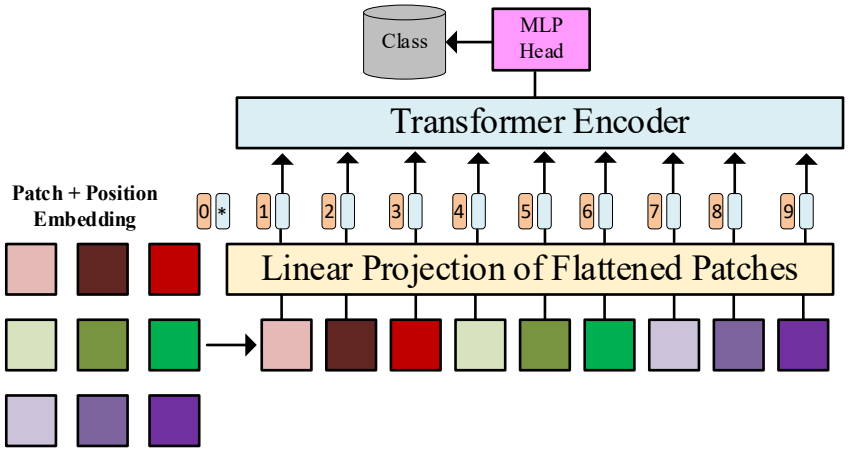

Figure 10. Image transformer architecture.

Figure 10 shows the basic structure of the vision transformer architecture. The image is first divided into fixed-size patches, each patch is flattened, and linear projection is applied to transform it into a series of vectors. Position information is added to these vectors to obtain “Patch + Position Embedding”, and then these vectors are sent to the Transformer Encoder layer. Transformer Encoder learns the relationships between these patches using the attention mechanism and combines the visual information. Finally, classification is performed using a Multi-Layer Perceptron (MLP) head. Vision transformers exhibit quite successful performance in image classification by considering the contextual relationships between the patches of the images.

Vision transformers use a self-attention mechanism that weights the importance of each patch of the image differently. This allows to better capture the relationships between different regions of the image and model long-range dependencies. CNN uses kernels to capture local features, but requires a large number of layers to establish connections between distant regions [88]. Vision transformers use location embedding to encode the location and orientation of the data while preserving the grid structure of the image. This makes image converters robust against operations such as transformation, scaling, reflection, etc. CNN has less location sensitivity compared to image converters, but requires more parameters [89]. Image converters generalize and simplify the converter architecture for image processing. Image converters use fewer layers, fewer operations, and fewer hyperparameters compared to CNN. Geometric concepts such as grid, group, graph, geodesic, and gauge are used in image converters to describe different aspects of image data [90].

2.9. Explainable Deep Learning Approaches

Explainable Deep Learning Approaches are a research area developed to better understand and interpret the decisions and decision-making processes of deep learning models [91]. Explainable Deep Learning Approaches have gained popularity recently because deep learning models need to be understandable and reliable by humans when used in critical areas such as healthcare, law, finance and security.

Explainable Deep Learning Approaches are useful for many real-world needs and applications such as model validation, model debugging and model discovery [91]. Model validation is used to

evaluate whether the model behaves as intended in the real world. Model debugging is used to reveal hidden biases or deficiencies of the model and find solutions. Model discovery is used to discover the hidden capabilities or potentials of the model [92].

Explainable Deep Learning Approaches show which parts of the input the model pays attention to, which features it learns, which factors affect the predictions and what evidence it provides [93]. Explainable Deep Learning Approaches provide an opportunity to better understand the underlying mathematical principles and physical realities of deep learning models. Explainable Deep Learning Approaches explain how the model uses the underlying concepts of the data, such as geometric, group, graph, geodesic, and gauge [94].

Explainable Deep Learning Approaches provide a means to increase the performance, robustness, efficiency, interpretability, and expressiveness of deep learning models [94]. Explainable Deep Learning Approaches provide a path to increase the scope, diversity, impact, and value of deep learning applications. Explainable Deep Learning Approaches offer a vision to push the boundaries of deep learning and solve new problems.

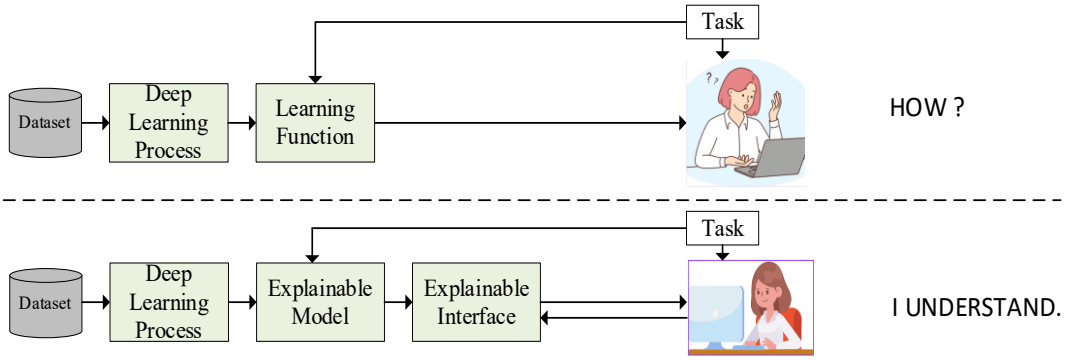

Figure 11. Explainability approach in deep learning models.

Figure 11 shows how deep learning processes are addressed with two different approaches in terms of explainability. In the upper part of the figure, it is emphasized that the deep learning process produces results through a learning function, but the decision mechanism in this process may be incomprehensible to the user. This structure, where the user asks the question “How?”, represents the nature of classical deep learning models that lack explainability. In the lower part, it is seen that an explainable deep learning model provides reliability and understanding to the user by providing not only a result but also a comprehensible explanation. The explainable model and interface involve the user in the process and enable them to reach the conclusion “I understand.” In this way, explainable deep learning makes it easier for users to understand the decision mechanisms of the model.

Explainable Deep Learning Approaches have been used in many fields such as natural language processing, chemistry, biology, social network analysis. In natural language processing, Explainable Deep Learning Approaches have been used in areas such as word embedding, text classification, text summarization, text generation, machine translation, sentiment analysis, question-answer systems, dialogue systems, and knowledge extraction [95]. In chemistry, Explainable Deep Learning Approaches have been used for modeling and prediction of molecular structures, properties, interactions, and reactions [96]. In biology, Explainable Deep Learning Approaches have been used for protein structure, function, folding, binding, interaction, and evolution [97]. In social network analysis, Explainable Deep Learning Approaches have been used to analyze the structure, dynamics, communities, spread, influence, and security of social networks [98].

3. Ethical and Societal Implications of Deep Learning

Deep learning has revolutionized various industries, including healthcare, finance, and autonomous systems, enabling significant advancements. However, as these models become integrated into daily life, they bring ethical concerns and societal implications. The widespread use of deep learning raises critical questions regarding bias, fairness, privacy, security, and its impact on the workforce. Addressing these issues is essential to ensuring that deep learning models serve humanity responsibly and equitably.

One of the major ethical concerns in deep learning is bias and fairness. Many deep learning models inherit biases from the large datasets they are trained on, leading to discriminatory outcomes [99]. For example, facial recognition systems have been found to exhibit lower accuracy for individuals with darker skin tones due to imbalanced training data. Similarly, AI-driven hiring systems have shown gender biases, favoring male candidates over female applicants based on historical employment data [100]. Such biases can reinforce existing societal inequalities and undermine trust in AI systems [101]. Researchers are working on techniques such as algorithmic fairness, diverse dataset curation, and bias auditing to mitigate these risks. Ensuring fairness in deep learning models requires continuous efforts to identify and rectify biases throughout the development process.

Privacy and security concerns also pose significant challenges in deep learning applications. Many AI models rely on extensive user data, raising concerns about data misuse and surveillance. For instance, large-scale language models collect vast amounts of text data, potentially exposing sensitive user information. Additionally, adversarial attacks on deep learning models can manipulate outputs, leading to security vulnerabilities in applications such as autonomous driving and medical diagnostics [102]. To counter these threats, privacy-preserving AI techniques such as federated learning and differential privacy are being developed. These methods enhance data security while maintaining model performance, ensuring that AI systems respect user confidentiality.

The impact of deep learning on the job market is another pressing issue. AI-powered automation is transforming industries by replacing repetitive and routine tasks with machine-driven solutions, resulting in job displacement, particularly in sectors such as manufacturing, customer service, and finance. However, deep learning also creates new opportunities, such as AI ethics consulting, machine learning engineering, and AI model auditing. To adapt to these changes, governments and institutions must invest in workforce reskilling programs, equipping individuals with the skills needed to thrive in an AI-driven economy [103].

Ensuring responsible AI development is essential for addressing these ethical and societal challenges. Explainable AI (XAI) is a growing field focused on making deep learning models more transparent and interpretable. Traditional deep learning models often operate as "black boxes," making it difficult to understand how decisions are made. By developing techniques that provide insights into model behavior, researchers can increase trust in AI systems and enable users to verify decisions. Additionally, regulatory frameworks and ethical guidelines must be established to govern AI applications [104]. Organizations such as the European Union and OpenAI are already working on policies that promote AI transparency, accountability, and fairness.

Looking ahead, the future of deep learning presents both opportunities and challenges. While AI has the potential to enhance human capabilities and solve complex problems, it must be developed with ethical considerations in mind. The rise of Artificial General Intelligence (AGI) further complicates ethical discussions, as models surpassing human intelligence may pose unforeseen risks [105]. Researchers, policymakers, and industry leaders must collaborate to ensure that deep learning technologies align with societal values and contribute positively to the world.

In conclusion, deep learning is a powerful tool with far-reaching implications. Addressing issues related to bias, privacy, security, and employment is crucial to fostering responsible AI deployment. By prioritizing fairness, transparency, and accountability, the AI community can build trust in deep learning systems and harness their potential for the benefit of all.

4. Discussion

Deep learning has achieved significant advancements across various domains, yet challenges remain. A key issue is the reliance on large labeled datasets, which can be costly and raise privacy concerns. Techniques like self-supervised and federated learning aim to address this by reducing dependency on extensive labeled data.

Computational complexity also poses limitations, making deep learning models resource-intensive. Efficient architectures, pruning, and quantization techniques can help mitigate these constraints. Another concern is the lack of interpretability, which hinders deployment in critical areas. Explainable AI (XAI) methods are being developed to increase model transparency and trust.

Security vulnerabilities, such as adversarial attacks, threaten the reliability of deep learning models. Robust training techniques and defense mechanisms are being explored to enhance resilience. Additionally, ethical concerns like algorithmic bias and job displacement require proactive solutions, including bias mitigation and responsible AI policies.

Despite these challenges, the future of deep learning is promising. Advances in geometric deep learning, reinforcement learning, and self-supervised methods will further expand AI capabilities. Addressing these issues will ensure deep learning continues to drive innovation and positive societal impact.

5. Conclusion

Deep learning methods have shown rapid development with the increase in data amounts due to advances in technology. Nowadays, many deep learning methods have been developed to solve various complex problems. In this study, general information about the concept of deep learning and its historical development is provided. Then, information is given about the popular models of deep learning that have achieved significant success in recent years, such as CNN, LSTM, Generative deep learning architectures, deep reinforcement learning, Siamese neural networks, capsule networks, geometric deep learning, vision transformers, explainable deep learning, and GANs. The historical development of these deep learning models is examined, and studies demonstrating their high performance are discussed. Additionally, a detailed review was conducted on the popular application areas of each model over the last decade. Finally, the ethical and societal implications of deep learning were discussed. This study provides information to researchers about method selection based on problem types and highlights the latest innovations in deep learning.

Ethical statement

The authors declare that this document does not require ethics committee approval or any special permission. This review does not cause any harm to the environment and does not involve the use of animal or human subjects.

Conflict of interest

The author declares no conflict of interest.

Authors' Contributions

M. G: Conceptualization, Methodology, Formal analysis, Writing - Original draft preparation

Ö. Y: Resources, Investigation, Formal analysis.
Y. D: Resources, Investigation, Formal analysis.
All authors read and approved the final manuscript.

Generative AI statement

The author(s) declare that no Gen AI was used in the creation of this manuscript.

References

[1] Hinton, G. E., Osindero, S., Teh, Y. W., "A fast learning algorithm for deep belief nets", *Neural Computation*, 18(7), 1527–1554, 2006.

[2] Hao, X., Zhang, G., "Technical survey deep learning", *International Journal of Neural Systems*, 10(3), 417–439, 2016.

[3] Krizhevsky, A., Sutskever, I., Hinton, G. E., "ImageNet classification with deep convolutional neural networks", *Advances in Neural Information Processing Systems*, 25, 1097–1105, 2012.

[4] Koch, C., "How the computer beat the Go player", *Scientific American Mind*, 27(4), 20–23, 2016.

[5] Khan, S., Islam, N., Jan, Z., Din, I. U., Rodrigues, J. J. P. C., "A novel deep learning based framework for the detection and classification of breast cancer using transfer learning", *Computers in Biology and Medicine*, 125, 1–6, 2019.

[6] Yıldırım, Ö., Pławiak, P., Tan, R., Acharya, U. R., "Arrhythmia detection using deep convolutional neural network with long duration ECG signals", *Computers in Biology and Medicine*, 102, 411–420, 2018.

[7] Mohsen, H., El-Dahshan, E.-S. A., El-Horbaty, E.-S. M., Salem, A.-B. M., "Classification using deep learning neural networks for brain tumors", *Future Computing and Informatics Journal,* 3(1), 68–71, 2018.

[8] Bulut, M. G., Unal, S., Hammad, M., Pławiak, P., "Deep CNN-based detection of cardiac rhythm disorders using PPG signals from wearable devices", *Plos One*, 20(2), 2025.

[9] Fukushima, K., "Neocognitron: A self-organizing neural network model for a mechanism of pattern recognition unaffected by shift in position", *Biological Cybernetics*, 36, 193–202, 1980.

[10] LeCun, Y., Bottou, L., Bengio, Y., Haffner, P., "Backpropagation applied to handwritten zip code recognition", *Neural Computation*, 1(4), 541–551, 1989.

[11] Zeiler, M. D., Fergus, R., "Visualizing and understanding convolutional networks", Proceedings of European Conference on Computer Vision, Zurich, Switzerland, pp. 818–833, 2014.

[12] Simonyan, K., Zisserman, A., "Very deep convolutional networks for large-scale image recognition", Proceedings of 3rd International Conference on Learning Representations (ICLR), San Diego, USA, 2015.

[13] Rubin, J., Abreu, R., Ganguli, A., Nelaturi, S., Matei, I., Sricharan, K., "Recognizing abnormal heart sounds using deep learning", Proceedings of Computing in Cardiology Conference, Rennes, France, 2017.

[14] Ozturk, T., Talo, M., Azra, E., Baran, U., Yildirim, O., "Automated detection of COVID-19 cases using deep neural networks with X-ray images", *Computers in Biology and Medicine*, 121, 2020.

[15] Tsirtsakis, P., Zacharis, G., Maraslidis, G. S., Fragulis, G. F., "Deep learning for object recognition: A comprehensive review of models and algorithms", *International Journal of Cognitive Computing in Engineering*, 6, 298–312, 2025.

[16] Panwar, M., et al., "CNN based approach for activity recognition using a wrist-worn accelerometer", Proceedings of the Annual International Conference of the IEEE Engineering in Medicine and Biology Society, Jeju Island, South Korea, pp. 2438–2441, 2017.

[17] Silver, D., et al., "Mastering chess and shogi by self-play with a general reinforcement learning algorithm", *arXiv preprint*, arXiv:1712.01815, 2017.

[18] Nelson, D. M. Q., Pereira, A. C. M., De Oliveira, R. A., "Stock market's price movement prediction with LSTM neural networks", Proceedings of International Joint Conference on Neural Networks (IJCNN), Anchorage, USA, vol. 2017-May, pp. 1419–1426, 2017.

[19] Wang, Y., Li, B., Todo, Y., "Enhancing robustness of object detection: Hubel–Wiesel model connected with deep learning", *Knowledge-Based Systems*, 311, 2025.

[20] Deutsch, S., Biological Cybernetics: A Simplified Version of Kunihiko Fukushima's Neocognitron. Tokyo: Springer, 1981.

[21] McCulloch, W. S., Pitts, W., "A logical calculus of the ideas immanent in nervous activity", *Bulletin of Mathematical Biophysics*, 5, 115–133, 1943.

[22] Hubel, D. H., Wiesel, T. N., "Shape and arrangement of columns in cat's striate cortex", *Journal of Physiology*, 165(3), 559–568, 1963.

[23] Fukushima, K., "Neocognitron: A self-organizing neural network model for a mechanism of pattern recognition unaffected by shift in position", *Biological Cybernetics*, 36(4), 193–202, 1980.

[24] LeCun, Y., Bottou, L., Bengio, Y., Haffner, P., "Gradient-based learning applied to document recognition", *Proceedings of the IEEE*, 86(11), 2278–2323, 1998.

[25] Szegedy, C., et al., "Going deeper with convolutions", IEEE Conference on Computer Vision and Pattern Recognition, 1–9, 2015.

[26] Mahyudin, R., et al., "Design of Automated Smart Attendance System Using Deep Learning Based Face Recognition", Proceedings of 9th International Conference on Science, Technology, Engineering and Mathematics (ICONSTEM), Chennai, India, 2024.

[27] Mnih, V., et al., "Human-level control through deep reinforcement learning", *Nature*, 518(7540), 529–533, 2015.

[28] Banerjee, A., Swain, S., Rout, M., Bandyopadhyay, M., "Composite spectral spatial pixel CNN for land-use hyperspectral image classification with hybrid activation function", *Multimedia Tools and Applications*, 1-24, 2024.

[29] Wu, T., et al., "A brief overview of ChatGPT: The history, status quo and potential future development", *IEEE/CAA Journal of Automatica Sinica*, 10(5), 1122–1136, 2023.

[30] Sharifuzzaman Sagar, A. S. M., Chen, Y., Xie, Y. K., Kim, H. S., "MSA R-CNN: A comprehensive approach to remote sensing object detection and scene understanding", *Expert Systems with Applications*, 241, 2024.

[31] Berner, C., et al., "Dota 2 with Large Scale Deep Reinforcement Learning", *arXiv preprint*, arXiv:1912.06680, 2019.

[32] Zhang, Y., Qian, H., Zhang, J., Shi, Z., "Action Recognition Networks Based on Spatio-Temporal Motion Modules", Proceedings of 2024 International Conference on Advances in Electrical Engineering and Computer Applications (AEECA), Shenyang, China, pp. 436–440, 2024.

[33] Wang, Y., et al., "RingMo-Lite: A Remote Sensing Lightweight Network With CNN-Transformer Hybrid Framework", *IEEE Transactions on Geoscience and Remote Sensing*, 62, 1–20, 2024.

[34] Hochreiter, S., Schmidhuber, J., "Long Short-Term Memory", *Neural Computation*, 9(8), 1735–1780, 1997.

[35] Rumelhart, D. E., Hinton, G. E., Williams, R. J., "Learning representations by back-propagating errors", *Nature*, 323(6088), 533–536, 1986.

[36] Kirov, C., Cotterell, R., "Recurrent Neural Networks in Linguistic Theory: Revisiting Pinker and Prince (1988) and the Past Tense Debate", *Transactions of the Association for Computational Linguistics*, 6, 2018.

[37] Hochreiter, S., Schmidhuber, J., "Long Short-Term Memory", *Neural Computation*, 9(8), 1735–1780, 1997.

[38] Sun, L., Jia, K., Chen, K., Yeung, D. Y., Shi, B. E., Savarese, S., "Lattice Long Short-Term Memory for Human Action Recognition", Proceedings of the IEEE International Conference on Computer Vision (ICCV), Venice, Italy, pp. 2147–2156, 2017.

[39] Zhou, J., Lu, Y., Dai, H. N., Wang, H., Xiao, H., "Sentiment analysis of Chinese microblog based on stacked bidirectional LSTM", *IEEE Access*, 7, 38856–38866, 2019.

[40] Chen, Y., Yuan, J., You, Q., Luo, J., "Twitter Sentiment Analysis via Bi-sense Emoji Embedding", Proceedings of the 26th ACM International Conference on Multimedia, Seoul, South Korea, pp. 117–125, 2018.

[41] Kim, T., Kim, H. Y., "Forecasting stock prices with a feature fusion LSTM-CNN model using different representations of the same data," *Plos One*, 14(2), 2019.

[42] Tian, Y., Zhang, K., Li, J., Lin, X., Yang, B., "LSTM-based traffic flow prediction with missing data," *Neurocomputing*, 318, 297–305, 2018.

[43] Karevan, Z., Suykens, J. A. K., "Spatio-temporal stacked LSTM for temperature prediction in weather forecasting," *arXiv preprint*, arXiv:1811.06341, 2018.

[44] Yang, F., Zhang, S., Li, W., Miao, Q., "State-of-charge estimation of lithium-ion batteries using LSTM and UKF," *Energy*, 201, 117664, 2020.

[45] Dehouche, N., Dehouche, K., "What's in a text-to-image prompt? The potential of stable diffusion in visual arts education," *Heliyon*, 9(6), e16757, 2023.

[46] Chamola, V., et al., "Beyond reality: The pivotal role of generative AI in the Metaverse," *arXiv preprint*, arXiv:2308.06272, 2023.

[47] Akhtar, Z., "Deepfakes generation and detection: A short survey," *Journal of Imaging*, 9(1), 2023.

[48] Privacy Affairs, "What are Deepfakes, their threats, and how to avoid them?," [Online]. Available: https://www.privacyaffairs.com/deepfakes/

[49] Goodfellow, I. J., et al., "Generative adversarial nets," *Advances in Neural Information Processing Systems*, 27, 2014.

[50] Huang, X., Liu, M., Belongie, S., Kautz, J., "Multimodal unsupervised image-to-image translation," Proceedings of the European Conference on Computer Vision (ECCV), Munich, Germany, pp. 172–189, 2018.

[51] Karras, T., Aila, T., Laine, S., Lehtinen, J., "Progressive growing of GANs for improved quality, stability, and variation," Proceedings of 6th International Conference on Learning Representations (ICLR), Vancouver, Canada, 2018.

[52] Li, J., Monroe, W., Shi, T., Jean, S., Ritter, A., Jurafsky, D., "Adversarial learning for neural dialogue generation," Proceedings of the 2017 Conference on Empirical Methods in Natural Language Processing (EMNLP), Copenhagen, Denmark, pp. 2157–2169, 2017.

[53] Hu, W., Tan, Y., "Generating adversarial malware examples for black-box attacks based on GAN," *arXiv preprint*, arXiv:1702.05983, 2017.

[54] Chidambaram, M., Qi, Y., "Style transfer generative adversarial networks: Learning to play chess differently," *arXiv preprint*, arXiv:1702.06762, 2017.

[55] Thorndike, E. L., "Animal intelligence: An experimental study of the associative processes in animals," *The Psychological Review Monograph Supplements*, 2(4), i–109, 1898.

[56] Thorndike, E. L., "Animal intelligence," *Psychological Review Monographs*, 2(4), 1898.

[57] Kaelbling, L. P., Littman, M. L., Moore, A. W., "Reinforcement learning: A survey," *Journal of Artificial Intelligence Research*, 4, 237–285, 1996.

[58] Silver, D., et al., "Mastering the game of Go with deep neural networks and tree search," *Nature*, 529(7587), 484–489, 2016.

[59] Lancaster, T., "Artificial intelligence, text generation tools and ChatGPT – does digital watermarking offer a solution?," *International Journal for Educational Integrity*, 19(1), 1–14, 2023.

[60] Teubner, T., Flath, C. M., Weinhardt, C., van der Aalst, W., Hinz, O., "Welcome to the Era of ChatGPT et al.: The Prospects of Large Language Models," *Business and Information Systems Engineering*, 65(2), 95–101, 2023.

[61] 365 Data Science, "The Evolution of ChatGPT: History and Future," [Online]. Available: https://365datascience.com/trending/the-evolution-of-chatgpt-history-and-future/.

[62] Singh, H., Singh, A., "ChatGPT: Systematic Review, Applications, and Agenda for Multidisciplinary Research," *Journal of Chinese Economic and Business Studies*, 21(2), 193–212, 2023.

[63] Heinrich, J., Silver, D., "Deep Reinforcement Learning from Self-Play in Imperfect-Information Games," arXiv preprint, arXiv:1603.01121, 2016.

[64] Gu, S., Holly, E., Lillicrap, T., Levine, S., "Deep reinforcement learning for robotic manipulation with asynchronous off-policy updates," Proceedings of IEEE International Conference on Robotics and Automation (ICRA), Singapore, pp. 3389–3396, 2017.

[65] El Sallab, A., Abdou, M., Perot, E., Yogamani, S., "Deep reinforcement learning framework for autonomous driving," IS&T International Symposium on Electronic Imaging, Burlingame, USA, pp. 70–76, 2017.

[66] Zhou, Z., Li, X., Zare, R. N., "Optimizing chemical reactions with deep reinforcement learning," *ACS Central Science*, 3(12), 1337–1344, 2017.

[67] Zheng, G., et al., "DRN: A deep reinforcement learning framework for news recommendation," *The Web Conference (WWW)*, 2, 167–176, 2018.

[68] Bromley, J., Bentz, J., Bottou, L., Guyon, I., LeCun, Y., Moore, C., "Signature verification using a 'siamese' time delay neural network," *International Journal of Pattern Recognition and Artificial Intelligence*, 7(4), 669–688, 1993.

[69] Chicco, D., "Siamese neural networks: An overview," *Artificial Neural Networks*, pp. 73–94, 2021.

[70] Koch, G., "Siamese neural networks for one-shot image recognition," [Online]. Available: http://www.cs.toronto.edu/~gkoch/files/msc-thesis.pdf, 2015.

[71] Ahrabian, K., BabaAli, B., "Usage of autoencoders and siamese networks for online handwritten signature verification," *Neural Computing and Applications*, 31(12), 9321–9334, 2019.

[72] Song, L., Gong, D., Li, Z., Liu, C., Liu, W., "Occlusion robust face recognition based on mask learning with pairwise differential siamese network," Proceedings of IEEE/CVF International Conference on Computer Vision (ICCV), Seoul, South Korea, pp. 773–782, 2019.

[73] Jindal, S., Gupta, G., Yadav, M., Sharma, M., Vig, L., "Siamese networks for chromosome classification," Proceedings of IEEE International Conference on Computer Vision Workshops (ICCVW), Venice, Italy, pp. 72–81, 2017.

[74] Schlesinger, O., Vigderhouse, N., Eytan, D., Moshe, Y., "Blood pressure estimation from PPG signals using convolutional neural networks and siamese network," Proceedings of ICASSP 2020 - IEEE International Conference on Acoustics, Speech and Signal Processing, Barcelona, Spain, pp. 1135–1139, 2020.

[75] Hinton, G. E., Krizhevsky, A., Wang, S. D., "Transforming auto-encoders," Proceedings of 21st International Conference on Artificial Neural Networks (ICANN), Espoo, Finland, pp. 44–51, 2011.

[76] Choudhary, S., Saurav, S., Saini, R., Singh, S., "Capsule networks for computer vision applications: A comprehensive review," *Applied Intelligence*, 53, 21799–21826, 2023.

[77] Li, J., et al., "A survey on capsule networks: Evolution, application, and future development," Proceedings of 2021 International Conference on High Performance Big Data and Intelligent Systems (HPBD and IS), Shenzhen, China, pp. 177–185, 2021.

[78] Bronstein, M. M., Bruna, J., Cohen, T., Veličković, P., "Geometric deep learning: Grids, groups, graphs, geodesics, and gauges," *arXiv preprint*, arXiv:2104.13478, 2021.

[79] Cao, W., Yan, Z., He, Z., He, Z., "A comprehensive survey on geometric deep learning," *IEEE Access*, 8, 35929–35949, 2020.

[80] Cao, W., Zheng, C., Yan, Z., He, Z., Xie, W., "Geometric machine learning: Research and applications," *Multimedia Tools and Applications*, 81(21), 30545–30597, 2022.

[81] Bronstein, M. M., Bruna, J., LeCun, Y., Szlam, A., Vandergheynst, P., "Geometric Deep Learning: Going beyond Euclidean data," *IEEE Signal Processing Magazine*, 34(4), 18–42, 2017.

[82] Qiao, Z., Christensen, A. S., Welborn, M., Manby, F. R., Anandkumar, A., Miller III, T. F., "Informing geometric deep learning with electronic interactions to accelerate quantum chemistry," *Proceedings of the National Academy of Sciences*, 119(31), 2022.

[83] Atz, K., Grisoni, F., Schneider, G., "Geometric deep learning on molecular representations," *Nature Machine Intelligence*, 3(12), 1023–1032, 2021.

[84] Villalba-Diez, J., Molina, M., Schmidt, D., "Geometric deep lean learning: Evaluation using a Twitter social network," *Applied Sciences*, 11(15), 2021.

[85] Han, K., et al., "A survey on vision transformer," *IEEE Transactions on Pattern Analysis and Machine Intelligence*, 45(1), 87–110, 2023.

[86] Vaswani, A., Shazeer, N., Parmar, N., Uszkoreit, J., Jones, L., Gomez, A. N., "Attention is all you need," *Advances in Neural Information Processing Systems*, 30, 2017.

[87] Chitty-Venkata, K. T., Emani, M., Vishwanath, V., Somani, A. K., "Neural architecture search for transformers: A survey," *IEEE Access*, 10, 108374–108412, 2022.

[88] Parmar, N., et al., "Image transformer," Proceedings of International Conference on Machine Learning (ICML), Stockholm, Sweden, pp. 4055–4064, 2018.

[89] Touvron, H., Cord, M., Sablayrolles, A., Synnaeve, G., Jégou, H., "Going deeper with image transformers," Proceedings of IEEE/CVF International Conference on Computer Vision (ICCV), Montreal, Canada, pp. 32–42, 2021.

[90] Dosovitskiy, A., Beyer, L., Kolesnikov, A., Weissenborn, D., Zhai, X., "An image is worth 16x16 words: Transformers for image recognition at scale," *arXiv preprint*, arXiv:2010.11929, 2020.

[91] Ras, G., Xie, N., van Gerven, M., Doran, D., "Explainable deep learning: A field guide for the uninitiated," *Journal of Artificial Intelligence Research*, 73, 329–396, 2022.

[92] Rasouli, P., Yu, I. C., "Explainable debugger for black-box machine learning models," Proceedings of 2021 International Joint Conference on Neural Networks (IJCNN), Shenzhen, China, pp. 1–10, 2021.

[93] Barredo Arrieta, A., et al., "Explainable artificial intelligence (XAI): Concepts, taxonomies, opportunities and challenges toward responsible AI," *Information Fusion*, 58, 82–115, 2020.

[94] Lisboa, P. J. G., Saralajew, S., Vellido, A., Villmann, T., "The coming of age of interpretable and explainable machine learning models," *Neurocomputing*, 535, 25–39, 2023.

[95] Cha, Y., Lee, Y., "Advanced sentence-embedding method considering token importance based on explainable artificial intelligence and text summarization model," *Neurocomputing*, 564, 126987, 2024.

[96] Oviedo, F., Ferres, J. L., Buonassisi, T., Butler, K. T., "Interpretable and explainable machine learning for materials science and chemistry," *Accounts of Materials Research*, 3(6), 597–607, 2022.

[97] Dasari, C. M., Bhukya, R., "Explainable deep neural networks for novel viral genome prediction," *Applied Intelligence*, 52(3), 3002–3017, 2022.

[98] Zogan, H., Razzak, I., Wang, X., Jameel, S., Xu, G., "Explainable depression detection with multi-aspect features using a hybrid deep learning model on social media," *World Wide Web*, 25(1), 281–304, 2022.

[99] Buolamwini, J., Gebru, T., "Gender shades: Intersectional accuracy disparities in commercial gender classification," Proceedings of the Conference on Fairness, Accountability, and Transparency (FAT), 2018.

[100] Mehrabi, N., Morstatter, F., Saxena, N., Lerman, K., Galstyan, A., "A survey on bias and fairness in machine learning," *ACM Computing Surveys*, 54(6), 2021.

[101] O'Neil, C., *Weapons of Math Destruction: How Big Data Increases Inequality and Threatens Democracy*. New York, NY: Crown Publishing Group, 2016.

[102] Papernot, N., McDaniel, P., Goodfellow, I., Jha, S., Celik, Z. B., Swami, A., "Practical black-box attacks against machine learning," Proceedings of the ACM Asia Conference on Computer and Communications Security (ASIACCS), Abu Dhabi, United Arab Emirates, pp. 506–519, 2017.

[103] Brynjolfsson, E., McAfee, A., *The Second Machine Age: Work, Progress, and Prosperity in a Time of Brilliant Technologies*. New York, NY: W. W. Norton & Company, 2014.

[104] Imam, N. M., Ibrahim, A., Tiwari, M., "Explainable Artificial Intelligence (XAI) Techniques to Enhance Transparency in Deep Learning Models," *IOSR Journal of Computer Engineering*, 26(6), 29–36, 2024.

[105] Bikkasani, D. C., "Navigating artificial general intelligence (AGI): Societal implications, ethical considerations, and governance strategies," *AI and Ethics*, 2024.

Middle East Journal of Science

https://dergipark.org.tr/mejs **MEJS**

e-ISSN:2618-6136

Review

PESTICIDES FROM PUBLIC HEALTH PERSPECTIVE: THREATS, RISKS AND PREVENTIVE STRATEGIES

Ali Asım IŞIK [1] ***Zehra KILINÇ*** [2]

[1]-Dicle Üniversity Institute of Health Sciences Department of Public Health, Diyarbakir, Türkiye
[2]-Dicle University Faculty of Medicine Department of Public Health, Diyarbakir, Türkiye.
Corresponding Author; aliasim21@gmail.com

Abstract: *Pesticides are chemical substances widely used in modern agriculture to enhance crop productivity and combat pests. However, the uncontrolled and widespread use of pesticides poses significant threats to both the environment and human health. This study examines the public health impacts of pesticides, focusing on exposure pathways, health effects, and prevention strategies. The study highlights that exposure to pesticides primarily occurs through inhalation, dermal contact, and the consumption of contaminated food and drinking water, emphasizing that vulnerable groups such as children, pregnant women, and agricultural workers are particularly at risk of experiencing severe health issues. In addition to acute poisonings, long-term low-dose exposure has been scientifically linked to chronic diseases, including cancer, neurological disorders, and endocrine disruptions. The study also elaborates on primary, secondary, and tertiary prevention strategies within the framework of public health and offers recommendations regarding alternative agricultural practices and regulatory measures. In this context, effective monitoring, education, the promotion of alternative methods, and the enhancement of public awareness are necessary to reduce the harmful effects of pesticides.*

Keywords: *Pesticide, public health, food safety, organic farm, acute poisoning, chronic exposure*

Received:May 21, 2025 *Accepted: June 16, 2025*

1. Introduction

Pesticides are chemical or biological substances used to kill, control, or repel harmful organisms. In recent years, the use of pesticides has significantly increased in order to meet the growing global demand for food [1, 2]. However, the indiscriminate use of these chemicals poses serious threats not only to pests but also to human health, the environment, and ecosystems [3, 4]. These substances may be applied directly or indirectly to plants, seeds, soil, or water. Based on the type of pests they target, pesticides can be classified as follows:

- **Insecticides**: Effective against insects
- **Herbicides**: Destroy weeds
- **Fungicides**: Target fungal pathogens
- **Rodenticides**: Eliminate rodents such as rats and mice
- **Others**: Including acaricides, bactericides, nematicides, etc.

Some pesticides are lipophilic (fat-soluble), which enables them to accumulate in body fat and potentially lead to long-term toxic effects [5, 6, 7]. Their widespread use in both agricultural and domestic environments represents a significant threat to public and environmental health. Due to their persistent nature, these chemicals can remain in the environment for long periods and gradually enter

the food chain [8]. The health impacts of pesticides today are not limited to acute poisoning; numerous scientific studies have linked them to a broad range of chronic diseases, including cancer, neurological disorders, congenital anomalies, endocrine disruption, and reproductive health issues [2, 9, 10].

Although pesticide use continues to rise, inadequate monitoring of residues and limited adoption of alternative pest control methods have intensified the problem. While many countries—particularly within the European Union—have implemented stricter pesticide regulations, public health risks remain high in developing and underdeveloped nations due to insufficient enforcement and a lack of public awareness [11, 12]. Pesticide residues have been detected in a variety of foods and beverages, including fruit juices, wine, water, snacks, and poultry feed. Research has shown that simple washing and peeling are not enough to remove these residues. Furthermore, the detection of pesticide residues in breast milk indicates the possibility of fetal exposure. Collectively, these findings indicate that pesticides represent one of the most pressing public health challenges of our time [13, 14].

2. Routes of Exposure

Pesticide exposure varies depending on an individual's lifestyle, occupation, living environment, and consumption habits. The level and duration of exposure are among the primary factors influencing health. Agricultural workers, individuals living in rural areas, and children are particularly at higher risk of exposure to these substances [9, 15].

In general, pesticide exposure occurs through four main routes: inhalation, dermal contact, ingestion through food, and contaminated drinking water.

2.1. Inhalation Exposure

Most pesticides are applied in agricultural settings via spraying techniques. During this process, aerosols and vapors released into the air can remain suspended and disperse throughout the environment. Not only applicators but also nearby individuals can be exposed to these airborne pesticide particles through inhalation [16].

It has been observed that pesticides can be carried several hundred meters under windy conditions [3]. Numerous studies have reported a high prevalence of acute respiratory illnesses and asthma-like symptoms among agricultural workers [17].

2.2. Dermal Exposure

Dermal contact represents one of the most common exposure routes, particularly for agricultural workers and pesticide applicators. During application, pesticides can be absorbed through exposed areas such as the hands, arms, and face. Many pesticides, due to their lipophilic nature, can easily penetrate the skin barrier [17, 18].

In the absence of appropriate protective equipment, pesticides have been documented to cause skin irritation, redness, and systemic absorption, and in some cases, serious poisoning [7, 19, 20].

2.3. Dietary Exposure

The primary route of pesticide exposure for consumers is through the ingestion of fruits and vegetables containing pesticide residues. If the pre-harvest interval is not adequately observed after pesticide application, residue levels in the produce may increase. High-risk products include strawberries, peppers, lettuce, and grapes [21, 22].

2.4. Waterborne Exposure

Some pesticides can contaminate surface and groundwater sources, thereby polluting drinking water supplies. This represents a significant health risk, especially for populations living in regions

with intensive agricultural activity. The magnitude of this risk depends on the solubility, half-life, adsorption capacity, and biodegradability of the pesticide compounds [23].

2.5. Determinants of Exposure

The health impact of pesticide exposure must be evaluated considering the type of pesticide, dosage, duration of exposure, and individual factors such as age and health status. For instance, children are more vulnerable due to higher food intake per body weight and immature detoxification systems [15, 16].

Moreover, certain pesticides can cross the placental barrier during pregnancy and directly affect fetal development [24].

3. Acute and Chronic Health Effects

Health problems caused by pesticide poisoning can be examined in two groups: acute (short-term exposure to high doses) and chronic (long-term exposure to low doses). Acute effects are more commonly seen in groups that are in close contact with pesticides, such as agricultural workers and spraying personnel. Chronic effects, on the other hand, are more widespread in the general population and often progress insidiously without noticeable symptoms. While acute effects are often dramatic and prompt immediate clinical attention, chronic effects frequently remain unnoticed until irreversible damage has occurred [2, 9, 11, 25].

3.1. Acute Health Effects

Acute pesticide poisonings generally occur as a result of short-term exposure to high doses during pesticide applications. They are most frequently encountered among agricultural workers. Especially in developing and underdeveloped countries, such poisonings are common due to the lack of protective measures such as masks and protective equipment [3, 9].

Acute toxic effects may appear within a few minutes to several hours after pesticide exposure. Poisoning affects not only peripheral muscarinic and nicotinic receptors but also the central nervous system. Symptoms of acute pesticide poisoning include nausea, vomiting, diarrhea, abdominal cramps, urinary incontinence, miosis, excessive salivation, lacrimation, bronchorrhea, bradycardia, hypotension, twitching, muscle paralysis, dizziness, confusion, seizures, coma, and respiratory failure. These effects can appear immediately upon exposure. Moreover, if not treated promptly and appropriately, life-threatening complications may occur, leading to death [8].

The severity of these symptoms depends on the dose and type of pesticide. The most common types of poisoning are associated with organophosphate and carbamate pesticides. Globally, approximately 3 million pesticide poisoning cases occur each year, with around 220,000 resulting in death. The vast majority of these cases are reported in low- and middle-income countries in Africa, Latin America, and Asia [3, 9].

Most deaths result not from occupational or accidental exposure via skin contact or inhalation, but from intentional ingestion in suicide attempts. Overall, the pesticide poisoning mortality rate has been decreasing as newer and safer pesticides are incorporated into global agricultural practices and more toxic pesticides are phased out. This effect has been clearly observed in Sri Lanka and China, where the number of pesticide-related suicides has dropped by over 70% in the last two decades [26].

According to data from the Turkish Ministry of Health, more than 5,400 acute pesticide poisoning cases were reported between 2018 and 2022. The majority of cases were observed in individuals working in the agricultural sector [27].

3.2. Chronic Health Effects

Chronic pesticide exposure occurs over a long period and usually at low doses; thus, symptoms develop slowly and are often noticed too late. However, the effects may be much more persistent and severe compared to acute poisonings [2, 11].

3.2.1 Cancer Risk Associated with Pesticide Exposure

Numerous epidemiological studies have shown significant associations between pesticide exposure and certain types of cancer such as prostate, leukemia, lymphoma, and breast cancer [25, 28]. Some pesticides can directly damage DNA, leading to mutations and tumor development [29].

In particular, studies on herbicides and insecticides have revealed an increased risk of colon and rectal cancer [30].

3.2.2 Neurological and Psychiatric Effects

The effects of pesticides on the central nervous system have been linked to depression, anxiety, cognitive decline, and Parkinson's disease [31, 32].

3.2.3 Endocrine System Disorders

Some pesticides are classified as endocrine-disrupting chemicals (EDCs). These chemicals can interfere with the functions of hormones such as thyroid, estrogen, and insulin. This can lead to health problems such as developmental delays, obesity, infertility, and thyroid diseases, particularly in children [33-35].

3.2.4 Reproductive and Developmental Effects

Pesticide exposure may increase the risk of reproductive problems such as decreased fertility in women, abnormal births, irregular menstruation, premature birth, miscarriage, stillbirth, congenital abnormalities, and low birth weight [36]. There are also studies showing that some pesticides reduce sperm quality and may cause infertility in men. Furthermore, pesticides that can cross the placental barrier may directly affect fetal development and lead to undesirable outcomes [37].

3.2.5 Effects on the Immune System

Some types of pesticides may suppress the immune system and increase susceptibility to infections. They have also been shown to be associated with autoimmune diseases [18]. Scientific studies have demonstrated that pesticides such as atrazine (ATR), organophosphates (OP), carbamates, and pyrethrins can impair the survival and growth of leukocytes by inducing apoptosis or cell cycle arrest and interfering with the specific immunological functions of immune cell types [38].

4. Global and Local Pesticide Usage Rates

According to FAO (2022) data, global pesticide use in 2021 was approximately 4.1 million tons, representing an increase of more than 60% compared to 1990. Several factors have contributed to this significant rise. One of the primary reasons is the widespread adoption of monoculture farming systems, which are more vulnerable to pest infestations. Additionally, the development of resistance to pesticides among pests has led to the need for increased application. Climate change has also played a role by creating conditions that favor the growth and spread of pest populations. Furthermore, high yield expectations and economic pressures have driven farmers to rely more heavily on pesticides to protect their crops and maximize production [12, 39].

The countries that use the most pesticides are China (approximately 1,800,000 tons), the United States (around 400,000 tons), and Brazil (about 380,000 tons) [12].

Active ingredients such as glyphosate, chlorpyrifos, and mancozeb are among the most commonly used pesticides globally [29].

Pesticide use in Turkey has shown a significant increase over the past 10 years. According to data from TURKSTAT and the Ministry of Agriculture and Forestry, approximately 62,300 tons of pesticides were used in 2023. This amount is nearly double the usage in 2010 [40].

In inspections conducted by the Ministry of Agriculture and Forestry, the issue of pesticide residues in food in Turkey is notable. In 2022, it was found that 7.6% of fruit and vegetable samples analyzed exceeded the maximum residue limit (MRL) [40]. The average pesticide use among European Union member countries is 3.5% [21].

In Turkey, Antalya is the province with the highest pesticide use, while Ardahan uses the least. The Mediterranean Region accounts for the highest pesticide use due to its diverse crop cultivation, whereas the Black Sea Region uses the least. In 2020, the most used pesticide groups in Turkey were fungicides (38.4%), herbicides (27.4%), and insecticides (23.0%), respectively. An examination of the top three provinces with the highest pesticide use reveals that fungicides were the most common in Antalya (38.3%) and Manisa (81.0%), while insecticides were predominant in Adana (65.2%) [41]

As of 2021, the average pesticide use per hectare in Türkiye was 2.26 kg. This amount is lower than the European Union average (3.20 kg/ha) but higher than the global average (1.07 kg/ha). While herbicides account for the largest share of pesticide use per unit area worldwide (21.92%), fungicides and bactericides have the highest share in the EU (43.18%) and in Türkiye (36.06%). This indicates that pesticide use in Türkiye is particularly concentrated on combating fungal and bacterial diseases [42].

To assess compliance with maximum residue limits (MRLs) of pesticides, the most commonly used methods include the QuEChERS extraction technique combined with LC-MS/MS or GC-MS/MS analysis. These methods allow for the simultaneous and highly sensitive detection of multiple pesticide residues. The results of such analyses play a critical role in identifying potential health risks when MRLs are exceeded and in ensuring consumer safety [43].

5. Strategies for Minimizing Pesticide Exposure

To mitigate the harmful effects of pesticides on human health and the environment, it is crucial to develop multifaceted protection strategies at individual, societal, legal, and political levels. In addition, it is imperative to promote sustainable and environmentally conscious agricultural practices as viable alternatives to traditional chemical control methods [2, 9, 44].

5.1. Primary Prevention: Preventing Exposure

At this level, the primary objective is to prevent pesticide exposure before it occurs, thereby safeguarding society from potential health risks:

5.1.1 Personal Protection Methods

The use of personal protective equipment (PPE) by pesticide applicators significantly reduces direct exposure. Equipment such as gloves, masks, and protective eyewear acts as a physical barrier against pesticide residues. Furthermore, compliance with hygiene and safety protocols by applicators plays a pivotal role in preventing exposure [3, 45, 46].

5.1.2 Food Cleaning and Preparation Techniques

Consumers can mitigate pesticide residues by thoroughly washing fruits and vegetables with abundant water, peeling products with peelable skins, and opting for organic produce. However, it should be noted that washing and peeling may not completely eliminate pesticide residues [47].

5.1.3 Education and Awareness Programs

The dissemination of educational programs has been shown to reduce pesticide application errors and poisoning incidents. Tailoring educational programs to specific target groups (such as farmers, children, and consumers) will be more effective. Social media campaigns can also play a significant role in raising awareness about pesticide use [48, 49].

5.1.4 Legal Measures and Inspections

The frequency and scope of inspections should be increased; residue analyses must be conducted routinely for both domestic and export products [21]. Additionally, legal authorities should enforce the prohibition or restriction of hazardous pesticides [9].

5.1.5 Alternative Practices

Organic farming represents a production model where the use of synthetic chemical pesticides is strictly prohibited. Pest management is accomplished through natural methods, with an emphasis on biological and physical interventions. The risk of pesticide residues in organic products is negligible. However, due to production costs and the challenges associated with inspections, continuous support for organic farming is essential [47, 50].

5.1.6 Biological Control

This method involves the use of natural predators of harmful organisms (such as predatory insects, parasitoids, etc.). For example, *Bacillus thuringiensis* is highly effective against lepidopteran larvae [51].

5.1.7 Digital and Technological Solutions

Advancements in agricultural technologies present significant opportunities for reducing pesticide use. These include disease and pest detection using sensors and IoT devices, as well as precision spraying through drone and GPS technology [52, 53].

5.2. Secondary Prevention: Early Detection and Intervention

The goal at this stage is to identify individuals exhibiting early symptoms in order to limit the effects and prevent the progression of the disease:

5.2.1 Toxicological Screening and Biological Monitoring

Regular testing for individuals working with pesticides, including measurements of blood cholinesterase levels and liver and kidney functions [2, 54, 55].

5.2.2 Poisoning Surveillance Systems

Public health institutions should actively utilize pesticide poisoning reporting and recording systems, and early identification of high-risk areas should be implemented [27, 56]. Turkey lacks adequate monitoring and registration systems for pesticides. Comprehensive studies and effective systems are needed in these areas.

5.2.3 Community-Based Screening

Neurological, endocrine, and psychological health screenings should be conducted for populations residing in areas with intensive pesticide use [57, 58].

5.3. Tertiary Prevention: Damage Reduction and Rehabilitation

The objective at this level is to prevent permanent damage and enhance the quality of life in individuals who have suffered health damage due to pesticide exposure:

5.3.1 Treatment in Centers with Toxicology and Neurology Specialization

Patients who have been poisoned should undergo appropriate rehabilitation and multidisciplinary follow-up.

5.3.2 Psychosocial Support

Psychological support should be provided for conditions such as depression, anxiety, or cognitive disorders that may develop following pesticide exposure. Additionally, given that a significant portion of acute pesticide poisonings is suspected to be related to suicide attempts, the importance of psychosocial support becomes even more evident.

5.3.3 Discontinuation of Exposure for Poisoned Workers

Workers who have developed chronic health issues due to pesticide exposure should be reassigned to alternative roles and provided with social security support [26, 59, 60].

6. Conclusion

To ensure effective control over pesticide use, licensing and regulatory inspection processes should be enhanced through greater transparency and stricter enforcement. Additionally, comprehensive education and awareness programs must be implemented at both the producer and consumer levels to foster informed decision-making and promote safer agricultural practices. Strengthening adherence to international agreements is crucial for the complete elimination of banned pesticides. In addition, offering financial and technical assistance for sustainable agricultural practices, including organic farming, is crucial for decreasing reliance on hazardous chemical inputs.

Addressing the challenges posed by pesticide use requires solutions that are not limited to individual actions but are instead grounded in systematic, science-based, and sustainable approaches. Such strategies are essential to ensuring the long-term viability of agricultural production while simultaneously protecting public health.

Ethical statements

The author confirms that no ethics committee approval or special authorization was necessary for this document.

Conflict of Interest

The author confirms that no conflicts of interest exist.

Authors' contributions

Both authors contributed to the preparation of this review article and read the final version.

Generative AI statement

The authors declare that no Gen AI was used in the creation of this manuscript.

References

[1] Rad, S. M., Ray, A. K., & Barghi, S., "Water pollution and agriculture pesticide", *Clean Technologies*, 4(4), 1088-1102, 2022.

[2] Mostafalou, S., & Abdollahi, M.S., "Pesticides: an update of human exposure and toxicity", *Arch. Toxicol.*, 91(2), 549-599, 2017. Doi: 10.1007/s00204-016-1849-x

[3] World Health Organization, "Pesticide residues in food and drinking water: Human health risks. Geneva: WHO Press", 2021. [Online]. Available: https://www.who.int/publications/i/item/9789240035269

[4] Issa, S. T., Takshe, A. A., Alwan, N. H., & ElBarazi, I., "Pesticides exposure and public health", *Front. Public Health*, 11, 1211115, 2023.

[5] Mostafalou, S., & Abdollahi, M., "Pesticides and human chronic diseases: Evidences, mechanisms, and perspectives", *Toxicol. Appl. Pharmacol.*, 268(2), 157–177, 2013. Doi: 10.1016/j.taap.2013.01.025

[6] Sharma, A., Kumar, V., Shahzad, B., Tanveer, M., Sidhu, G. P. S., Handa, N., ... & Thukral, A. K., "Worldwide pesticide usage and its impacts on ecosystem", *SN Appl. Sci.*, 1, 1-16, 2019.

[7] United States Environmental Protection Agency (EPA), "Pesticide registration manual: Chapter 1–Overview of requirements for pesticide registration", 2020. [Online]. Available: https://www.epa.gov/pesticide-registration/pesticide-registration-manual-chapter-1-overview-requirements-pesticide

[8] Tudi, M., Li, H., Li, H., Wang, L., Lyu, J., Yang, L., ... & Connell, D., "Exposure routes and health risks associated with pesticide application", *Toxics*, 10(6), 335, 2022.

[9] Boedeker, W., Watts, M., Clausing, P., & Marquez, E., "The global distribution of acute unintentional pesticide poisoning: Estimations and trends", *BMC Public Health*, 20, 1875, 2020. Doi: 10.1186/s12889-020-09939-0

[10] Aytaç, N., Yüzügüllü, D. A., Demirhindi, H., & Gönültaş, T., "Pestisit Kullanımının Halk Sağlığı Etkileri", Arşiv Kaynak Tarama Dergisi, 26(4), 540-551, 2017

[11] European Food Safety Authority (EFSA), "The 2021 European Union report on pesticide residues in food", *EFSA J.*, 21(6), e08753, 2023. Doi: 10.2903/j.efsa.2023.7939

[12] Food and Agriculture Organization of the United Nations (FAO), "FAOSTAT statistical database: Pesticide use", 2022. [Online]. Available: https://www.fao.org/faostat/en/#data/RP

[13] Kaur, R., Choudhary, D., Bali, S., Bandral, S. S., Singh, V., Ahmad, M. A., ... & Chandrasekaran, B., "Pesticides: An alarming detrimental to health and environment", *Sci. Total Environ.*, 915, 170113, 2024.

[14] Aytaç, N., Hilal, A., Yapıcıoğlu, A. B., Dağlıoğlu, N., Gülmen, M. K., & Tanır, F., "Anne Sütünde Organoklorlu Pestisid (OKP) Düzeyi", Turkiye Klinikleri Journal of Medical Sciences, 30(1), 107-114, 2010

[15] Grandjean, P., & Landrigan, P. J., "Neurobehavioural effects of developmental toxicity", *Lancet Neurol.*, 13(3), 330–338, 2014. Doi: 10.1016/S1474-4422(13)70278-3

[16] Kim, K. H., Kabir, E., & Jahan, S. A., "Exposure to pesticides and the associated human health effects", *Sci. Total Environ.*, 575, 525–535, 2017. Doi: 10.1016/j.scitotenv.2016.09.009

[17] de-Assis, M. P., Barcella, R. C., Padilha, J. C., Pohl, H. H. ve Krug, S. B. F., "Health problems in agricultural workers occupationally exposed to pesticides", *Rev. Bras. Med. Trab.*, 18(3), 352, 2021.

[18] Corsini, E., Sokooti, M., Galli, C. L., Moretto, A., & Colosio, C., "Pesticide induced immunotoxicity in humans: A comprehensive review", *Toxicology*, 307, 123–135, 2013. Doi: 10.1016/j.tox.2012.10.009

[19] Del Prado-Lu, J. L., "Pesticide exposure, risk factors and health problems among cutflower farmers: a cross sectional study", *J. Occup. Med. Toxicol.*, 2, 1-8, 2007.

[20] Atabila, A., Sadler, R., Phung, D. T., Hogarh, J. N., Carswell, S., Turner, S., ... & Chu, C., "Biomonitoring of chlorpyrifos exposure and health risk assessment among applicators on rice farms in Ghana", *Environ. Sci. Pollut. Res.*, 25, 20854-20867, 2018.

[21] European Food Safety Authority (EFSA), "The 2020 European Union report on pesticide residues in food", *EFSA J.*, 20(6), e07215, 2022. Doi: 10.2903/j.efsa.2022.7215

[22] Bondareva, L., & Fedorova, N., "Pesticides: Behavior in agricultural soil and plants", *Molecules*, 26(17), 5370, 2021.

[23] Syafrudin, M., Kristanti, R. A., Yuniarto, A., Hadibarata, T., Rhee, J., Al-Onazi, W. A., ... & Al-Mohaimeed, A. M., "Pesticides in drinking water—a review", *Int. J. Environ. Res. Public Health*, 18(2), 468, 2021.

[24] Shelton, J. F., Geraghty, E. M., Tancredi, D. J., Delwiche, L. D., Schmidt, R. J., Ritz, B., & Hertz-Picciotto, I, "Neurodevelopmental disorders and prenatal residential proximity to agricultural pesticides: The CHARGE study", *Environ. Health Perspect.*, 122(10), 1103–1109, 2014.

[25] Alavanja, M. C. R., Ross, M. K., & Bonner, M. R., "Increased cancer burden among pesticide applicators and others due to pesticide exposure", *CA Cancer J. Clin.*, 63(2), 120–142, 2013.

[26] Eddleston, M., "Poisoning by pesticides," *Medicine*, 48(3), 214-217, 2020.

[27] Republic of Türkiye, Ministry of Health, Türkiye Poisoning Notification System: 2018–2022 Evaluation Report, Directorate General of Public Health, Department of Environmental Health, 2022.

[28] Zhang, L., Rana, I., Shaffer, R. M., Taioli, E., & Sheppard, L., "Exposure to pesticides and the risk of Parkinson's disease: An updated meta-analysis", *Int. J. Epidemiol.*, 48(3), 1025–1039, 2019.

[29] Mesnage, R., & Antoniou, M. N., "Facts and fallacies in the debate on glyphosate toxicity", *Front. Public Health*, 5, 316, 2017.

[30] Xie, P. P., Zong, Z. Q., Qiao, J. C., Li, Z. Y., & Hu, C. Y., "Exposure to pesticides and risk of colorectal cancer: A systematic review and meta-analysis", *Environ. Pollut.*, 345, 123530, 2024.

[31] Sánchez-Santed, F., Colomina, M. T., & Hernández, E. H., "Organophosphate pesticide exposure and neurodegeneration", *Cortex*, 74, 417–426, 2016.

[32] Amaral, L., Martins, M., Côrte-Real, M., Outeiro, T. F., Chaves, S. R., & Rego, A., "The neurotoxicity of pesticides: Implications for Parkinson's disease", *Chemosphere*, 377, 144348, 2025.

[33] Mnif, W., Hassine, A. I. H., Bouaziz, A., Bartegi, A., Thomas, O., & Roig, B., "Effect of endocrine disruptor pesticides: A review", *Int. J. Environ. Res. Public Health*, 8(6), 2265–2303, 2011.

[34] Thongprakaisang, S., Thiantanawat, A., Rangkadilok, N., Suriyo, T., & Satayavivad, J., "Glyphosate induces human breast cancer cells growth via estrogen receptors", *Food Chem. Toxicol.*, 59, 129–136, 2013.

[35] Miranda, R. A., Silva, B. S., de Moura, E. G., & Lisboa, P. C., "Pesticides as endocrine disruptors: programming for obesity and diabetes", *Endocrine*, 79(3), 437–447, 2023.

[36] Jain, D., Verma, R. K., Sharma, V., Kaur, A., Rai, A. R., Kumari, P., ... & Parihar, K., "Associations between high levels pesticide and adverse reproductive outcomes in females: A comprehensive review", *Mater. Today Proc.*, 95, 50–60, 2023.

[37] Fucic, A., Duca, R. C., Galea, K. S., Maric, T., Garcia, K., Bloom, M. S., ... & Vena, J. E., "Reproductive health risks associated with occupational and environmental exposure to pesticides", *Int. J. Environ. Res. Public Health*, 18(12), 6576, 2021.

[38] Lee, G. H., & Choi, K. C., "Adverse effects of pesticides on the functions of immune system", *Comp. Biochem. Physiol. C Toxicol. Pharmacol.*, 235, 108789, 2020.

[39] OECD/FAO, "OECD-FAO Agricultural Outlook 2023–2032", *OECD Publishing*, Paris, 2023. Doi: 10.1787/08801ab7-en

[40] Republic of Türkiye, Ministry of Agriculture and Forestry, Pesticide Use and Residue Control in Türkiye: 2023 Evaluation Report, General Directorate of Food and Control, 2023.

[41] Özercan, B., & Taşcı, R., "Türkiye'de pestisit kullanımının iller, bölgeler ve pestisit grupları açısından incelenmesi", Ziraat Mühendisliği, (375), 75-88, 2022.

[42] Yılmaz, H., Düzenli, A., & Dağ, M. M., "Dünya, Avrupa Birliği Ülkeleri ve Türkiye'de Pestisit Kullanımı ve Yasal Düzenlemeler", Türkiye Tarımsal Araştırmalar Dergisi, 11(3), 315-330, 2024.

[43] Tian, F., Zhou, Z., Lu, J., Qiao, C., Wang, C., Pang, T., Guo, L., Li, J., & Xie, H., "Development and validation of a combined QuEChERS and HPLC-MS/MS method for trace analysis of ten diamide insecticides in agricultural products. Analytical Methods", 17(3), 456–465, 2025 https://doi.org/10.1039/D4AY02117G

[44] Scorza, F. A., Beltramim, L., & Bombardi, L. M., "Pesticide exposure and human health: Toxic legacy", *Clinics*, 78, 100249, 2023.

[45] Tsakiris, P., Damalas, C. A., & Koutroubas, S. D., "Risk perception and use of personal protective equipment (PPE) in pesticide use: does risk shape farmers' safety behavior?", *Int. J. Environ. Health Res.*, vol. 35(2), 453–463, 2025.

[46] Lari, S., Yamagani, P., Pandiyan, A., Vanka, J., Naidu, M., Senthil Kumar, B., ... & Jonnalagadda, P. R., "The impact of the use of personal-protective-equipment on the minimization of effects of exposure to pesticides among farm-workers in India", *Front. Public Health*, 11, 1075448, 2023.

[47] Nicolopoulou-Stamati, P., Maipas, S., Kotampasi, C., Stamatis, P., & Hens, L., "Chemical pesticides and human health: the urgent need for a new concept in agriculture", *Front. Public Health*, 4, 148, 2016.

[48] Calliera, M., & L'Astorina, A., "The role of research, communication, and education for a sustainable use of pesticides", *Advances in Chemical Pollution, Environmental Management and Protection*, 2, 109-132 Elsevier, 2018. Doi: 10.1016/bs.apmp.2018.03.002

[49] Ahmadipour, H., & Nakhei, Z., "The effect of education on safe use of pesticides based on the health belief model", *BMC Res. Notes*, 17(1), 134, 2024.

[50] Gamage, A., Gangahagedara, R., Gamage, J., Jayasinghe, N., Kodikara, N., Suraweera, P., & Merah, O., "Role of organic farming for achieving sustainability in agriculture", *Farming Syst.*, 1(1), 100005, 2023.

[51] Jouzani, G. S., Valijanian, E., & Sharafi, R., "*Bacillus thuringiensis*: a successful insecticide with new environmental features and tidings", *Appl. Microbiol. Biotechnol.*, 101, 2691–2711, 2017.

[52] Wang, Z., Qiao, X., Wang, Y., Yu, H., & Mu, C., "IoT-based system of prevention and control for crop diseases and insect pests", *Front. Plant Sci.*, 15, 1323074, 2024.

[53] Arakawa, T., & Kamio, S., "Control efficacy of UAV-based ultra-low-volume application of pesticide in chestnut orchards", *Plants*, 12(14), 2597, 2023.

[54] Jintana, S., Sming, K., Krongtong, Y., & Thanyachai, S., "Cholinesterase activity, pesticide exposure and health impact in a population exposed to organophosphates", *Int. Arch. Occup. Environ. Health*, 82, 833–842, 2009.

[55] Aprea, C., Colosio, C., Mammone, T., Minoia, C., & Maroni, M., "Biological monitoring of pesticide exposure: a review of analytical methods", *J. Chromatogr. B*, 769(2), 191–219, 2002.

[56] London, L., & Bailie, R., "Challenges for improving surveillance for pesticide poisoning: policy implications for developing countries", *Int. J. Epidemiol.*, 30(3), 564–570, 2001.

[57] Snipes, S. A., Thompson, B., O'Connor, K., Shell-Duncan, B., King, D., Herrera, A. P., & Navarro, B., "Pesticides protect the fruit, but not the people: using community-based ethnography to understand farmworker pesticide-exposure risks", *Am. J. Public Health*, 99(S3), S616–S621, 2009.

[58] Bradman, A. S. A., Salvatore, A. L., Boeniger, M., Castorina, R., Snyder, J., Barr, D. B., ... & Eskenazi, B., "Community-based intervention to reduce pesticide exposure to farmworkers and potential take-home exposure to their families", *J. Expo. Sci. Environ. Epidemiol.*, 19(1), 79–89, 2009.

[59] Eddleston, M., Buckley, N. A., Eyer, P., & Dawson, A. H., "Management of acute organophosphorus pesticide poisoning", *Lancet*, 371(9612), 597–607, 2008.

[60] Akyıldız, H. Ç., & Okyay, P., "The Development and Scope of the Concept of Prevention in Health", *Journal of Continuing Medical Education (Sürekli Tıp Eğitimi Dergisi)*, 33(2), 146–156, 2024.